UNIVERSITÀ DEGLI STUDI DI TRIESTE

XXVIII CICLO DEL DOTTORATO DI RICERCA IN

NANOTECNOLOGIE

Capacitance ImmunoSensor for the early detection of circulating cancer biomarkers

Settore scientifico-disciplinare: FIS/03

DOTTORANDO

Pietro Capaldo

COORDINATORE

PROF. LUCIA PASQUATO

SUPERVISORE DI TESI

DR. Loredana Casalis

Capacitance Immunosensors for the early detection of Circulating Cancer Biomarkers

March 10, 2016

Contents

Abstract - English

The quantication of signicant amounts of disease biomarkers circulating in the bloodstream represents one ofthe challenging frontiers in biomedicine. The complexity of blood composition has opened the quest for novel detection technologies, capable of discerning small amount of specic biomarkers from other blood proteins/oligonucleotides and of reliably measuring them. In this context, we have developed a device based on dierential double-layer capacitance readout at microfabricated gold electrodes and demonstrated its detection performance in real bio-sample volumes.

In particular, in this PhD thesis, I will show my results in improving and implementing a biosensor based on a three-electrodes electrochemical readout using two miniaturized gold (working and counter) electrodes and a mm-sized AgCl pellet reference electrode, with the nal scope of detecting cancer biomarkers circulating in blood in real-time and in-situ. This biosensor has demonstrated to be able to detect DNA-hybridization with a detection limit of 1 pM, starting from a probing ssDNA-SAM (self-assembled monolayer) on the gold-coated working electrode. The measurements were rst carried out in pure saline buer solution, monitoring the dierential capacitance at the Working Electrode versus the incubation time. The kinetics studies, modeled using the Langmuir adsorption isotherm, not only give us important information on DNA hybridization kinetics but also allow to detect eventual mismatches along the target DNA sequence proving to be sensitive to the position of the mismatch with respect to the surface of the device. Furthermore, we are able to detect and quantify, in human extract and plasma, an unknown concentration of a specic microRNA (miRNA) biomarker connected to heart failure disease, using miRNA/complementary ssDNA calibration curves. The results were then conrmed using a real time qPCR by our MD partners at the University of Udine, D. Cesselli and A.P. Beltrami.

Beside miRNA, I have demonstrated that my device can detect more complex components such as protein biomarkers on single-domain antibodies (e.g. VHH fragments)

DNA conjugates in human serum. In particular, I have focused on the detection of the protein HER2, overespressed in many types of cancer. In addition, I have performed a systematic characterization of the device varying the physiological conditions (e.g. salt type: KCl, NaCl, $MgCl_2$, PBS, etc. and concentration), at different ssDNA SAM density conditions (estimated by using an XPS) and applying different potential in order to have a more comprehensive understanding of the phenomena occurring at the electrode/electrolyte interface. Such studies have led to the implementation of a theoretical model, to provide an explanation, consistent with the experimental data, of the biophysical phenomena that contribute to the biorecognition of the events of interest. Recently, I started exploring new routes to improve the sensitivity of our devices: on one hand, through Au nanoparticles amplication; on the other hand, through the development of a multiplexing system, which also requires the miniaturization of the reference electrode on the same plane of the other two gold electrodes, to increase device portability and its limit of detection.

In conclusion, by means of EIS measurements in a three electrodes setup, we built a device based on DNA hybridization detection, which was carefully calibrated for optimal biorecognition. With such device we were able to quantify the presence of microRNAs (miRNAs) in cellular extract and in human plasma. We demonstrated that our device is fast, sensitive, reusable, reproducible and perfectly suited to measure binding anities in complex matrices, as cell lysate, serum and blood plasma. We applied this platform to the bioanity detection of protein biomarkers with the possibility to detect circulating drugs in blood, for therapeutic drug monitoring applications.

Abstract - Italiano

La detection e misurazione di biomarcatori tumorali e non circolanti nel sangue umano rappresenta una delle nuove e più impegnative frontiere in campo biomedicTuttavia, la complessità delsangue umano ha reso necessario lo sviluppo dinuove tecnologie di rilevamento, in grado di discernere piccole quantità dibiomarcatori specici dagli altri oligonucleotidi o componenti proteiche presenti nel sangue e di misurarle in modo adabile. Ed è in questo contesto, che abbiamo sviluppato un biosensore in grado di misurare le variazioni della capacità dierenziale che avvengo all'interfaccia elettrodo/elettrolita (per questo nota come capacità di double-layer) e connessi ad eventi di bioriconoscimento dimostrando buone capacità di rilevamento anche in ambienti reali quali plasma umano ed estratto cellulare.

In particolare, in questa tesi di dottorato, vi mostrerò i risultati da me ottenuti nel miglioramento di un dispositivo costituito da un redout elettrochimico a due elettrodi d'oro microfabbricati (di lavoro e ausiliario) e un elettrodo di riferimento di AgCl di dimensioni millimetriche, con la scopo nale di rilevare biomarcatori tumorali circolanti nel sangue, in tempo reale e in-sitQuesto biosensore ha dimostrato di essere in grado di rilevare il processo di ibridazione del DNA con un limite di detection di 1 pM, a partire da un monostrato di DNA a singolo lamento (ssDNA-SAM) auto-assemblato sull'elettrodo di lavoro. Le misurazioni sono state eettuate in una soluzione tampone salina pura e la capacità dierenziale in corrispondenza dell'elettrodo di lavoro in funzione del tempo di incubazione è stata poi monitorata.

Gli studi cinetica, attraverso il modello di adsorbimento di Langmuir, non solo ci danno informazioni importanti sulla cinetica di ibridazione DNA ma anche permettere di rilevare eventuali spaiamenti di basi lungo la sequenza del DNA d'interesse dimostrando, inoltre, di essere sensibile alla posizione del disallineamento rispetto alla supercie il dispositivo. Inne, siamo in grado di rilevare e quanticare, sia in estratto cellulare che in plasma umano, una concentrazione sconosciuta di uno specico frammento di RNA (mi-

croRNA, o miRNA) biomarcatore specico dell'insucienza cardiaca, utilizzando curve di calibrazione di ssDNA/miRNA complementare. I risultati sono stati poi confermati attraverso l'uso di una qPCR in tempo reale grazie ai nostri partner presso l'Università di Udine, i MD D. Cesselli e A.P. Beltrami e collaboratori.

Oltre lo studio e rilevazione dei miRNA, ho dimostrato che il dispositivo è in grado di rilevare componenti più complessi quali biomarcatori proteici su anticorpi a singolo dominio (ad esempio frammenti VHH) coniugati a lamenti di DNA in siero umano. In particolare, ci siamo concentrati sulla rilevazione della proteina HER2, la cui sovraespressione è stata rilevata in molti tipi di cancro ma in special modo in forme particolarmente aggressive di cancro al seno. Inoltre, ho eseguito una caratterizzazione sistematica del dispositivo variando le condizioni siologiche (ad esempio il tipo di sale: KCl, NaCl, MgCl2, PBS, etc. e lo loro concentrazione), a diverse condizioni di densità del ssDNA-SAM (stimata utilizzando un XPS) e applicando diversi potenziali in modo da avere una comprensione più completa dei fenomeni che avvengono all'interfaccia elettrodo/elettrolita. Tali studi hanno portato alla realizzazione di un modello teorico, in grado di fornire una spiegazione, coerente con i dati sperimentali, dei fenomeni biosici che contribuiscono al bioriconoscimento degli eventi di interesse.

Recentemente, ho iniziato a esplorare nuove vie per migliorare la sensibilità dei nostri dispositivi: da un lato, attraverso l'uso di nanoparticelle d'oro in grado di amplicare il segnale delle variazioni d'interesse; dall'altro, attraverso lo sviluppo di un sistema di misurazioni a multicanale, che richiede anche la miniaturizzazione dell'elettrodo di riferimento sullo stesso piano degli altri due elettrodi in oro, al ne di aumentare la portabilità del dispositivo e inoltre il suo limite di rilevazione.

In conclusione, mediante tecniche di spettroscopia ad impedenza elettrochimica (EIS) in una congurazione a tre elettrodi di cui due microfabbricati, abbiamo realizzato un dispositivo basato sulla rilevazione dell'ibridazione, in-situ, di oligonucleotidi (DNA/RNA) che è stato poi accuratamente calibrato per un ottimale bioriconoscimento. Grazie a questo dispositivo, siamo stati in grado di quanticare la presenza di microRNA (miRNA) in estratto cellulare e in plasma umano. Abbiamo dimostrato che il nostro dispositivo è veloce, sensibile, riutilizzabile, riproducibile e perfettamente adatto per misurare anità di legame in matrici complesse, come lisato cellulare, siero e plasma sanguigno.

Chapter 1

Introduction

In the last decades the growing interest towards personalized therapies has motivated the development of an increasing number of miniaturized, label-free devices to be used as fast diagnostic tools for medical treatment ([1, 2, 3, 4, 5]). Moreover, in recent years the measurements of blood (and its components) impedance through an alternating current has been suggested as a non-invasive approach to determine some blood disorders [6]. The nal goal, of all these devices, is the detection of biological biomarkers (as proteins, microRNA (miRNA), small pieces of DNA, etc.) circulating in the bloodstream, and to selectively distinguish them from the huge amount of other, non-disease-representative molecules.

Label-free biosensors require only a single recognition element, leading to simplied assay design, decreased assay time and reduction in reagent costs. Another advantage of label-free method is the ability to perform quantitative measurement of molecular interaction in real-time, allowing continuous data recording. Moreover, target analytes are detected in their natural form without labeling and chemical modication. The label-free sensing strategies operate through a binding-event-generated perturbation in optical, electrical or mechanical signals.

Optical transducers are widely used due to their high sensitivity with several well established optical phenomena such as surface plasmon changes [7, 8, 9, 10], light scattering/adsorption [11, 12, 13, 14]. Most label-free optical biosensors require precise alignment of light coupling to the sensing area, which is a major drawback for point-of-care applications. Therefore, optical sensing can be signicantly improved integrating this approach to several passive and active optical components on the same substrate, allowing the fabrication of multiple sensors on one chip.

Advances in micro- and nanofabrication technologies have facilitated the emergence of micro- and nanoscale mechanical transducers capable of detecting changes in force, motion, mechanical properties and mass that come along with molecular recognition events [15, 16, 17, 18]. Among the different mechanical biosensors, cantilever and quartz crystal microbalances (QCMs) are the most established techniques. Mechanical bending of a micro- or nanocantilever is monitored as analytes bind, with optical readout typically used to detect the deflection or change in stress/strain profile of the cantilever. In one example, Kosaka et al., 2014, [19] developed a sandwich assay that combines mechanical and optoplasmonic transduction which can detect cancer biomarkers in serum at ultra low concentrations. In this array the second antibody is tethered to a gold nanoparticle that acts as a mass and plasmonic label; the two signatures are detected by means of a silicon cantilever that serves as a mechanical resonator for `weighing' the mass of the captured nanoparticles and as an optical cavity that boosts the plasmonic signal from the nanoparticles, achieving a detection limit of 1×10^{-16} g ml^{-1} in serum which is at least seven orders of magnitude lower than that achieved in routine clinical practice. This class of biodetectors is very appealing in terms of limit of sensitivity and it is well suited to laboratory applications; however, the application of an external potential to a piezoelectric material (in this case the quartz crystal) produces internal mechanical stresses that induce an oscillating electric field. Moreover, the resonance frequency shift can be influenced by many factors, such as changes in mass, viscosity, dielectric constant of the solution and the ionic status of the crystal interface with the buffer solution.

The best performances are expected by detectors based on electrical readout, both in terms of cost reduction and of multiplexing analysis of different biomarkers. These sensors integrated with microfluidic networks in a Lab-on-a-Chip platform, can develop into easy-to-use, rapid and reliable diagnostic kits to be operated as medical practitioner's bench tool [20]. In contrast to the others that are interesting in terms of limit of sensitivity and well suited to laboratory applications but whose cost cannot easily be decreased to make them not available for systematic point-of-care diagnostics.

Electrical readout assays monitor the response of the system to the application of a small amplitude (hundreds of mV) AC voltage to functionalized gold electrodes, and can measure, as a function of the AC frequency, the capacitance variation at the electrode/electrolyte interface upon the occurrence of biorecognition events. These types of measurements are known as electrochemical impedance spectroscopy (EIS) measurements. The application of an AC-voltage instead of a DC-voltage is a fundamental trick

to avoid charge-transport from the electrode to the electrolyte and vice-versa which are inducing a rise of electrochemical reactions that can change the ionization state of the atoms at the surface. In this way, at the interface, the moving ions in solution are periodically attracted and repelled from the surface oscillating around a central position and, in first approximation, they behave like a planar capacitor. This capacitance is called double layer capacitance, C_{DL}, and it is formed by the charged electrode (because of the applied potential) and the layer of mobile ions in the diffusive layer within a distance equal to the Debye length[1] of the solution.

In 1853 Helmholtz, knowing that at the equilibrium, the charge in the metallic electrode is distributed at its surface, modeled the electrode/electrolyte interface as composed of two layers of opposite polarity where the ions in solution counterbalance exactly the charge on the metal and form, together with the electrode, the double layer capacitance, C_{DL}. After this first model several scientists refined the theory but the name given by Helmoltz to the double layer capacitance remained.

For a mathematical treatment of the interface one can introduce an equivalent circuit described in Figure 1.1, where the two[2] main components of the equivalent circuit: C_{DL} and $R_{channel}$ are highlighted ([21, 22]). As already explained, C_{DL} models the solid/liquid interface whereas $R_{channel}$ idealizes the ionic resistance of the electrolyte solution in the pool.

In literature can be found many examples of bio-detectors based on Electrochemical Impedance Spectroscopy [12, 22, 23, 24]. In general, according to the frequency of

[1] In electrochemistry the Debye length is the measure of a charge carrier's net electrostatic effect in solution, and how far those electrostatic effects persist. For a symmetric monovalent salt, is defined as:

$$k^{-1} = \sqrt{\frac{\varepsilon_r \varepsilon_0 RT}{2F^2 C_0}} \tag{1.1}$$

where R is the gas constant, T the absolute temperature, F the Faraday constant, C_0 the molar concentration of the electrolyte, ε_r and ε_0 are the dielectric constant of the solution and vacuum, respectively. k^{-1} gives us information about the electrostatic screening effect of the solution and, as we can see in Equation 1.1, decreases for increasing ionic strength.

The ionic strength provides the concentration of all ions present in a solution,

$$I = \frac{1}{2} \sum_{i=1}^{n} c_i z_i^2 \tag{1.2}$$

where c_i is the molar concentration of ion i (M, mol/L), z_i is the charge number of that ion, and the sum is taken over all ions in the solution.

[2] considering negligible and therefore not reported the parasitic contribution of the surrounding environement (cables, wires, etc.).

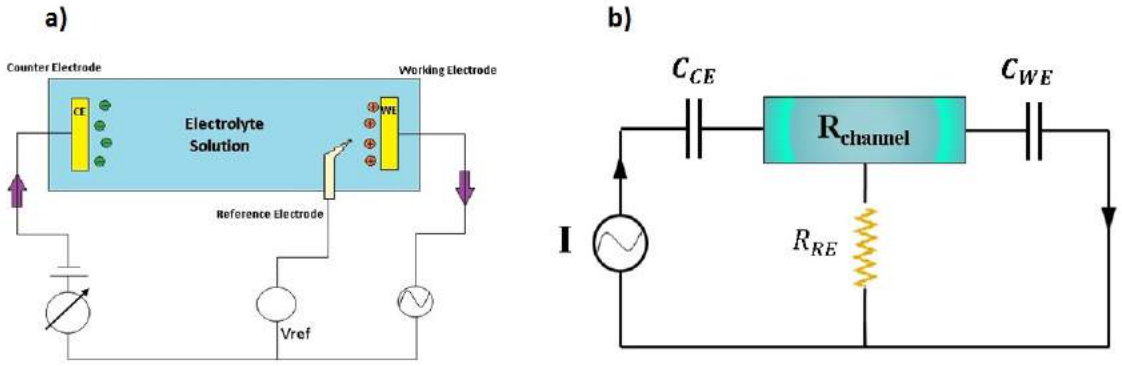

Figure 1.1: a) Idealization of the physical system of the measuring setup. b) Equivalent electrical circuit of our biosensor. C_{DL} models the interface electrode/electrolyte while $R_{channel}$ represents the ionic resistance of the channel.

the applied voltage, the capacitance at the electrode/electrolyte interface or the resistance of the electrolytic solution is measured [1, 22]. The devices based on resistivity measurements showed high sensitivities [23, 24] whenever an appropriate choice of the functionalization of the substrate. In resistance immunosensors a redox species is alternately oxidized and reduced by the transfer of an electron to and from the metal electrode. Thus, faradaic EIS requires the addition of a redox-active species and DC bias conditions such that it is not depleted [24-1].

Capacitive readout oers the ability to create label-free integrated microsystems with miniaturized dimensions thus saving cost, time and system complexity. The possibility to integrate capacitive biosensor arrays into a single chip along with the enablement of electrical detection are perhaps the most signicant advantages of this kind of sensors. Integration, on one hand, significantly increases throughput and automation of the device and reduces the size of the biosensor as well as the cost of the diagnostic assays avoiding to consume hundreds of microliters of expensive reagents, while electrical detection eases readout electronics design and implementation thus leading to compact portable instruments for point-of-care diagnostics with great results in terms of device sensitivity, e.g. 0.1 pM is the detection limit achieved by Limbut and co-workers[25] in the Bacterial Endotoxin detection using gold electrodes. Qureshi et al.[26], showed a limit of detection of 25 pg/ml for the detection of biomarkers connected to cardiovascular risk by using an assay of interdigitated gold electrodes.

On the other hand, in the capacitive biosensor world, very few works have been presented indicating reliable detection of an analyte in real complex samples. Although

the biological receptors are usually specic, interfering substances in the analyte solution may aect both the sensor selectivity and sensitivity[27, 28]False positive or false negative results may be due to the matrix components. A common practice for compensating the eect of interfering parameters is dierential measurements using reference sensors without biological receptors on their surface or with molecules that are expected not to interact with the analyte.

This type of devices may have a great impact in the future of medical diagnostics but, at the same time, the fabrication steps and the functionalization with biomolecules are still very complex.

For all these reasons we decided to concentrate our attention on detectors based on capacitance read-out[29]working thus at low frequencies (which,given the dimensions of our setup and buer conditions, means frequencies lower than 1.3 kHz) where the so called double layer capacitance dominates,as demonstrated by Zou et al.[30]. In this regime, it is crucial to control the voltage applied to the electrodes with high accuracy, to avoid voltage-induce damaging of the functional molecules adsorbed on the gold surface. To this aim, a third reference electrode is often used.In fact, it was demonstrated in a previous work of our group that a three-electrode, miniaturized capacitive device allows for high time stability, enables rapid, real-time response and improves resolution[29], hence being an ideal candidate for fast personalized diagnostics, and/or therapeutic drug monitoring ([31, 32]).

In particular, we concentrated on DNA detection. Oligonucleotides are in fact interesting for biomedical and technical reasons:

- DNA is the most stable biological molecule that contains information about the source organism.This makes it the ideal molecule for pathogen detection and drug discovery. Moreover, the ability to synthesize DNA oligonucleotides allows for the low-cost design of DNA biosensor microarrays;

- The unique biomolecular recognition properties of DNA, based on Watson and Crick base pairing, can be exploited to detect complementary DNA (or RNA) strands in solution and to bind antibody DNA-conjugates with a high bioanity level;

- In DNA sensors,the target gene sequence is identied by a DNA probe that can form a double-stranded (dsDNA) hybrid with its complementary nucleic acid with high eciency and extremely high specicity in the presence of a mixture of many

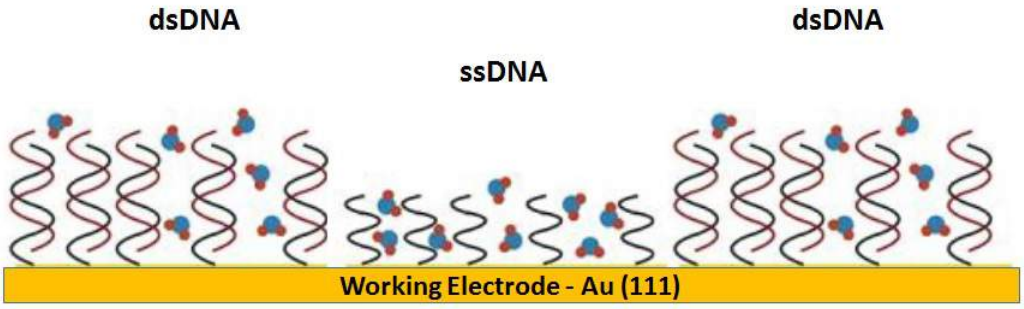

Figure 1.2: Cross section of the mixed Self assemble Monolayer (SAM) formed by ssDNA- and dsDNA-molecules immobilized on Au(111) gold lm. Because ofthe variation in the persistence length of the DNA-molecules after hybridization (from 1 to 50 nm), the ssDNA is more exible than dsDNA which results in a shorter rod.

dierent, non-(or not fully-)complementary nucleic acids. A single mismatch for a 20 bases long probe can destabilize the complex such that its melting temperature is reduced by 5°C [33]This makes detection using DNA strands extremely specic, given that the probe length is short enough for the mismatch to be signicant, but long enough for the global stability of the molecular complex;

- DNA molecules remain intact up to about 80° C. As temperature is lowered,the denatured DNA will self-recognize and hybridize once again, so the device can be reusable;

- Label-free DNA sensors have been built on many dierent substrates and materials, including gold and carbon, silicon dioxide, diamond, quartz, optical ber and conducting polymers[34].

One of the challenges in building surface-based DNA sensors is the link of the probes to the transducer substrate. This is particularly important for sensors that rely on electron transfer reactions that involve the DNA molecule. Single stranded DNA probes can be immobilized on a surface via long-range electrostatic forces, or by chemical attachment to a surface. For a durable, highly sensitive biosensor a particular care must be given to probe immobilization on the surface. Achieving control over the construction and operation of microfabricated label-free DNA biosensors would be a big leap in the quest for highly reliable clinical laboratory tests. A rst step towards this goal is the

characterization of the device, which means the research of the best operating conditions to perform the various experiments.

It becomes clear that, whether it is for genomic protein application for early screening of diseases, routine walk-in medical checkups, or forensic analysis, controlled design of these sensors is essential. Reliable outcomes of critical medical tests mean less need for repetitions, offering better diagnosis with earlier intervention and more efficient therapies. The problem of achieving a repeatable outcome is still open. Even in the case of the electrochemical based DNA sensors, the output is fitted with an empirical or semi-empirical model, and some conclusions are derived. It is, however, very important to know what mechanisms cause the biosensor to operate. Simulation of the sensors using physical models can shed light into these mechanisms and help answer this question [35].

The aim of the present Ph.D. work is to design, develop and characterize a DNA-biosensor with electrical read-out proving its clinical utility through the detection of circulating cancer biomarkers as microRNAs, in real, complex environment (e.g. blood, serum).

To achieve the aims described above, a miniaturized electrochemical cell was designed and developed (cf. Figure 1.3). So, starting from this measuring setup, our final purpose is to implement and microfabricate a biosensing platform based on electrochemical impedance readout with the ultimate goal of performing label-free, real-time measurements of clinically relevant biomarkers. The idea is very simple and consists in functionalizing the gold surface of the WE with surface-immobilized ssDNA-molecules with different sequences and perform EIS measurements of oligonucleotides hybridization (DNA, miRNA), in order to exploit the expertise of the group in the functionalization of gold surfaces, or measuring the electrical response of the device due to an antigen-antibody biorecognition event, conjugating the protein to an oligonucleotide strand via DNA directed immobilization (DDI) [36, 37].

First, a systematic analysis of a single stranded DNA film deposited on a gold electrode was performed. In particular, different geometrical, physiological and read-out parameters (e.g. ssDNA probe surface density, ionic strength, potential applied to the electrodes) were exploited to calibrate the device and optimize its performance in order to define the best operating conditions for the detection of complementary DNA and/or RNA hybridization processes occurring at the electrode/electrolyte interface. We modeled our sensor by means of mean-field simulation in 3D using finite element analysis.

Then, the optimized device was used to detect the unknown concentration of miRNAs in cell extract and in human plasma of patients with heart failure disease, using derived calibration curves to quantify it. We distinguished two contributions to the variation of dierential capacitance: one, due to the blocking eect of the complex matrix (e.g. human plasma) and a second one, showing a time dependent kinetics, due to the specic miRNA/DNA biorecognition.

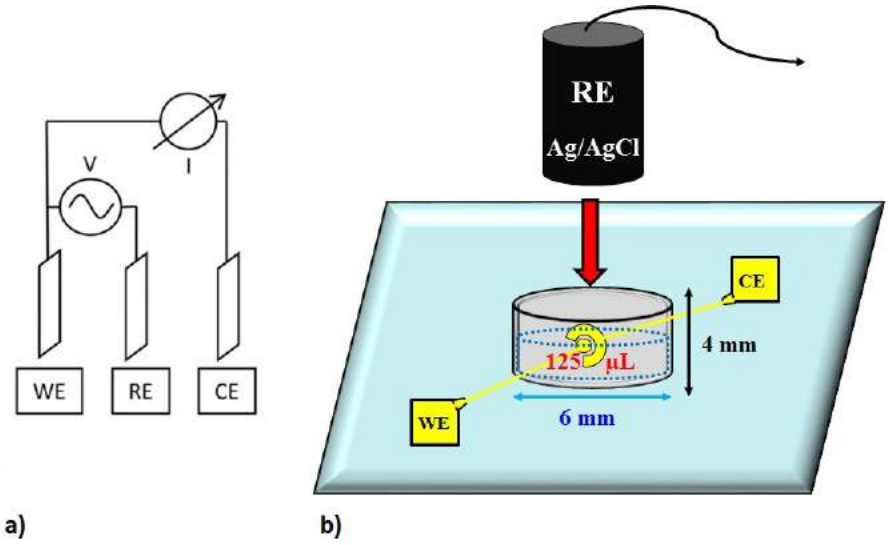

Figure 1.3: a) Scheme of the connections of the three-electrode setup. The potential is applied across WE and RE whereas the current is measured across WE and CE. b) Cartoon showing the assembling method of the three-electrode setup. In the foreground, the small silicone pool where the experiments were carried out. The dimensions are not to scale.

We are condent that our device constitutes a novel, sensitive, fast and cheap bio-analytical methods to detect disease biomarkers and/or genetic mutations and possibly usable in therapeutical drug monitoring.

Chapter 2

Materials and Methods

2.1 Device Fabrication & Measuring Setup

As already explained in the work of Ianeselli et al.[29], it is possible demonstrate that a device composed of three electrodes guarantees a more stable signal than one with only two electrodes[29,38]. Therefore an electrochemical cell composed of three electrodes was realized: the Working (WE) and the Counter (CE) electrodes are in the micrometer scale while the Reference (RE) is an electrode commonly used in electrochemical cells: millimeter size (d ' 4 mm) Ag/AgCl electrode obtained from the chlorination of a silver pellet. This kind of electrodes, called second-species reference electrodes, were chosen for their simplicity of manipulating and for their proper working in contact with a solution containing chloride anions (Nernst equation for these half-reactions depends only with the chloride concentration).

Devices were fabricated using proximity UV-optical lithography based process. Working and counter electrodes were produced on clean microscope slides by a classical lift-off process.

First of all, the clean[1] slides were dehydrated at 200 °C for 5 min and then treated with O_2-plasma in order to increase the adhesion of the photoresist. The parameters that we used to increase the hydrophilicity of microscope slides are listed in Table 2.1.

[1] The cleaning protocol consists in three successive baths in acetone, 2-Propanol and soapy milli-RO water in a sonicator water bath for 45 minutes in total, and thus rinsed with milliQ water.

Element	Power (W)	Flux(sccm)	P (mbar)	Bias (V)	Exp. time (min)
Oxygen O_2	60	30	1.5×10^{-1}	' 300	5

Table 2.1: Parameters for the oxygen plasma that we set in order to increase the adhesion of resist on glass substrateThe plasma treatment was performed in the chamber of the machine for reactive ion etching (RIE).

Successively the slides are rapidly cooled down in a nitrogen stream and immediately spin-coated with a UV-photo-sensible resist. In this thesis work we employed mostly MEGAPOSIT™ SPR™ 220 1.2 (Series Photo-Resist) as a positive resist. The type of the resist, negative or positive (as here),denes how the mask image is transferred. For negative resist the exposed areas remain on the slides after development whereas for positive resist the exposed areas are removed during development becoming soluble to the developer solution. According to the fabrication needs,one can vary the lm thickness by varying the rotational speed of the spin-coater, in our case, the resist was deposited on the glass slide to a thickness of 1.4μm. After spinning, the slides were put on a hot plate in order to perform the soft-bake (or Pre-Bake) of the resist. Temperature and baking time are dened by the resist and its thickness. At this point the samples were exposed to UV-light through a Chromium mask and the mask pattern was transferred into the photo-sensible lm. After the exposure the samples were immediately developed in a solution related to the specic resist. Again, after the developing step, the samples were subjected to a further thermal treatment called hard-bake in order to increase the thermal, chemical and physical stability of developed structures for subsequent processes. In the following Table 2.2, we listed all the details regarding the resists and procedures that we employed.

Resist	SPR™ 220 1.2	SU8-2002
Dehyd. glass slides	200°C for 5 min	100° for 5 min
Spinning	500 rpm for 5s 2500 rpm for 25 s	3000 rpm for 35 s
Soft-Bake	95°C for 1 min	65°C for 1 min
	thermal ramp 95°C→ 115°C	thermal ramp 65°C→ 95°C
	115°C for 90 s	95°C for 2 min
Exposure	13 sec @ 3 mW/cm^2	9 sec @ 5 mW/cm^2
Post-Bake	No	65°C for 1 min
		thermal ramp 65°C→ 95°C
		95°C for 1 min
Development	~ 28 sec in MF24A	~ 40 sec in SU8-Dev.
Rinse	in milli RO water	in IsoPropanol
Hard-Bake	115°C for 2 min	No

Table 2.2: Lithographic steps to be performed for the positive photoresist SPR™ 220 1.2.

After the described photolitographic steps, the so patterned slides were metalized using an e-beam evaporator.First the micro-patterned microscope slides were inserted in the evaporator and two metal layers, 20 nm of Titanium (in order to facilitate the adhesion on glass,) followed by an 80-nm Au layer,were deposited under high-vacuum (' 3×10^{-6} torr) in order to prevent oxidation and obtain smooth and uniform layers. Following evaporation, the slides underwent lift-o where the inverse patter layer is sacriced. In this process the samples were immersed in an acetone bath overnight and rinsed thoroughly with acetone to remove the last remnants of sacricial covered resist and eventually cleaned with isopropanol to remove any halo left by acetone bath. After lift-o process the samples with the two metalized electrodes required another complete lithographic sequence in order to dene the area of the working and counter electrode in contact with the solution and isolate the rest.In this last part of fabrication protocol, electrodes were coated with an insulating layer (about 3 µm) of NANO™ SU8-2002 (negative resist),shaped to expose only the circular part of the WE and the CE performing an aligned lithography using the mask aligner MJB3 by Karl Suss, Germany.

Pictures of the slides patterned with the micro-electrodes,are shown in Figure 2.1. The microfabricated electrodes are composed by two gold pads for wire-connection. The WE has a diameter of D_{WE} = 100 µm ($\Rightarrow A_{WE}$ ' 7.85×10^{-5} cm^2), and is connected to the gold pad by a path with variable width. The CE is an arc with a smaller diameter

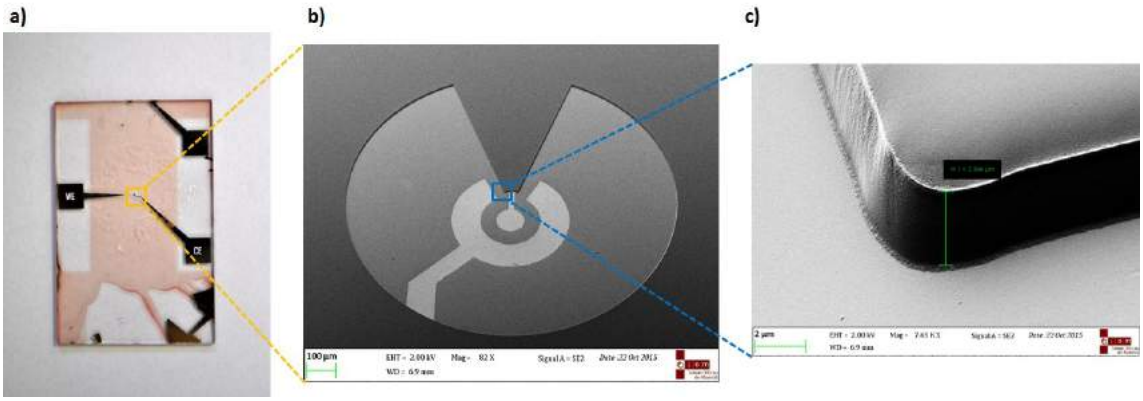

Figure 2.1: a) Picture of the microfabricated WE and CE for the three-electrode setup. b) SEM image of the microfabricated working (WE) and counter (CE) gold electrodes. The gold electrodes appear lighter than the background of the picture. c) The patterned insulation layer is shown and it is higher with respect to the plane of the electrodes. EHT=2 kV and Mag 82x.

of 300 µm that encloses the WE. A layer of SU8 2002 with a thickness of 2.9µm (recognizable in Figure 2.1) was realized in order to reduce the active area of the electrodes (pac-man shaped in Figure 2.1b)) and insulate the electrical path that connect WE and RE with the connection-pads.

In order to connect the electrodes with the electrical instruments, a sample holder suitable to the features of our patterned slides has been developed. The sample holder is shown in Figure 2.2a). From the picture, the micro-electrodes have been constrained between two Plexiglas slides. The measurements were carried out in a small silicone pool with a diameter of 6 mm and a height of 4 mm, holding a 125 µL volume. In this way the reference Ag/AgCl pellet electrode (diameter d = 5 mm), could be inserted directly in the solution through the hole in the top Plexiglas slide and placed just above the microelectrodes (see Figure 2.2). The electrical signal was collected from the gold pads (4×4 mm^2) by a circuit board with a specic design equipped with SMA connectors and spring-loaded pins (see Figure 2.2). In order to shield the device from parasitic contribution of the surrounding environment, we further designed and realized a very robust Faraday cage (see Figure 2.3a) and b)). The cage was made of solid 1 cm thick aluminum plates and with a total weight of about 10 kg. In this way also mechanical vibrations could be eectively shielded and measurements at low frequencies became easier.

The whole setup was then connected to a bipotentiostat model PG340 usb by Heka

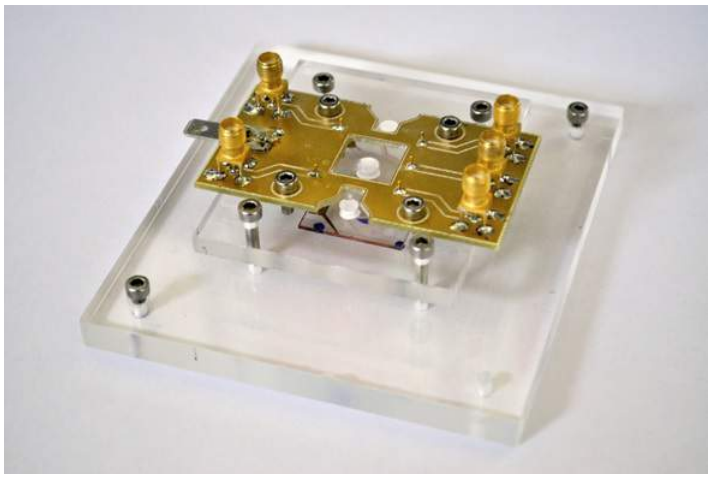

Figure 2.2: a) Sample holder for our miniaturized biosensor. The microscope slide with the micro-electrodes are constrained between two Plexiglas slides. The measurements were carried out in a small pool with a diameter of 6 mm and a height of 4 mm, holding a 125 µL volume. The reference Ag/AgCl pellet electrode is immersed directly in the solution through the hole in the top plexiglas slide and placed just above the microelectrodes. The electrical signal is collected from the gold pads (4x4 mm^2) by a circuit board of custom design with SMA connectors and spring-loaded pins.

(programmable via Potmaster Software) shown in Figure 2.3c). The advantage of the bipotentiostat, was the possibility to handle three electrodes. The third electrode in fact, which acts as Reference Electrode (RE), made of Ag/AgCl is used for the high stability of its potential in contact with the electrolytic components of human blood, to assure a ne control of the absolute value of the potential applied across WE and RE and thus the measurements of the current owing between WE and CE.

The potential applied during the measurements was an AC sinusoidal voltage center at 0 V, whose amplitude was optimized to the needs of the specic experiment and usually ranged from 10 mV to 150 mV. The stimulus signal for each time was mediated on four frequencies: 100 Hz, 200 Hz, 250 Hz and 400 Hz. These frequencies were chosen because in this regime the system has a purely capacitive response, (see Figure 2.3d)). At each frequency we collected 200 complete periods from which we computed the root mean squared value of the measured current, $I_{rms} = 2\pi f \cdot V_{rms} \cdot C_d$, and the relative uncertainties using error propagation analysis.

The procedure was implemented in Igor, a software for data analysis developed by Wavemetrics. The procedure was inserted in a loop in order to analyze the variations of C_d as a function of the time. Each time t is associated to a time-sampling of 2 seconds

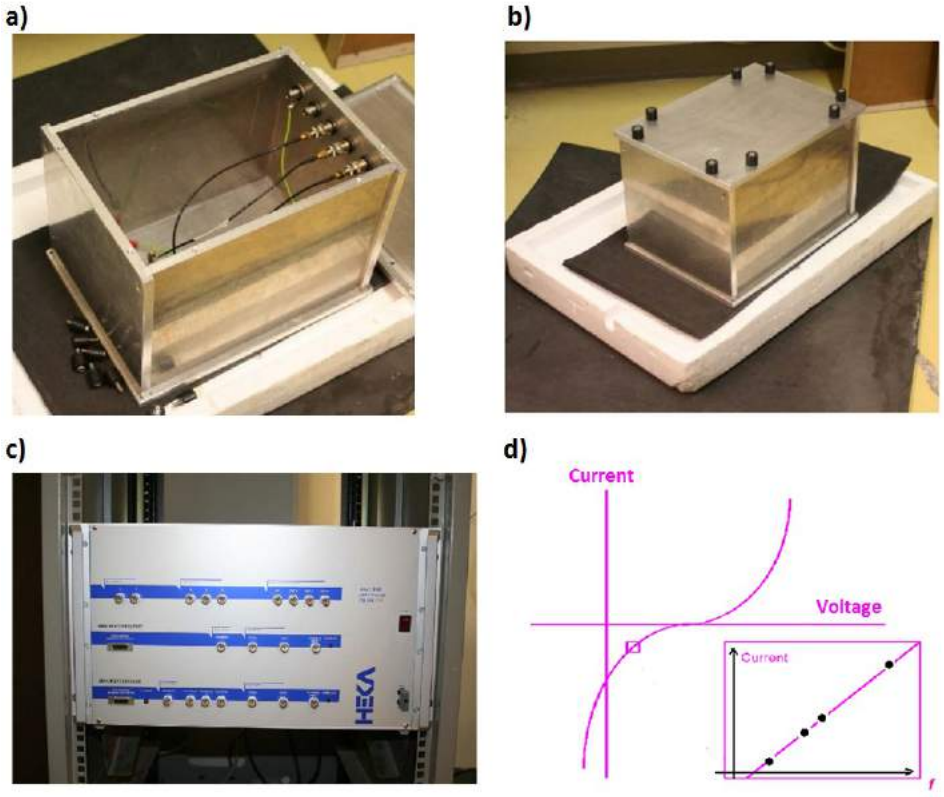

Figure 2.3: a) and b) Faraday cage designed in order to shield the external electromagnetic noise (the experiments were carried out at low frequencies, $\leq$ 1.3 kHz) and to prevent mechanical vibrations,made of Aluminum plates with a thickness of 1 cm and a total weight of roughly 10 kg. The cage permits the use of 5 BNC connection cables. c) Frontal point of view of the bipotentiostat, model PG340 usb by Heka.d) For small excitation signal, cell's response (C-V curve) can be approximate to be linear. In the inset, in frequency range 100-400 Hz the system has a pure capacitive response (image d) courtesy of Serena Rosa Alfarano).

(500 ms per each of the four frequencies).

In conclusion, by calculating the dierential capacitance C_d from the current I_{rms}, it can be possible to derive information about the DNA-SAM composition and assembling.

As already explained in the work of Ianeselli et al.[29],in fact, our device measures the dierential capacitance C_d at the electrode/electrolyte interface that, in our conguration, can be set equal to C_{DL}, the double layer capacitance already introduced in the previous section, and dened as:

$$C_{DL} \; ' \; C_{\;d} = \frac{\vartheta \sigma_M}{\vartheta \phi} \tag{2.1}$$

C_d reects the charge density (σ_M) change at the metal surface for a small variation of the applied potential (ϕ) between electrode and solution. In the case of a biofunctionalized metal electrode immersed in a saline solution, C_d can be modeled as a series connection of two capacitances ([39, 40]):the capacitance due to the absorbed layer of molecules (C_{mol} in Figure 2.4a)) and the one related to the ions in solution, the so-called diusive layer capacitance (C_{ions} in Figure 2.4a)).

According to this model, proposed by Helmholtz in 1853, the molecules in solutions can either lay down on the surface or stay in the diusive layer according to Boltzmann's distribution at a distance from the surface equal to the Debye length of the solution.

Normally, C_{ions} has densities of the order of 40 $\mu F/cm^2$, larger than C_{mol} ($\approx$ 10 $\mu F/cm^2$, in agreement with literature [41]). The nal capacitance is the inverse of the sum of the inverse of the two linked capacitors and thus the dominant contribution is due to the variations of C_{mol} that raised upon molecular adsorption on the electrode surface including height changes, changes in the electrical charge density and substitution of water molecules in the biological layer since the SAM layer is composed of DNA monolayer and of the ions solvating the strands (Figure 2.4b)).

The resulting capacitor can be treated as a planar capacitor and thus:

$$C_d = \; _{0\;r} \; \frac{A}{d} \; = \; _{0\;r} \; \frac{A_{WE}}{d} \tag{2.2}$$

where $_r$ is the dielectric constant of the molecular layer and $_0$ the vacuum permittivity, A is the surface occupied by the layer (here is equal to the area of the gold working electrode, A_{WE} ' 7.85×10^{-5} cm^2) and d is the thickness of the monolayer. From Equation 2.2 we recognize immediately the weakness of the model proposed by Helmholtz,

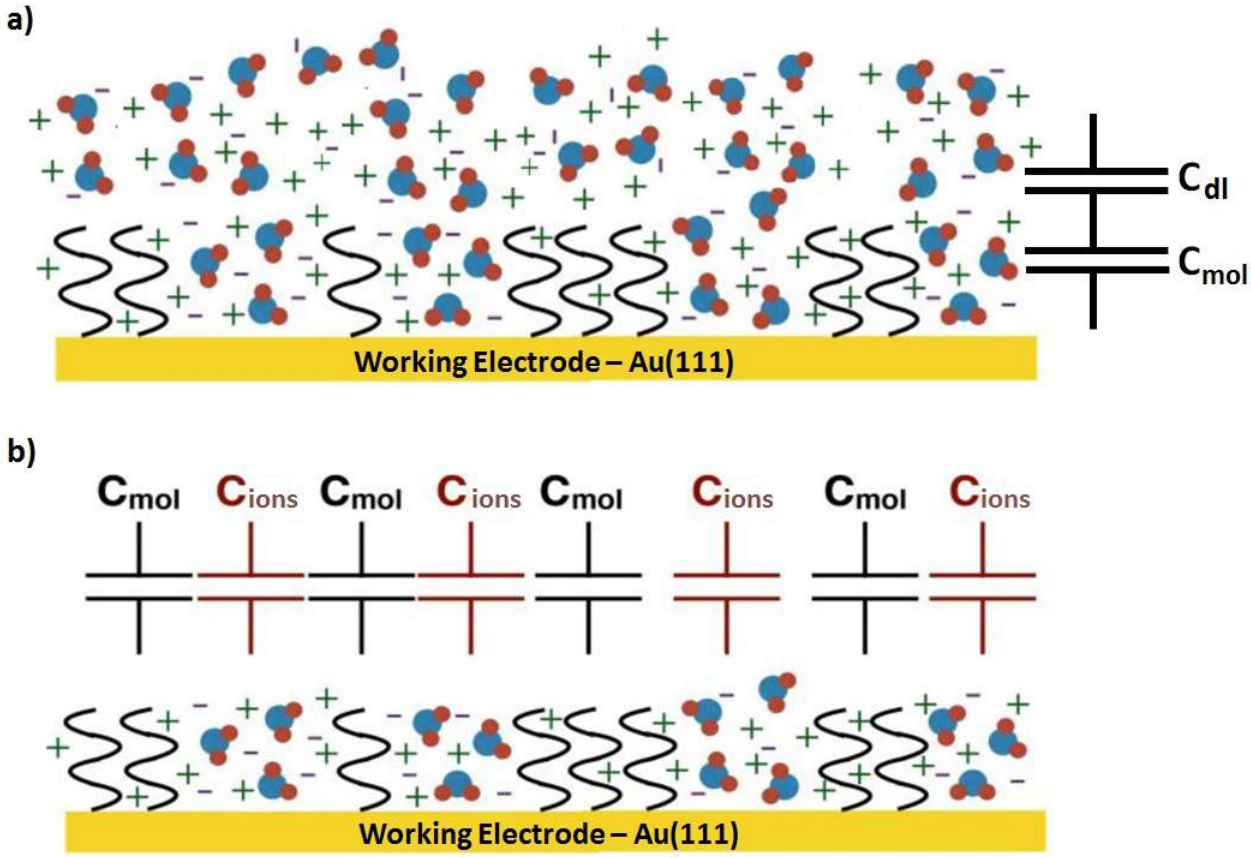

Figure 2.4: Idealization of the electrode/electrolyte interface. a) The rst layer consists of ssDNA on Au(111) surface. The counterions in solution, just above the molecular layer, composes the second layer modeled with a second capacitance, C_{ions}, in series with the rst one. b) The total capacitance at the interface is the sum of capacitances linked in parallel and associated to the area composed of DNA strands or ions.

although it represents a good approximation of our device, , C_d is independent of the applied voltage, and this is the main reason that prompted me to look for a model that took account the applied potential and also shows the dependence of and d from the target concentration in solution.

2.2 Oligonucleotides

DNA and RNA are nucleic acids whose purpose is the transport of genetic information and consist of monomers called nucleotides. Therefore, oligonucleotides (from the

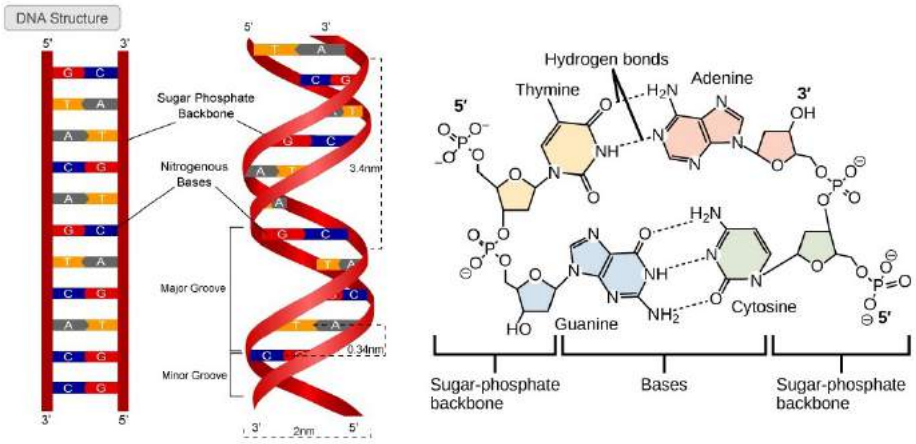

Figure 2.5: The structure of the DNA double helix. The red-colored backbone is composed of sugar-phosphate bonds and the bases in the structure are color-coded by element and the detailed structure of two base pairs are shown in the right. Image courtesy of Serena Rosa Alfarano.

Greek "oligo" which means few or small) are short DNA or RNA molecules characterized by a sequence of nucleotide residues that make up the entire molecule and constitute the keystone of the research described in this thesis work.

A nucleotide is made of a nucleobase (also termed a nitrogenous base), a ve-carbon sugar (either ribose or 2-deoxyribose depending on if it is DNA or RNA) and one phosphate groups.

Nitrogenous bases are typically classied as the derivatives of two parent compounds, pyrimidine (include uracil, thymine, cytosine) and purine (adenine and guanine), abbreviated as U, T, C, A, and G, respectively. Uracil and thymine are identical except that uracil lacks the 5' methyl group.

Most of DNA exists as double stranded DNA, consisting of two oriented, complementary, polynucleotide sequences. Double helix is 2.2 ÷ 2.6nm large and one base-pair corresponds to approximately 0.34 nm of length along the strand.

From Figure 2.5 one can see that lateral DNA structure (backbone) is composed by repeated phosphate groups between two sugars with ve carbon atoms (deoxyribose for DNA and ribose for RNA): each phosphate group is bound to the 3^0 carbon of the rst sugar and the 5^0 carbon of the following sugar. In this way DNA is oriented in the direction of phosphate bonds. Double helix is created by bonds between nitrogenous bases and purines pair with pyrimidines mainly for dimensional reasons,in fact, only

this combination ts the constant width geometry of the DNA spiral. The G ≡ C pair is bound by three hydrogen bonds,while A = T bound by two hydrogen bonds,which means that DNA sequence with a high GC-content has a greater thermal stability than DNA with a lower percentage of GC bonds.

The rst interesting (for ours studies) property of DNA that deserves to be emphasized is its ability to create a self-assembled monolayer on (and not only) gold surfaces. Among the many SAM system investigated, those made by adsorbing alkanethiols on single crystal surfaces have been more frequently studied and, chemically modifying the end of a DNA single strand with a thiol group, a Self Assembled Monolayer of DNA on a gold surface where thioloxidizes and bends to the single gold crystal,can be formed where the strands, inside the monolayer, can interact through electrical and Van der Waals interactions.

Another, most relevant feature for this work is that DNA is a highly charge polyelectrolyte. As already stated, DNA is basically a polymer of nucleotides which are held together by covalent bonds formed between the phosphate groups, each of which forms an ester with a hydroxyl group of the pentose of the next nucleotide.This involves two of the three OH groups of the acid, leaving the last one free to ionize. This ionization leaves a negative charge on each phosphate group [82]. Such molecular structures can be used to detect complementary DNA (or RNA) strands in solution and to bind antibody DNA-conjugates in bioanity assays for novel applications, ranging from the study of protein networks to monitor the progress of diseases.

2.3 An insight on SAM formation

Self-assembly forms the basis for many natural processes including protein folding, DNA transcribing and hybridization, and the formation of cell membranes. The process of selfassembly in nature is governed by inter- and intra-molecular forces that drive the molecules into a stable, low energy state.These forces include hydrogen bonding, electrostatic interactions, hydrophobic interactions, and van der Waals forces.

In the 1980's, scientists discovered that alkanethiols with dierent chemical endgroups spontaneously assembled on noble metals. This new area of science opened the doors to a simple way of creating surfaces of virtually any desired chemistry on a gold substrate. This results in crystalline-like ordered molecular assemblies formed on the metal surface, called self-assembled monolayers (SAMs). Over the years, the

mechanism of the self-assembly process has been well studied and elucidated. Strong and Whitesides[43],via electron diraction studies of high density monolayers,have found that a typical alkanethiol monolayer forms a ($\sqrt{3} \times \sqrt{3}$ R30°) structure on Au(111) with the thiol chains tilted approximately 30 degrees from the surface normal.

As with self-assembly in nature, there are several driving forces for the assembly of thiols onto noble metal surfaces. The rst is the anity of sulfur for the gold surface. Dubois et al., have found that the sulfur-gold interaction is on the order of 45 kcal/mol[44], forming a stable, semi-covalent bond, in comparison, the $C-C$ bond strength is ~ 83 kcal/mol.

The next driving force for assembly is the van der Waals interactions between the methylene carbons on the alkane chains. For alkanethiol monolayers,this interaction causes the thiol chains to tilt in order to maximize the interaction between the chains and lower the overall surface energy[45].

An alkanethiol is compound containing an alkyl group ($-C_xH_{2x+1}$) joined to a mercapto group ($-SH$). The substrate here discussed is Au(111).

Each alkanethiol chain can be divided into three parts:

- headgroup (linking group) which guides the self-assembly process on each type of substrate through a strong bond;
- the backbone (main chain) that interacts with other chain backbones via van der Waals and hydrophobic forces.This ensure an ecient packing of the monolayer and contribute to stabilize the structures;
- the specic terminal active group which confers specic properties to the surface and is able to bind dierent molecules by weak interactions or covalent bonds.

In the case of SAM-alkanethiol, the reaction may be considered formally as an oxidative addition of the S-H bond to the gold surface, followed by a reductive elimination of the hydrogen.

From Figure 2.6a), we can follow the steps of how a SAM composed of alkanethiol chains on Au(111) forms as a function of deposition time[46]:

1. Physisorption. Upon thiol dosage there is an initial physisorption step. The physisorbed state on Au(111) can be described as a gas-like, highly disordered system;

2. Lying down phase. After physisorption, thiol molecules chemisorb on the Au(111) substrate through the sulfur headgroup in a process that takes at least some minutes. During the process the thiol molecule loses the mercaptan H atom,transforming itself in a thiolate. This kind of nucleation happens easier at Au step edges and forms islands composed of adsorbed chains. The phase is called "lying down" because the axis of the chain is parallel to the substrate;

3. Nucleation of standing up phase. After nucleation, the islands grow and there is the increase the surface coverage ofthiolate species on the Au surface. "Standing up" is referred to molecules which have their axis perpendicular to the substrate. This phase is governed by the balance between intermolecular and molecule/substrate interactions and the gold surface response to the chemisorption process. The competing forces that determine the SAM ordered structure are the interaction between the headgroup and the substrate,which involves a large chemisorption energy (30 kcal/mol), and the interchain van der Waals forces. Although van der Waals interactions are weak with respect to chemisorption ones, they inuence and stabilize molecular self-assembly.

4. Standing up phase. The self-assembly takes place in two consecutive nucleation and growth processes. The standing up is the second one and it leads to rotated domains of lying down molecules, and later to domains of standing up molecules, irrespective of the environment used for SAM preparation.

The self-assembly takes place in two consecutive nucleation and growth processes that lead to rotated domains of lying down molecules, and later to domains of standing up molecules, irrespective of the environment used for SAM preparation.

From the alkanethiol SAMs the extension to DNA-SAMs was easy: chemically modifying the end of a DNA strand with a thiol group permits to form a Self Assembled Monolayer of DNA on a metal surface where thiol oxidizes and bends to the metal, with the strands interacting through electrical and Van der Waals interactions. The main dierence is that DNA is negatively charged and, in order to screen the negative charge of DNA backbones, a saline buer solution is usually used. In fact positive ions of saline solution shield the DNA chains electrostatic repulsion and allow the SAM to form.

Furthermore, alkanethiols are smaller than DNA chains and these last have steric eects which dene the structure of the DNA-monolayer far less packed than thiols-SAM[47]. In addition, DNA-SAM can adsorb on the surface also via aspecic bond

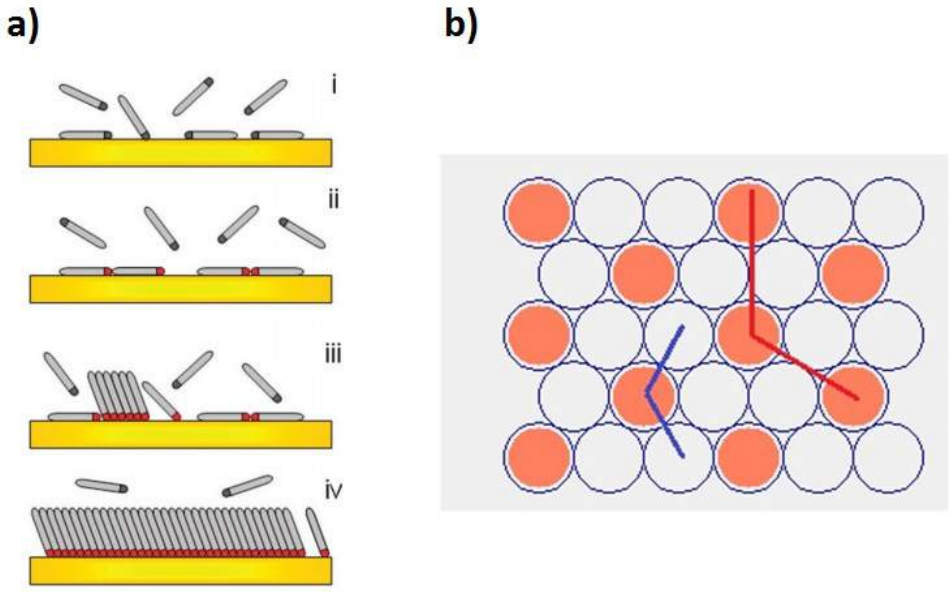

Figure 2.6: a) Scheme of the dierent steps taking place during the self-assembly of alkanethiol on Au(111): (i) physisorption, (ii) lying down phase formation, (iii) nucleation of the standing up phase, (iv) completion of the standing up phase[46]b) commensurate $\sqrt{3} \times \sqrt{3}$ R30° structure on Au(111). Blue lines are primitive vectors of the substrate and red lines are the primitive vectors of the adsorbate lattice that are larger and rotated with respect to the blue ones. Image courtesy of Serena Alfarano.

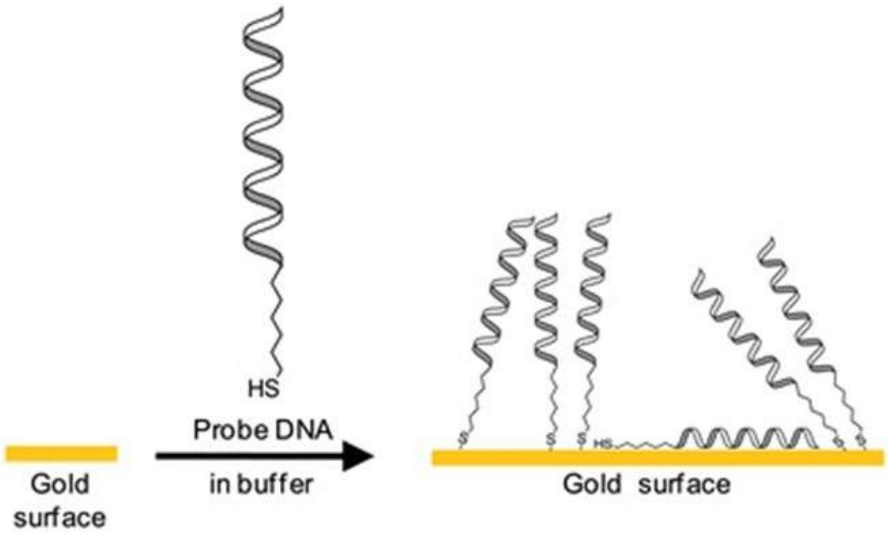

Figure 2.7: Representation scheme ofDNA-SAM on gold surface. DNA is a thiol-modied oligonucleotide that can be adsorbed on the surface via specic and aspecic bonds.

(cross-linking bases), which means that DNA can physiadsorbed to the gold surface via N-Au bonds (see Figure 2.7 for a representation scheme). This last case of physisorption bonding, usually occurs at energy of 6 kcal/ mol, at variance with a chemiadsorption bonding S-Au at higher energy (30 kcal/ mol)[45].

2.4 ssDNA-SAM Density

The density of our ssDNA-SAM in solution can be controlled varying the incubation time, that is the time that the solution, containing a given concentration (1 μM in our case) of thiolated DNA molecules, is left in contact with the Au(111) surface of the WE. Obviously, increasing the incubation time more dense will be the DNA-SAM layer. Principally we used in this work two dierent incubation times: low density SAM (LD-SAM) realized keeping the samples in contact with the functionalizing solution for 10/15 min whereas high density SAM (HD-SAM) formed increasing the time to 70 min.

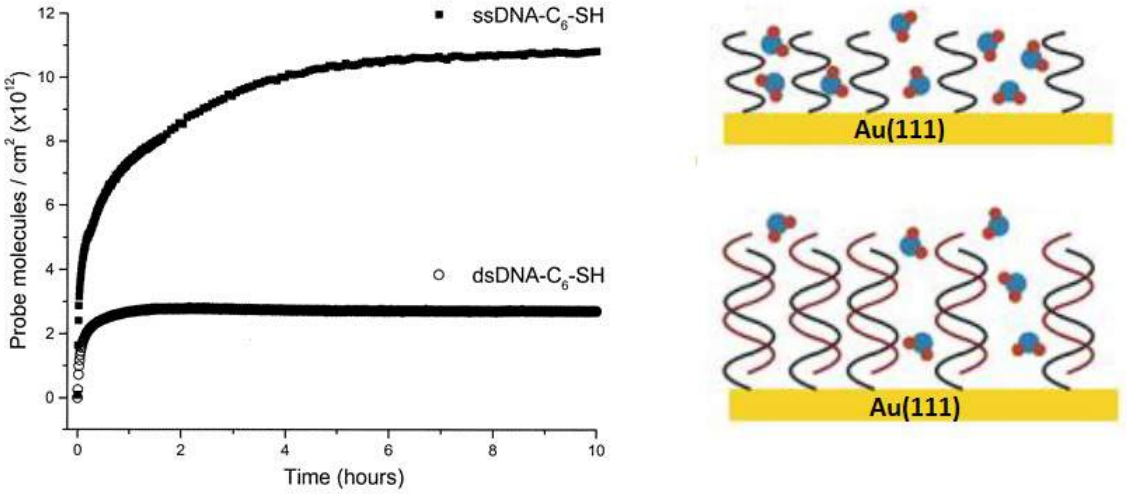

Figure 2.8: Georgiadis et al. results[48]: ssDNA and dsDNA exponential density behavior as function of incubation time.

Both single-stranded and double-stranded SAMs-DNA show the same density vs incubation time trend (see Fig. 2.8), that Georgiadis et al. recognized as an exponential function of the incubation time, making use of a two-colors SPR (Surface Plasmon Resonance) to estimate the SAM density and to characterize it[48]. In their studies, they demonstrated that lower ionic strength solutions correspond to less probe adsorption

(due to the electrostatic repulsion between DNA strands) whereas, higher ionic strength solutions are associated to higher probe coverage. Moreover, at a lower ionic strength adsorption is slower in the first few hours than at higher ionic strength. This is due to electrostatic phenomena connected to the Debye's length of the solution.

In order to quantify the density of ssDNA layer autoassembled on the surface of WE, XPS measurements were carried out. The idea was based on the experiments of Tarlov and co-workers[49] and the density results were compared with those obtained by Georgiadis et al.[48]. Different incubation times has been considered: 5, 12, 20 and 30 minutes, 1, 3, 5 and 24 hours.

The analysis were performed onto nitrogen spectra N1s. They are univocally related to the presence of DNA on Au(111): so spectra were taken in the binding energy range 390-410 eV, because N1s peak is centered at 395 eV. The 24 hours incubation was selected as reference density and it is associated to the maximum possible density for ssDNA and all spectra are normalized with respect to it. In fact, at sufficiently high probe densities, DNA is expected to be in the strongly charged regime of polyelectrolyte brushes ([50, 51]).

The electrodes were post-treated for 1 h in contact with a solution of TE NaCl 1 M containing mercaptohexanol (MCH) 1 mM. MCH-molecules chemisorbed onto the surface through S-Au bond ensuring the displacing of aspecic ssDNA bonds. We have chosen to work in this way because the XPS data analysis model can be simplified by excluding those nitrogen bases of the molecules laying down on the surface which will not participate in DNA-hybridization processes.

The ssDNA-SAM probe density was calculated assuming an hexagonal package for DNA onto Au(111) (see Figure 2.9): DNA is treated as a solid and rigid chain of diameter 1nm, it can be done because the high density structure forces DNA strands to stand up from the surface. Steric interaction are taken in account assuming that DNA strands in HD phase locate themselves at a minimum distance of 2nm[52].

The measurements were performed using a conventional Al K_α source with an electron pass energy of 20 eV. The spectra were collected as the sum of following scan on an energy window of 20eV and sampled with a step of 0.1 eV and with a time of 500 ms. For each sample the Fermi level (that should be positioned at binding-energy 0 eV) was taken and all spectra were thus rescaled with respect to it.

XPS spectra for Nitrogen 1s are analyzed using a Voight prole estimating the area of the selected peak. Graphs in Figure 2.10and Figure 2.11 show the peak intensity associated to N1s for a samples in contact with the functionalizing solution for 24 hours,

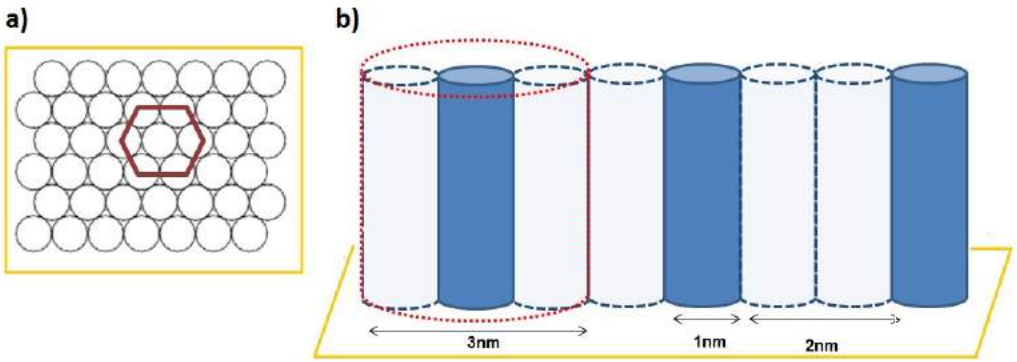

Figure 2.9: a) Top view of hexagonalpackage ofssDNA molecules (cylinder) on gold surface. b) ssDNA molecules (solid blue cylinder) are large 1nm and because of coulomb electrostatic repulsion they are separated by 2nm distance (transparent blue dotted cylinders). Image courtesy of Serena Rosa Alfarano.

and the nal density evaluated for each incubation time, respectively.

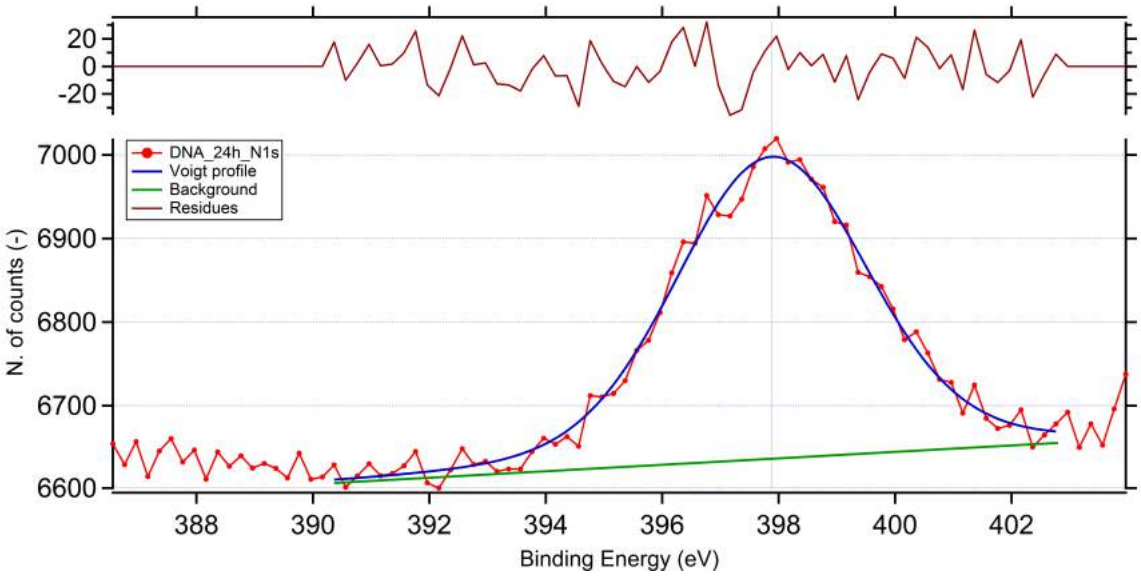

Figure 2.10: N1s peak for a sample incubated for 24 hours and t with a Voight function.

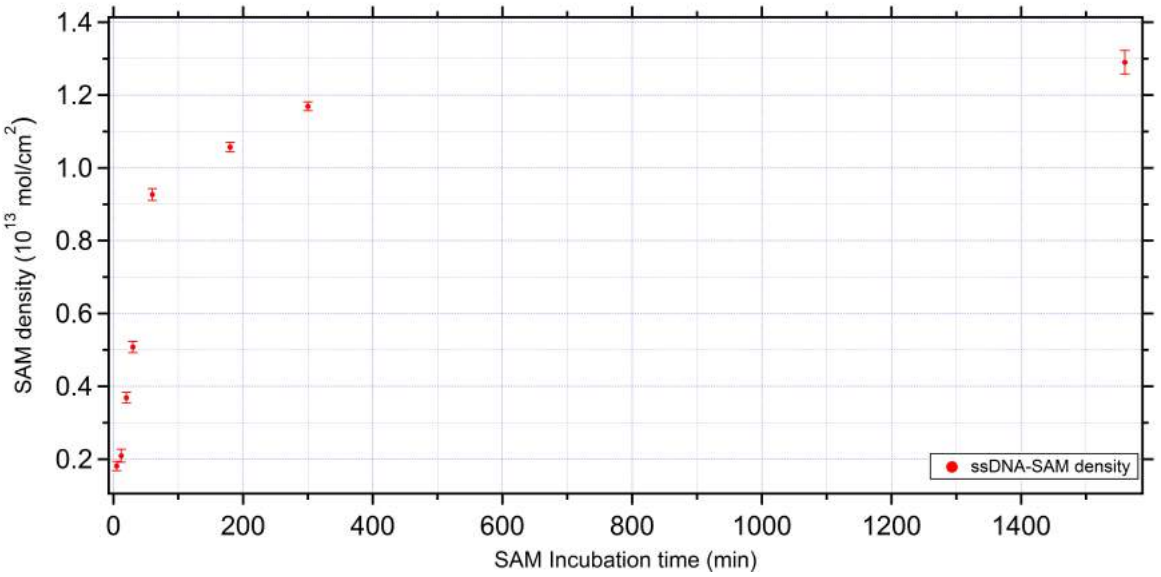

Figure 2.11: ssDNA density as function of incubation time. Results are comparable with those obtained by Georgiadis et al.[48].

2.5 Experimental procedures

DNA functionalization of the gold electrodes was carried out using the well-established procedures for single stranded (ss) DNA[2] self-assembled monolayers on gold ([37, 48]). The electrodes were wetted for 12 min, with a drop of 1 µM thiolated (C6) ssDNA ($HS-(CH_2)_6$-5'-ctt atc gct tta tga ccg gac c-3', called F5-SH) in a high-ionic-strength buer TE NaCl 1 M at pH 8. In this way a low density ssDNA SAM ($2.1 \pm 0.4 \times 10^{12}$ molecules/cm^2) was obtained (more details can be found in Section 2.4 and according to[48]). After DNA-SAM formation, in order to remove aspecically bound DNA-molecules, the electrodes were thoroughly rinsed with the same buer solution, at physiological concentration, used for the measurements,e.g. KCl 100 mM, PBS 1x, etc. Then the dierential capacitance at the electrode-electrolyte interface was measured. Hybridization was performed by wetting the functionalized working electrodes with a drop of the same buer solution containing the complementary DNA strand (5'-ggt ccg gtc ata aag cga taa g-3', called cF5), in dierent concentrations. The used 44-mer ssDNA oligonucleotide has a sequence ($HS-(CH_2)_6$-5'-caa aac agc agc aat cca aag atc aga cac ccg att aca aat gc-3', called dpnII_SH).

[2] The used DNA-molecules were purchased from Biomers.net GmbH, unless otherwise stated

We chose to work at low surface probe densities because, in this way, electrostatic and steric eects are minimized and a complete hybridization and relatively fast kinetics can be achieved. Instead, in a high density regime, experimental measurements have revealed a strong suppression of DNA target hybridization ([37, 48, 53])Moreover, we noted that a further passivation treatment of the surface of the electrode with molecules as MCH-molecules, prevented the detection of the DNA-hybridization masking the signal and thus reduced the sensitivity of the device.

In the DNA/miRNA hybridization experiments performed here, the DNA sequence ($HS-(CH_2)_6$-5'-cga agg caa cac gga taa cct a-3') was chosen to be complementary to a miRNA target namely hsa-miR-154-5p (5'-uag guu auc cgu guu gcc uuc g -3'), up-regulated in heart failure ([54, 55]). In addition, a murine miRNA, mmu-miR-351-5p (5'-cag gct caa agg gct cct cag gga-3'), was used as negative control and complementary to the ssDNA sequence: mmu-miR-351-5p-comp-SH ($HS-(CH_2)_6$-5'-cag gct caa agg gct cct cag gga-3').In these experiments the miRNAs detection was performed in buer solutions (PBS 1X, KCl 100mM) and human extract and then implemented in human plasma samples having dierent levels of heart failure.

All the used oligonucleotide-molecules were purchased from Biomers.net. A complete list of oligonucleotide sequences and nomenclature can be found in Figure 10 in Appendix D.

2.5.1 De-hybridization protocols for device regeneration

Thermal de-hybridization cycles were introduced to test the reusability of the device. The thermal treatment in the case of DNA/DNA hybridized SAM on the WE, in buer solution, consisted of sample incubation in a basic solution ($pH = 9$) of TE buer for 1 hour in oven at a temperature 10° C higher than the melting temperature of the specic DNA sequence (e.g.55°C for the sequence F5 previously introduced).

In the case of DNA/miRNA SAMs hybridized in human plasma samples a two-step cleaning protocol was used: the electrode was rst soaked in a PBS plus Tween 1.25% solution for a time dependent on the miRNA buer dilution used, before proceeding with the previously described thermal treatment.

Chapter 3

A Biosensor for Direct Detection of DNA Sequences

As already mentioned in the introduction, the nal goal of this work is to produce a portable capacitive device to be used as a point-of-care medical diagnostic tool. Towards this goal, the unique biomolecular recognition properties of DNA are exploited to detect genomic biomarker with high anity. To optimize the sensitivity of the device we investigated DNA-SAM electrical properties using dierent physiological conditions mimicking the complexity of blood composition. After ssDNA-SAM characterization, the hybridization process has been characterized, in the case of fully- and partially-matching target DNA sequences.

3.1 DNA-SAM Electrical Characterization

As already stated in Section2.1 Electrochemical Impedance Spectroscopy (EIS) measurements were performed on a three-electrode conguration to characterize the DNA SAM.

The WE and CE are microfabricated gold electrodes, immersed in an electrochemical pool, whereas the RE is a classical mm-sized Ag/AgCl pellet electrode accessing the experimental pool from the top. As in a normal electrochemicalsetup, the potential is applied across WE and RE while the current, owing in the experimental pool, is measured across WE and CE. In order to compare our measurements with standard conditions in electrochemical setups, the RE was calibrated with respect to a standard

Ag/AgCl RE (sRE) placed in a solution of saturated KCl 3 M. Practically, we measured the open circuit potential (OCP[1]) of our RE with respect to the sRE (ΔV_{Re-sRE}) in the dierent working buer solutions used in this thesis-work. In this way, we can relate the potentials measured in our setup to the sRE (ΔV_{WE-sRE}) according to the following equation:

$$\Delta V_{WE-sRE} = \Delta V_{WE-RE} + \Delta V_{RE-sRE} \quad (3.1)$$

where ΔV_{WE-RE} is the bias potential measured between WE and RE. In this way we derive the correcting parameter to set in the bipotentiostat control software to assure a ne control of the applied potential during the whole experiment and to allow a direct comparison with other data available in literature.

After this calibration, we tested the eect of the applied potential (details in section 3.1.1) and of the buer conditions (see section 3.1.2) on the measurements of DNA-SAM capacitance. To optimize the conditions for best DNA hybridization, dierent SAM densities were exploited.

3.1.1 The eects of the Applied Potential on the ssDNA-SAMs

Prior to SAM-formation we treated the gold surface with plasma etching which makes the surface at and smooth (0.5 nm roughness, as measured with Atomic Force Microscopy). Then, we prepared the DNA-SAm as described in section 2.5, using the sequence F5-SH. Capacitance measurements as a function of the applied potential were performed in KCl 100 mM buer solution, as described in section 2.1.

In Figure 3.1a) we show, as an example, the dierential capacitance measured for a low density (LD) ssDNA-SAM obtained by incubated 1 µM of ssDNA for 12 minutes and applying a bias potential ranging from 10 mV to 100 mV. C_d has been measured for more than a hour, to prove the stability of the system.

From the solid red line in Figure3.1b), we noticed a sharp increase of the capacitance, raising the applied potential from 25 mV to 100 mV. This sharp change of C_d can be related to thiols desorption which led us to terminate the measure in order to avoid SAM damaging. At this point, EIS measurements with dierent applied potential at dierent densities were carried out.Figure 3.1b) show the dierential capacitance measured for

[1] is the potential across WE and RE, for which no current ows across WE and CE.

six dierent ssDNA-SAM densities obtained with six dierent incubation times: 12, 15, 20, 30, 45 and 70 minutes, as described in Section 2.4.

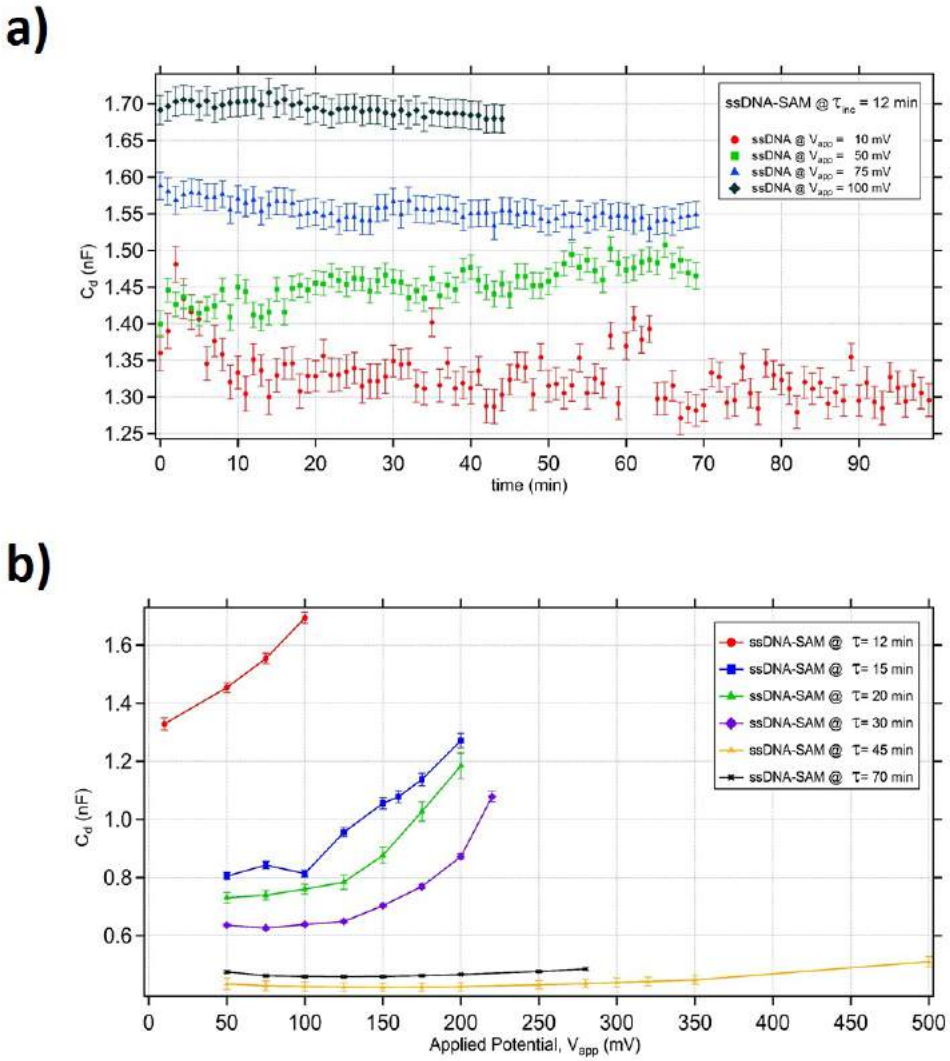

Figure 3.1: a) Dierential capacitance measured for a low density (τ_{inc} = 12 min) ssDNA-SAM in KCl 100 mM at four dierent amplitudes for the applied potential: 10, 50, 75 and 100 mV. b) Dierential capacitance, C_d vs the amplitude of applied potential (V_{app}) in KCl 100mM at six dierent incubation densities, from the top, density with 12 minutes of incubation, then 15 minutes, 20 minutes, 30 minutes, 45 minutes and 70 minutes. Increasing the SAM-density we can observe a decrease of C_d; furthermore, in each case, for larger applied potential the measured capacitance is larger.

From Figure3.1a) it is evident that higher potentials correspond to higher C_d, and

that the system is stable vs time at each of the applied potential. In Figure3.1b) we checked further the eect of the potential on SAM of dierential densities. The curves of 3.1a) correspond to the same LD ssDNA-SAM of the top red curve of 3.1b). The lowest two curves (dark green and orange markers) correspond to a high density (HD) DNA-SAM, obtained through a DNA incubation of 70 minutes. While HD SAM can support applied potential as high as 400 mV,for LD SAM a potential higher than 100 mV is already inducing a slow desorption of SAM molecules, as can be seen from parallel AFM measurements. A dependence of the DNA-SAM stability to the applied bias on the SAM density is not new in literature: LD SAMs have a poor degree of order, are not stabilized by intermolecular interactions, and their desorption eciency is higher[56, 57].

The monotonic decrease of the dierential capacitance by increasing the ssDNA-SAM density observed in Figure 3.1b), can be explained through the planar approximation (cf. Eq.2.2) used to describe C_d. According to this equation and since A_{WE} remained constant for all devices, C_d variations depend mainly on changes in the height of the molecular layer, d, and variations in the dielectric constant. As already said, LD DNA-SAMs are less packed ([35, 37, 47, 48]) and much less ordered than HD DNA-SAMs. This corresponds to a higher free volume of individual ssDNA molecules, pinned to the gold surface through the thiol linker. As a consequence, the corresponding average height of the SAM is lower, the lower is the density. In turn a lower DNA density allows a greater number of water molecules to penetrate the monolayer, contributing more and more to the total dielectric constant of the area close to the electrode, probed by our measurements.The cartoon in Figure 2.8 provides a graphical representation of the LD and HD-SAMs, and of the water molecules in between.

The eect of C_d increase with the applied potential, at a given DNA-SAM density, is instead due to polarization eects. The bias potential polarizes the hydrated ions[58, 59] within the layer closed to the electrode surface increasing the dielectric constant. To prove the role of the hydrated ions polarization in C_d measurements, the complex dielectric permittivity of KCl 100 mM buer solution has been measuring the electrical response ofbare gold electrodes upon varying the amplitude of the applied potential. These experiment are reported in Figures 3.2a) and b). Using the approximation 2.2, assuming the thickness of the layer equal to the Debye length of the solution, the dielectric constant value at each applied potential is estimated.

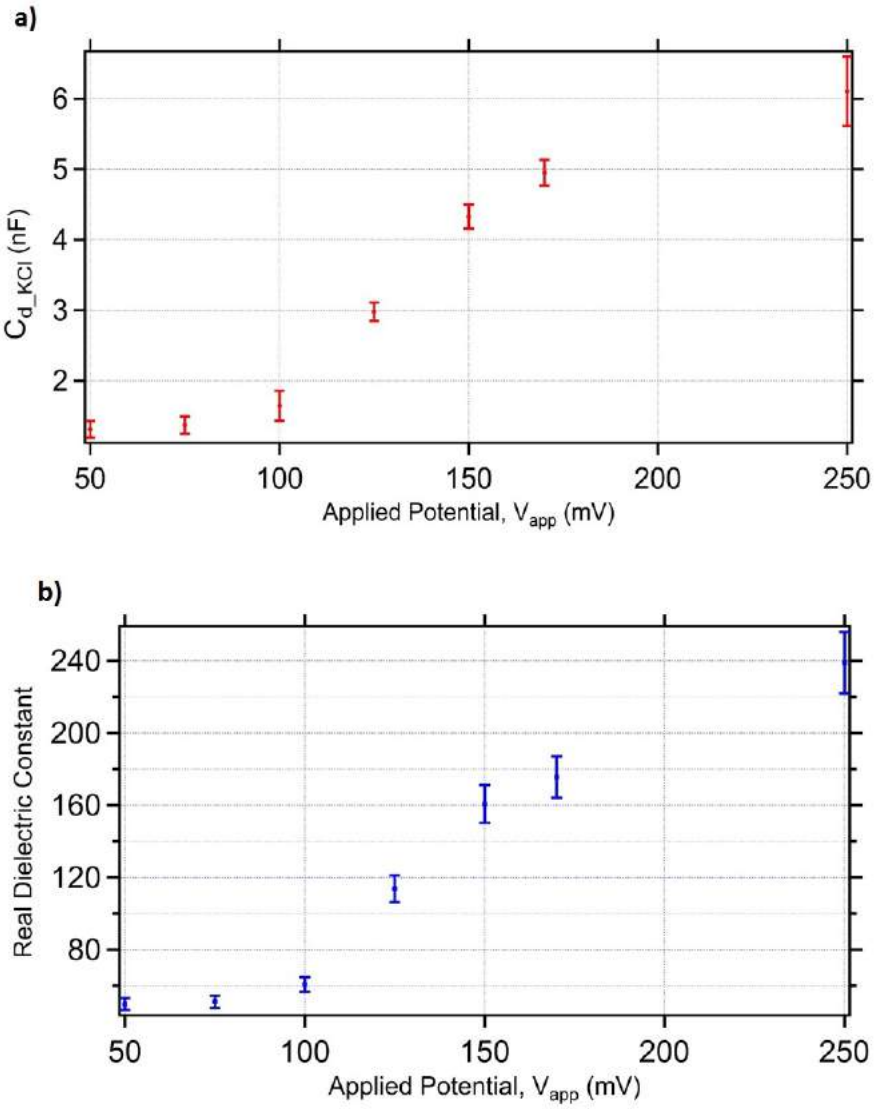

Figure 3.2: Bare electrodes measurements carried out in KCl100 mM: a) Dierential capacitance as function ofthe applied potential. b) KCl-doped aqueous solution's dielectric constants showing their trend with a more and more high applied potential.

The study of the polarization in electrolyte solutions is not at the core of this thesis and thus we will not discuss here in details. References [59,60, 61] are given for more details and the mathematical approaches.

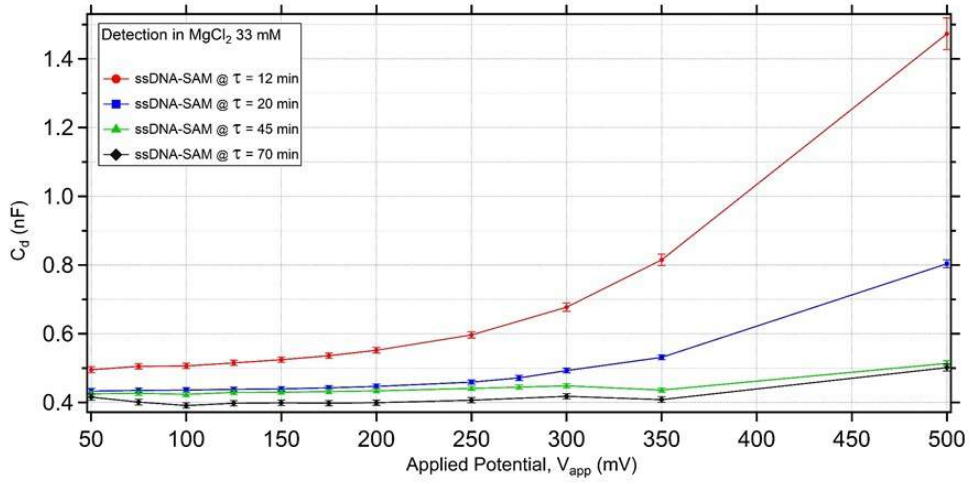

Figure 3.3: a) Dierential capacitance, C_d vs the amplitude of applied potential (V_{app}) in $MgCl_2$ 33mM at four dierent incubation time, going down from the red curve at the top of the graph, density with 12 minutes of incubation, 20 minutes, 45 minutes and 70 minutes. The slow increasing of the capacitance as function of the applied potential for each SAM density is due to the double charge of the ions which screens the eect of the potential. b) ssDNA with 44bases.Total capacitance as function of the applied dierent potential in a buer solution of KCl 100mM. Dierent densities are explored. From the top: density with 15 minutes of incubation, then 45 minutes and 70 minutes. In each case increasing the applied potential, a higher capacitance is measured. Lines are guides for the eye

3.1.2 Divalent salt eects

Experiments similar to the ones described in the previous paragraph were carried out in the case of a divalent salt $MgCl_2$. To get a direct comparison with KCl 100mM, we chose kept the ionic strength the same, choosing a solution of $MgCl_2$ 33 mM in order to have the same ionic strength.

The overall results are similar to what already found (cf. Figure 3.3a)): applying larger potential, we can observe an increase in the measured dierential capacitance. The dependence of the voltage, also in this case, is more evident at lower DNA densities. Although the two buers have the same ionic strength, the screening eect of Mg^{2+} ions is higher than for K ions because of their dierent size and dimension of the hydration shell, and because of the dierent valence. This leads to the formation of a more compact

ssDNA monolayer in the case of $MgCl_2$ solutions [62, 63]. As a consequence, we observe a slower increasing of C_d as function of the applied potential for each SAM density due to a more eective screening the DNA backbone.

3.2 The biophysics of DNA hybridization

After the electrical optimization of the ssDNA-SAM and of the read-out conditions as explained in the previous section 3.1, we concentrated on study of the kinetics of DNA hybridization. The capability of detecting DNA hybridization in real time and in-situ is of critical importance for applied genomics, drug discovery, gene expression proling and other applications. These studies are based on the detection of interactions between oligonucleotides immobilized on the solid support, or probes, with analyte target nucleic acids present in solution. Binding, or hybridization, between probes and targets to form an immobilized duplex depends on the degree of complementarity between the probe and target base sequences and on the steric availability of the surface-immobilized probes.

Many techniques have been employed in order to study DNA-hybridization [64, 65, 66], including EIS-experiments [67] but never in-situ, i.e. following the process while occurring, nor in capacitive conditions. As we will show in this chapter, monitoring C_d as a function of hybridization time will give us additional information to be used in DNA-detection.

To detect DNA hybridization, we proceeded as follows: the WE was functionalized with a low-density ssDNA adopting the procedure described in Section 2.5. The average C_d value measured in 100 mM KCl saline buer at 10 mV applied potential was (1.06 ± 0.01) nF. An example of this type of measurement is shown in Figure 3.4, red curve. From the measured C_d, we estimated a capacitance density at the working electrode of $\approx 10\ \mu F/cm^2$, in agreement with the literature [41] and with the theoretical value extracted from eq. 2.2. In fact, assuming a SAM-height of 2.38 ± 0.07, as determined via AFM measurements [38], and using the ssDNA dielectric constant values found in literature ([68, 69, 70, 71]), a C_d variation between 0.6 nF ($_{ssDNA} \approx 20$) and 2.3 nF ($_{ssDNA} \approx 78$) was expected. Furthermore, the measured height is consistent with the polyelectrolye brush theories. In particular, in our salted brush regime, the concentration of added salt is approximately the same inside and outside the brush, and the thickness of the layer is dominated by excluded volume interactions between the DNA laments.

As a result, the height depends on the SAM density (ρ_{SAM}) and salt concentration (C_0) according to:

$$h \sim \left(\frac{\rho_{SAM}}{C_0}\right)^{1/3} \simeq 2.18 \pm 0.41 \text{ nm} \qquad (3.2)$$

Attested the stability of the signal, the ssDNA SAM hybridization kinetics was then followed in-situ, in real-time. The C_d variation due to strand pairing is represented by the blue curve of Figure3.4, for the case of 10 pM complementary DNA in same salt solution. To follow hybridization kinetics, we initially measured at a rate of 4 measurements/min for 15 min, then we slowed down to 1 measurement/min untill the C_d dierential variations between successive points were lower than 6% which we considered to be the steady-state of our measure. The two dierent sampling steps are due to the need to highlight the part of the hybridization process more specically connected to the direct channel of DNA-hybridization (target approaching directly from solution, without diusing along the surface. More details can be found in Chapter 4).

The C_d measured at steady-state was (0.918 ± 0.001)nF for this concentration of complementary DNA, which correspond to a decrease in capacitance of 13.4% upon DNA hybridization. The lowering of the capacitance upon hybridization can be explained by the height increase of the SAM upon hybridization, due to the dierent persistence length[2] of ss- and dsDNA, and by the replacement of water molecules (with a high dielectric constant, $\varepsilon_{H2O} \simeq 76.7 \pm 0.2$, for 100 mM KCl-doped aqueous solution[72]) with DNA strands (lower ε) upon DNA pairing.

After this rst proof of principle, we proceeded with DNA-hybridization in real time.

As a rst step, the device was calibrated for DNA/DNA hybridization in the same experimental conditions exploring the dynamic range of detectable complementary DNA concentration over 6 orders of magnitudes, from 1 pM to 100 nM. The reusability of our three-electrode sensor obtained by using the thermal regeneration procedure described in Section 2.5.1, is shown in 3.5.

At each cycle, the C_d value after thermal regeneration recovers the initial C_{ssDNA} value with an error ranging from 1% to 3% (Table 3.1) attesting that the used protocol does not damage the ssDNA probe layer on the electrode, despite of the long measuring

[2]Dened as the length beyond which the polymer direction is becoming random. From literature ([37, 66]) we know that the persistence length of ss- and dsDNA amount to $p \approx 1$ nm and $p \approx 50$ nm, respectively

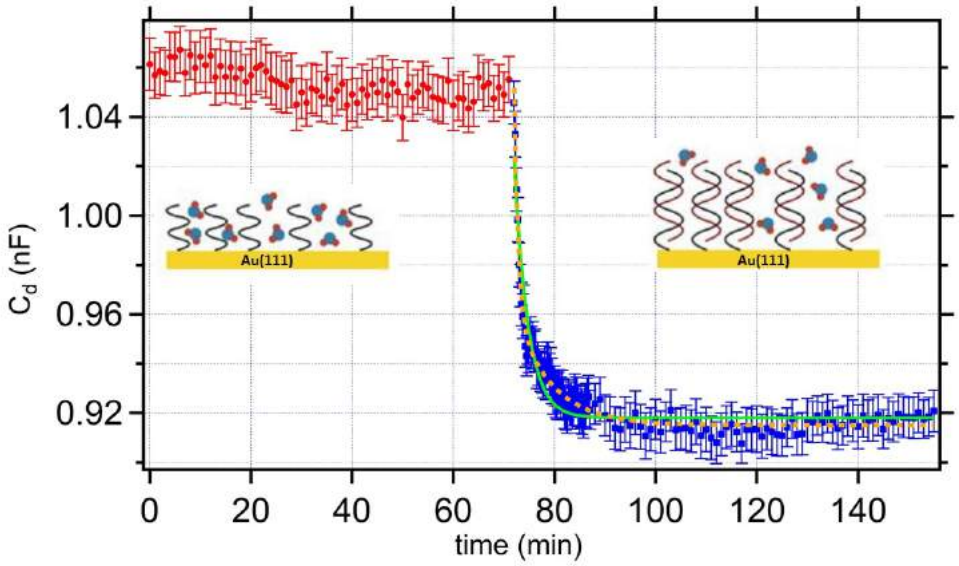

Figure 3.4: Kinetics of DNA-hybridization via dierential capacitance measurements. The red signal represents the dierential capacitance of a low density ssDNA SAM functionalized WE measured in KCl 100 mM and applying 10 mV of bias. The hybridization (blue points) was per-formed by adding in the experimental pool 10 pM complementary DNA. Cartoon-insets show the variation of thickness and dielec-tric constant between a layer of ss- (on the left side) and dsDNA (on the right side), respectively. The green and orange-dotted lines represent the ts based on rst-order Langmuir adsorption kinetics and double exponential kinetics, respectively.

time, approximately 20 hours. Hybridization was then performed after each regeneration cycle, using dierent concentrations of complementary-strand DNA (from 1 pM to 100 nM, see Figure 3.5), monitoring the dierential capacitance at the WE versus the incubation time. At each hybridization process, the measurements were run until the C_d dierential variations between successive points were lower than 6%, as just explained. Such steady-state C_d values, named C_{dsDNA}, are shown in Table 3.1. These equilibrium C_d-values are monotonically inversely proportional to the used concentration of DNA target. This can be rationalized considering that the capacitance decrement is proportional to the number of hybridized sites at the electrode as can be described by the following adsorption model[73]:

$$\theta(t) = \theta_{max} \frac{(k_{on} \cdot [cDN\,A])^a}{k_{off}^a + (k_{on} \cdot [cDN\,A])^a} \tag{3.3}$$

where θ_{max} is the maximum probe coverage, k_{on} and k_{off} are the adsorption and

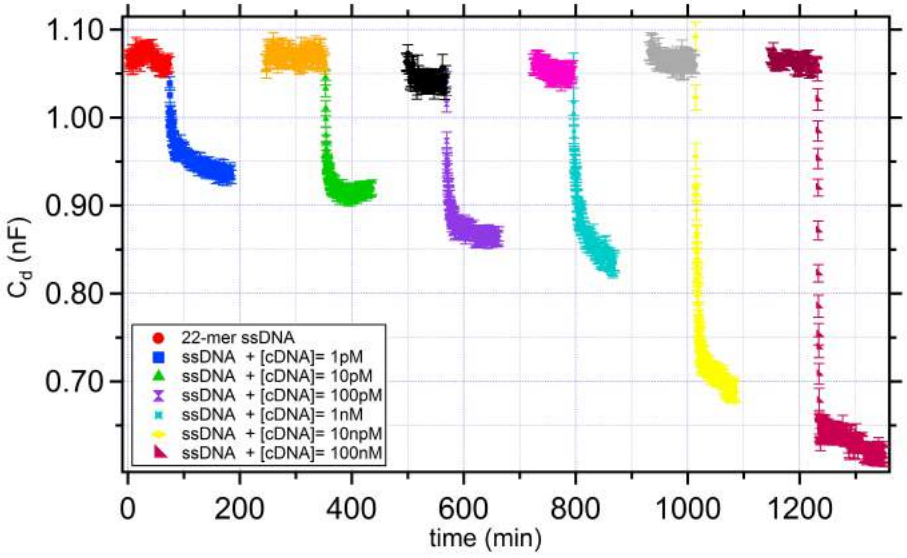

Figure 3.5: Hybridization and de-hybridization cycles on the same low density ssDNA SAM in KCl 100 mM. The [cDNA] concentration increases for every prole by one order of magnitude going from the blue curve (1 pM) to the right of the graph, mauve curve (100 nM). In the time scale (x-axis), it was considered the time delay necessary for the thermal regeneration of the electrodes.

desorption rate constant, respectively.

[cDNA]	C_{ssDNA} (nF)	Δ_{ssDNA} (%)	C_{dsDNA} (nF)
1 pM	1.07 ± 0.01	1.7	0.93 ± 0.01
10 pM	1.08 ± 0.01	2.5	0.92 ± 0.02
100 pM	1.02 ± 0.02	2.9	0.89 ± 0.01
1 nM	1.05 ± 0.01		0.83 ± 0.01
10 nM	1.06 ± 0.01	0.4	0.69 ± 0.01
100 nM	1.06 ± 0.01	0.4	0.61 ± 0.01

Table 3.1: Dierential capacitance measured at the ssDNA functionalized WE before ($C_{d-ssDNA}$) and after hybridization process, $C_{d-dsDNA}$. The experiments were carried out on the same regenerated SAM-probe lm for all the six dierent [cDNA] shown in Figure 3.5.

Note that this adsorption model in the limit where a = 1 reduces to the well-known Langmuir model where all probe sites are energetically equivalent, independent and available for binding. When a 6= 1 the equation describes a heterogeneous adsorption

isotherm where the degree of heterogeneity (distribution of binding energies) increases as the value of a decreases.

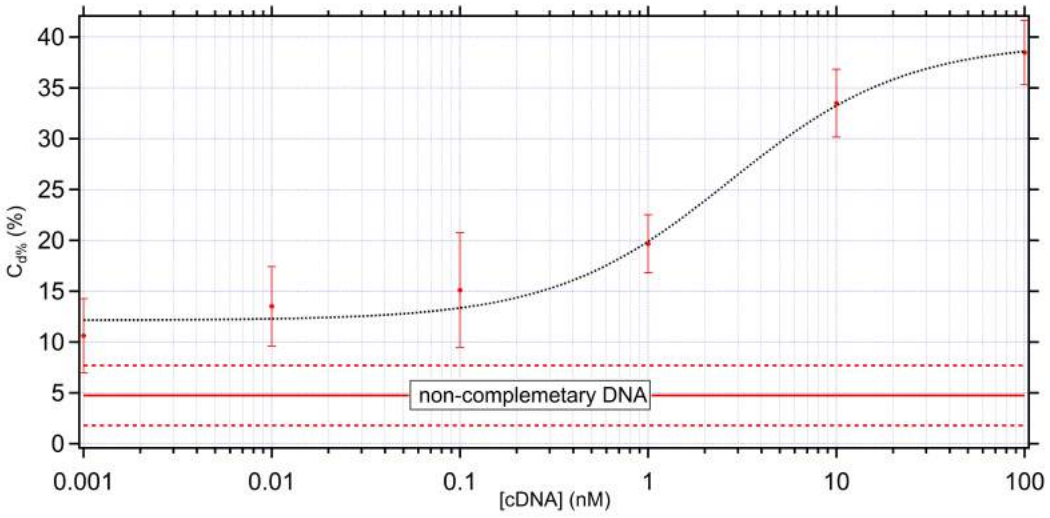

Figure 3.6: Calibration curve of the three-electrode device. The response is shown as percentage capacitance variation upon hybridization of the ssDNA-SAM WE, as a function of the complementary DNA concentration in solution (KCl 100 mM) and tted with a Hill equation (dotted black curve). The solid red line represents the average variation of C_d when a non-complementary DNA is present in solution at high concentration (1 µM), whereas the dashed red lines represent 3 standard deviations around this value.

In addition, the maximum variation of C_d upon hybridization, $C_{d\%}$ (calculated from C_{ssDNA} to C_{dsDNA}) can be obtained and its plot versus the concentration of the complementary DNA in solution, [cDNA], is shown in Figure 3.6. Fitting such data, one can further compute the anity constant, $K_A = \frac{k_{on}}{k_{off}}$, for DNA-hybridization. If we suppose in fact, that the DNA-pairing on the gold surface can be described by Langmuir adsorption isotherm [48, 72], we obtain the following equation that connects the percentage change of C_d, the varying concentration of the complementary DNA in solution, [cDNA], and K_A [64, 67], dotted black curve:

$$C_{d\%} = \frac{K_A \cdot [cDNA]}{1 + K_A \cdot [cDNA]} \tag{3.4}$$

An anity constant for DNA hybridization $K_A = (0.35 \pm 0.09) \times 10^{9}\ M^{-1}$, corresponding to an equilibrium dissociation constant $K_D = K_A^{-1} \approx (2.8 \pm 0.7)$ nM, was derived. These values are in agreement with the literature [67, 74], where thiolated DNA

strands of similar length were adsorbed on a gold surface.

From data of Figure 3.6, a limit of detection (LOD) of 1 pM for the device is determined. This value is the smallest measured capacitance variation that can be unambiguously assigned to the hybridization process. Lower concentrations of [cDNA] in fact, lead to variations of C_d comparable to the control measurements, obtained for non-complementary strands in solution at high (1 µM) concentration. In gure this region is highlighted with a solid line comprised between the two dotted red lines that represent three standard deviations around this value. We think that once we will have improved our experimental setup (especially the functionalization step by employing gold nanoparticles, for example) the detection limit of these devices for DNA-hybridization will be pushed towards the fM-range. Nevertheless, the LOD obtained with our device is already a very good starting point for further measurements in more complex human environments.

Obviously so far we made the assumption that the DNA-hybridization follows a Langmuir kinetics. In the next section we discuss the applicapibility and the limit of this approximation.

3.3 Kinetics and Dynamics of DNA Hybridization

In order to get insights into the DNA hybridization kinetics, we t our data with the well-known Langmuir adsorption model. In this model the adsorption of adsorbate (A) onto the surface of the adsorbant or solute (S) can be described using the following three assumptions, (see Figure 3.7):

- The surface of the adsorbant, assumed homogeneous, is in contact with a solution containing an adsorbate which is strongly attracted from the surface;
- The surface has a specic number of sites where the solute molecules can be adsorbed and all sites are equivalent;
- The adsorption involves the attachment of only one layer of molecules to the surface, i. e. monolayer coverage only;
- The interactions between adsorbate molecules on adjacent sites are not permitted.

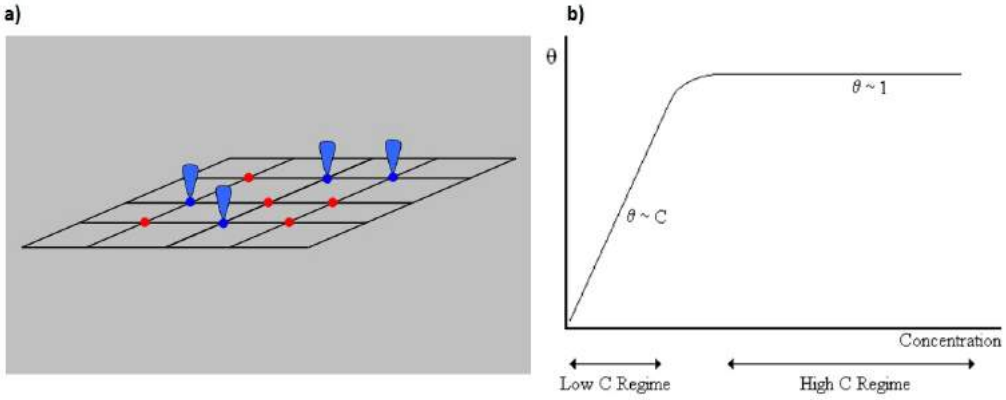

Figure 3.7: a) A schematic showing equivalent sites, occupied (blue) and unoccupied (red), in the Langmuir model. The adsorption sites (heavy dots) are equivalent and can have unit occupancyAlso, the adsorbates are immobile on the surface.Image courtesy of SmugBoy, https://en.wikipedia.org/wiki/Langmuir_adsorption_model. b) General form of the Langmuir Isotherm, the surface coverage, θ, with respect to the concentration of adsorbant in solution, http://infohost.nmt.edu/~jaltig/Langmuir.pdf.

Based on these points, adsorption can be described as a reversible process between adsorbent and adsorbate:

$$P + T \underset{k_{off}}{\overset{k_{on}}{}} H \tag{3.5}$$

where H represents a solute molecule bound to a surface site on T and k_{on} and k_{off} are the adsorption and desorption rate constant, respectively.

We introduce now the surface coverage, $\theta(t)$, which is defined as the fraction of the adsorption sites, occupied at time t, to which a solute molecule has attached. The forward adsorption rate to the surface should be proportional to a driving force times an area. The driving force is first order with respect to the concentration of the solute at time t, $C(t)$, and the area is proportional to the amount of bare surface which may be expressed in terms of the fraction of available adsorption sites at that time, $(1 - \theta(t))$. The desorption rate is first-order with respect to the amount of surface covered, $\propto \theta(t)$. So, the Langmuir kinetics isotherm can be expressed as:

$$\frac{d\theta(t)}{dt} = k_{on} \cdot C(t) \cdot (1 - \theta(t)) - k_{off}\, \theta(t) \tag{3.6}$$

Under the assumption that the capacitance change is directly related to the number

of occupied binding sites on the surface,it is possible to point out an equation, called Langmuir rst-order kinetics that describes the hybridization process on ssDNA in terms of dierential capacitance, experimentally measured:

$$C_d = C_{dsDNA} + C_0 \cdot \exp\left[-k_1 (t - t_0)\right] \tag{3.7}$$

Where C_d is the measured double layer capacitance, C_{dsDNA} is the capacitance reached by the system when the hybridization process reaches the equilibrium, when the number of strands that desorb per unit time is the same of the ones that hybridize, C_0 is the dierence between the capacitance of the ssDNA layer and the dsDNA layer and k_1 is the rst rate constant, related to the speed of the hybridization process. The time t_0 is the time at which the solution containing the DNA complementary-strand is added to the experimental pool.

In order to perform the tting in Figure 3.4 (green solid line) we further set $(C_{dsDNA} + C_0) = C_{ssDNA}$ where C_{ssDNA} is a t parameter that denes the dierential capacitance for $t < t_0$. The parameters obtained from our tting procedures are summarized in Table 3.2. Moreover, the overall DNA hybridization time derived from our measurements, $\tau = 1/k_1$ ' (13.1 ± 0.8) min, is in good agreement with both experimental and theoretical existing data for solid-phase hybridization reactions, at working conditions (i.e. ionic strength, DNA target concentration in solution, surface probe coverage) very similar to ours [75, 76]. Furthermore, tting data with 1st order Langmuir kinetics a reduced chi-square value of $\chi^2_\nu \approx 0.7$ is obtained. Although this model is the most accepted for the hybridization of ssDNA-SAMs, the Langmuir adsorption model fails in many cases, especially because it ignores probe/probe interactions. For instance, cross-linking interactions between adjacent adsorbed molecules will affect the target adsorption kinetics. This can aect the highest reachable-coverage.

To come to a more general model, which takes into account heterogeneities of the ssDNA SAM, we used the theory of Vincent Chan et al.[74] which applies and extends the Axelrod and Wang model of DNA hybridization. According to this theory, two dierent mechanisms describe DNA hybridization kinetics on immobilized probes on a solid surface: three-dimensional(3D) diusion of targets from free solution to the probe (direct hybridization) or through non-specic reversible adsorption from free solution to regions not covered with immobilized ssDNA followed by 2D diusion of the target to the probe (indirect hybridization). In this model of heterogeneous DNA-

[cDNA]	Fitting Parameters	1st order Langmuir Kinetics	Double Exponential Kinetics
10 pM	C_{dsDNA}	(0.918±0.001)nF	(0.915±0.001)nF
	k_1	(0.08±0.01) min^{-1}	
	τ	(13.1±0.8) min	
	τ_{hyb}		(8.4 ± 0.1) min
	τ_{melt}		(45.1 ± 3.9) min
	χ^2_v	0.7	0.9

Table 3.2: Fitting parameters for DNA/DNA hybridization C_d-proles shown in Figure 3.4 obtained using the 1st order Langmuir adsorption kinetics (cf. Equation 3.7) and Double Exponential model (cf. Equation 3.9), respectively.

DNA hybridization, several assumptions are made: the number of available probes is constant throughout the hybridization and covalently linked to an innite at surface placed at a certain distance from a DNA source of a given concentration. Here each of this DNA target reacts irreversibly with only one probe and that lateral interactions are neglected. These assumptions are fully satised in our experiments both in the WE functionalization protocols adopted (2.5) and in the geometrical features (circular geometry and since $A_{WE} \gg$ DNA target dimension). The latter condition appears valid if one computes the average distance from neighboring probe strands R_{probes}, that can be calculated directly from the surface probe density [74]:

$$R_{probes} = \sqrt{\frac{1}{4 \times \rho_{SAM}}} \approx 3.45 \pm 0.33 \text{ nm} \tag{3.8}$$

So, the DNA-hybridization process shown in Figure 3.4,can be best t considering a double exponential function, orange-dotted line:

$$C_d = C_{dsDNA} + C_0^{fast} \cdot \exp\left(-\frac{t}{\tau^{fast}}\right) + C_0^{slow} \cdot \exp\left(-\frac{t}{\tau^{slow}}\right) \tag{3.9}$$

where the superscripts indicate the two distinct kinetic modes considered. The reduced chi-square value obtained from the t is in this case is $\chi^2_v \approx 0.9$. From chemical kinetics, the solution hybridization rate ($k_{hyb} = 1/\tau^{fast}$) is expected to be proportional to DNA target concentration and the solution melting rate ($k_{melt} = 1/\tau^{slow}$) to be independent on concentration. The tting parameters have been summarized in Table 3.2.

The results indicate that acting on aspecic adsorption of single-stranded DNA on

the surface and subsequent two dimensional diusions, we can signicantly enhance the overall reaction rate and then it cannot be ignored. We believe in fact that heterogeneous hybridization depends strongly on the ratio of two-dimensional and three-dimensional diusion rates and the concentration dependence of the surface-based hybridization and melting rates.

Given all the above considerations, we applied to our system both models: 1st order Langmuir isotherm (3.7) and the double exponential kinetics 3.9. From tting the data in Figure 3.5, the parameters in Table A.3 can be obtained and it is shown in Appendix A. This analysis also demonstrated that the double exponential kinetics mode ts better our results for the hybridization process even though the data could be satisfactorily interpreted using the rst order rate Langmuir kinetics as well. Eventually we cannot exclude, for the conditions we used, to be in a situation where the degree of heterogeneity that exists on the biosensor surface not strongly aects the overall DNA hybridization process.

Further, the Langmuir adsorption model time constant, τ (red points) and the fast term in the double exponential model, τ_{fast} (blue points) are plotted as a function of cDNA concentration in solution in Figure 3.8. Such values are close to each other, and smaller than what reported in the literature for DNA-SAM hybridization from XPS and SPR measurements ([41, 48, 77]), in experimental conditions (e.g. DNA length, ionic strength) similar to ours.

Since in this work the important parameter is the hybridization time value and since Langmuir kinetics has been applied by many groups to study DNA hybridization on solid surfaces, in order to better compare our experimental results with literature, our data have been t with the Langmuir I order kinetics. At most, we can conclude that our experiments are performed in a Pseudo-Langmuir regime.

3.4 DNA Hybridization as a Function of the Applied Parameters

After having characterized the electrical behavior of our capacitive readout sensor and successfully detected DNA-hybridization, we moved forward and tested the eects of the applied bias potential on the hybridization process in dierent experimental conditions (i.e. buer solution, DNA probe density) to see how this potential can aect the

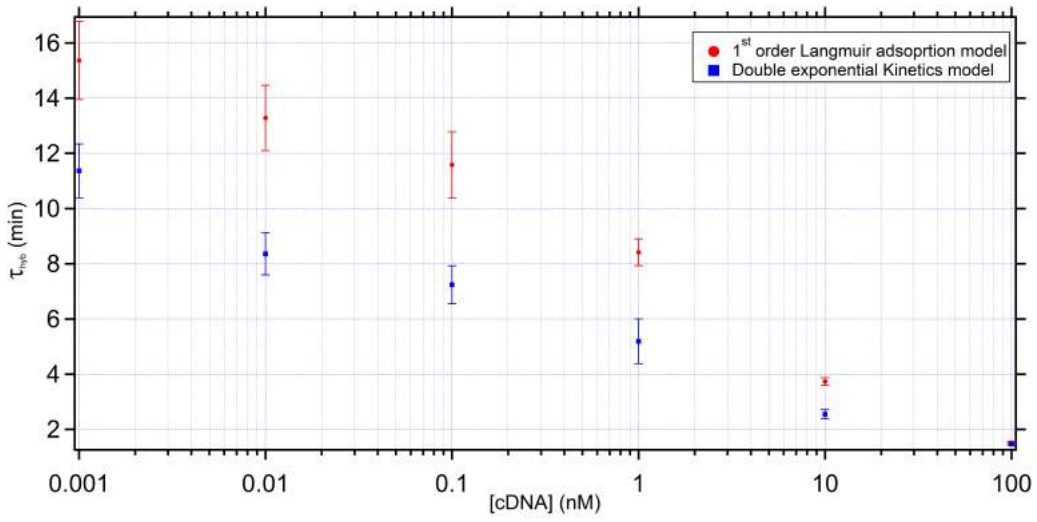

Figure 3.8: Plot of the hybridization time as function of [cDNA], dissolved in solution and in the range [1 pM; 100 nM], extrapolated using the 1st order Langmuir kinetics (red points) and the double-exponential model (blue points).

kinetics of target capture. It is well-known in fact, that hybridization depends on the ability of denatured DNA to reanneal with complementary strands in an environment just below their melting point [3], T_m. Moreover, the intermolecular interactions between DNA strands are primarily governed by hydrogen bonding and electrostatic repulsion, so various components in the hybridization solution have eects on the rate of renaturation.

First, we highlighted the eect of the applied bias potential on the DNA Hybridization mechanisms.

In the limit of low probe densities, an AC electric elds can be used to cyclically reorient the negatively charged DNA, providing an extremely sensitive scheme to promote target hybridization[78, 79, 80].

To test the validity of this hypothesis, we studied the hybridization kinetics as a function of the absolute value of the applied voltage. We tested the case of 8 pM complementary DNA in 100 mM KCL buer solution (on the same regenerated low density probe lm, incubation time τ_{inc} = 10 minutes), for two dierent values of V_{app}, 10 mV (red-blue lines in Figure 3.9) and 100 mV (black-green curves in Figure 3.9) respectively.

Dierences in ssDNA-SAMs are already discussed in previous section 3.1. Here,

[3] T_m is dened as the temperature at which half the DNA is present in a denatured form.

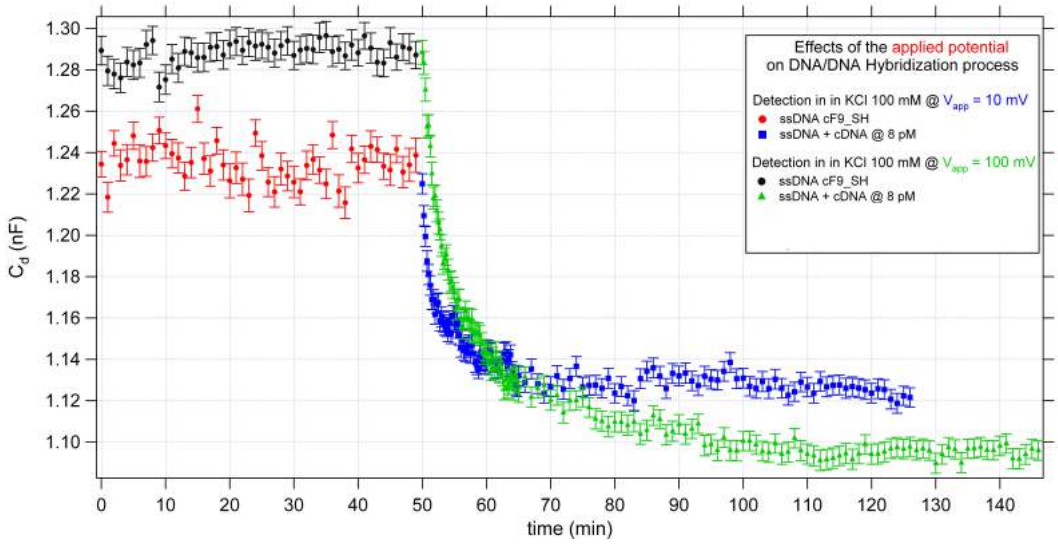

Figure 3.9: Eect of the applied potential on DNA/DNA Hybridization kinetics. The measurements are performed on the same probe lm at the same complementary DNA concentration (8pM) applying two dierent voltages: 10 mV (red blue lines) and 100 mV (black-green curves).

we can observe that increasing the applied potential, the hybridization process is faster (τ_{10mV} = 13.9 ± 0.8minutes $\Rightarrow \tau_{100mV}$ = 10.5 ± 0.2minutes) and more ecient as shown by the lower level reached by the measured$_d$C(η_{10mV} ~ 10% $\Rightarrow \eta_{100mV}$ ~ 15%); where the hybridization "eciency" parameter, η, is here estimated as the relative percentage dierence between the capacitance of ssDNA and the dsDNA at the equilibrium. From an electrostatic perspective,the surface density of immobilized charges,originated by probe phosphate groups, determines a kinetic activation barrier that a hybridizing target must overcome. This activation barrier is determined by the energy of inserting the DNA target into the DNA probe layer against the electrostatic potential of the charge density, thereby increasing the applied potential the charged cDNA's kinetic energy will raise, and then the probability to overcome the Coulomb's barrier.Considering our low probe density regime, ρ_{SAM} ' 2.1×10^{12} molecules/cm^2, and an ionic concentration of C_0 = 0.1 M, the maximum electrostatic potential in the layer is ~ 24.9 mV and thus the electrostatic driving energy to insert a positive counterions is ΔG_a ~ $3k_BT$ at room temperature (770 meV) [75, 76, 81]. Given the relative small magnitude of this electrostatic barrier, it becomes clear that the application of higher voltages can be compared with increasing ion concentration, leading to compensate for the electrostatic barrier from the DNA.

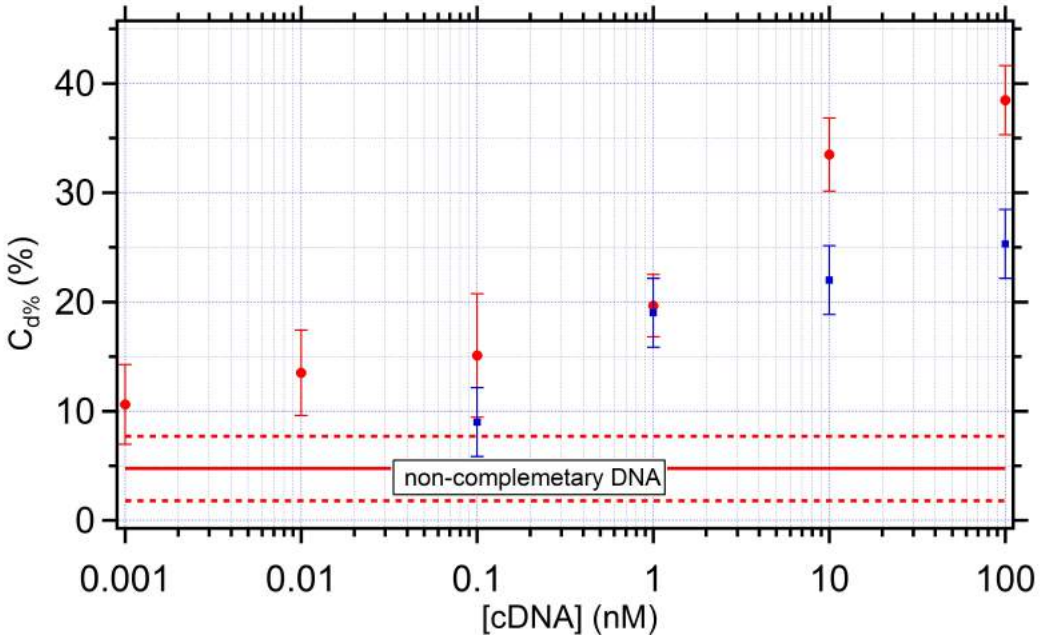

Figure 3.10: Calibration curve of the biosensor. The percentage capacitance variation (blue markers) at the WE as a function of the complementary DNA concentration in solution (KCl 100 mM) is here compared with results obtained in the same experimental condition (salt solution, ρ_{SAM} , same DNA sequence) but applying an AC potential with an amplitude of 10 mV (red points) during the hybridization process.The solid red line represents the average variation ofC_d when a non-complementary DNA is present in solution at high concentration (1µM), whereas the dashed red lines represent 3 standard deviations around this value.

In addition, the faster kinetics can be explained by the onset of an AC electroosmotic uid motion that acts on DNA strands accelerating them with respect to the simple diffusion. More on this topic can be found in chapter4 where we show direct measurements of DNA-hybridization kinetics.

Moreover, the importance of the applied potential can be further highlighted performing the hybridization processes shown in Figure 3.5 without applying any potential. Using as a buer solution KCl 100 mM, for each concentration we left the solution in contact with the WE for 1 h and then we measured the percentage change$C_d$frelative to the value at t = 0, corresponding to the electrode functionalized with ssDNA only. The obtained results, shown at page 62 of Ianeselli's PhD thesis [38], are compared (blue points) in Figure 3.10 with the $C_{d\%}$-values (red markers) estimated from data in Figure 3.5.

	LD (τ_{inc} = 12 min)		HD (τ_{inc} = 70 min)	
Fitting Param.	1st order Langmuir Kinetics			
	V_{app} = 50mV	V_{app} = 100mV	V_{app} = 50mV	V_{app} = 100mV
τ	(7.08±0.61) min	(6.21±0.33) min	(9.44±0.91) min	(8.52±0.65) min
χ^2_v	1.2	1.1	0.4	0.5
C_{ssDNA}	(1.09±0.01) nF	(1.24 ± 0.01) nF	(0.69 ± 0.01) nF	(0.74 ± 0.01) nF
η	(23.17 ± 0.22) %	(27.81 ± 0.21) %	(11.96 ± 0.19) %	(13.75 ± 0.05) %
	Double Exponential Model			
	V_{app} = 50mV	V_{app} = 100mV	V_{app} = 50mV	V_{app} = 100mV
τ_{hyb}	(6.14±0.59) min	(5.95±0.29) min	(8.02±0.87) min	(7.35±0.75) min
χ^2_v	0.9	0.83	0.78	0.81

Table 3.3: Eect of the SAM probe density on DNA/DNA hybridization process of a Low Density and High Density ssDNA, respectively, in a 100 mM KCl buer solution and at two dierent applied potentials: 50mV and 100mV. The hybridization process is more ecient in the case of low densities and faster at high potential. Hybridization times are obtained from the rate constant in eq.3.7.

From Figure 3.10 we note that, applying an AC potential, we are able to detect DNA-hybridization on a wider dynamic range of complementary DNA concentrations and with a more eciency kinetics, the latter is of fundamental importance for the detection of more complex biomarkers circulating in the bloodstreaming.

Explained the eect of the applied potential on the hybridization mechanisms, we chose, as a proof of principle, to investigate the capacitance response of the device as a function of two dierent electrode functionalization (High Density (HD) and Low Density (LD)) in KCl 100 mM and MgCl2 33 mM (i.e. same ionic strength but dierent ionic charge so a diering screening behavior), at two dierent applied potentials (50 mV, 100 mV).

By adopting the same procedure described in section2.5 and using a concentration of 1 nM for the complementary DNA in solution, the experiments of the DNA-hybridization were repeated, functionalizing two samples with two dierent ssDNA-SAM densities, 12 (LD) and 70 (HD) minutes respectively. Figure 3.11 shows the results for the hybridization process. The yellow-green curve is the hybridization of ssDNA incubated for 12 minutes and the red-blue is the HD ssDNA. The tting parameters are summarized in Table 3.3.

Comparing the four hybridization processes in Figure 3.11 and considering the t-ting parameters shown in Table 3.3, appears more evident as highlighted in the previous

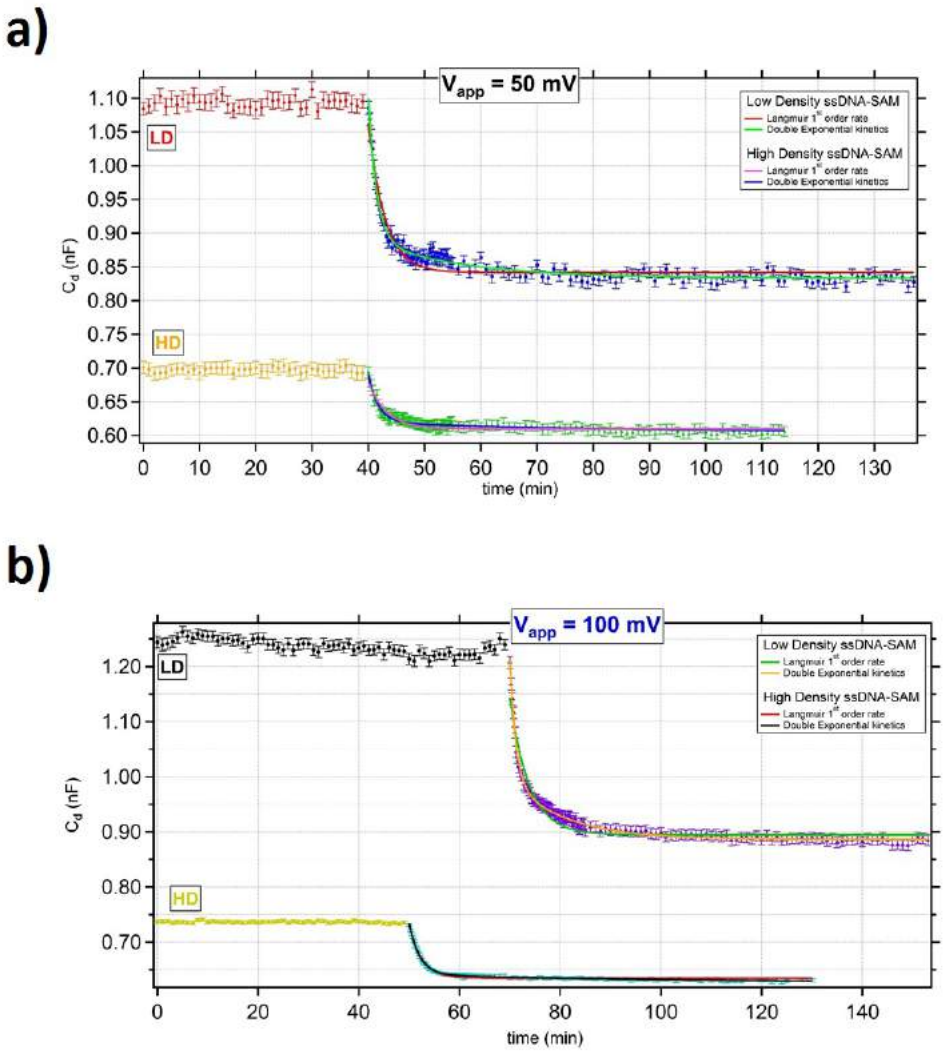

Figure 3.11: Eect of the SAM-probe density on DNA/DNA hybridization process. The experiments were performed in a 100 mM KClbuer solution and with a [cDNA] = 1 nM. Hybridization of a Low Density (LD, τ_{inc} = 12 minutes) ssDNA and a High Density (HD, τ_{inc} = 70 minutes) ssDNA with an applied potential of a) 50mV and b) 100mV. The hybridization process is more ecient in the case of low densities and it has a faster kinetics increasing the applied potential, see 3.3 for further details on the kinetics studies.

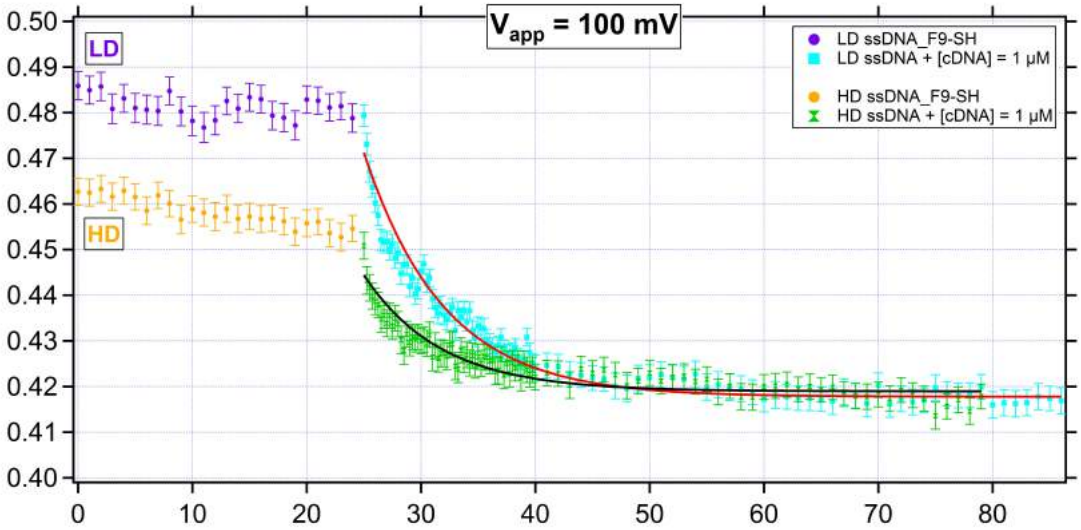

Figure 3.12: Hybridization of a Low Density (τ_{inc} = 12 min) ssDNA-SAM and a High Density (τ_{inc} = 70 min) ssDNA probe layer with an applied potential of 100mV in a buer solution of $MgCl_2$ 33mM. The kinetics studies are performed using the well-known 1st-order Langmuir adsorption model.

sections testing the soundness of our biosensor and reproducibility achieved in its fabrication. Raising the applied potential we can observe an increasing in the measured capacitance at the ssDNA-functionalized WE and an increase of hybridization kinetics. In addition, a rise in the incubation time and thus in the SAM probe density, is connected to a decrease of C_{ssDNA} and to an increase of steric crowding eects to target insertion which would require a large number of base pairing to nucleate the double strands leading to a minimal hybridization, as was expected.Moreover, observing the reduced chi-square values in Table 3.3, it is not surprising that the hybridization kinetics are poorly t by a single exponential in fact, in this regime, the kinetics are often described taking into account wider distributions of τ that fall between the fast and slow limits of $\tau_{hyb} \sim (k_{on}[cDNA]^{-1})$ and $\tau_{melt} \sim k_{off}^{-1}$.

The same experiments described before have been performed in 33 mM $MgCl_2$ buer solution. In this specic case, it is impossible to evaluate both the LD and HD SAM-hybridization applying a potential of 50 mV; it is not the case if we apply a potential of 100 mV but with a [cDNA] of at least 10 nM and thus a capacitance change unambiguously assigned to the DNA hybridization process can be appreciated.

The same trends of the experiment carried out in 100mM KCl are found and shown

in Figure 3.12. As already explained and observed, increasing the SAM probe density we foud out a decrease in the measured C_d ($C_{ssDNA,LD} = 0.48 \pm 0.01 nF \Rightarrow C_{ssDNA,HD} = 0.45 \pm 0.02$) as well as a less ecient process ($\eta_{LD} \sim 13.2\% \Rightarrow \eta_{HD} \sim 8.6\%$). From kinetic point of view, referring to eq. 3.7, we estimated the following two hybridization times: $\tau_{LD} = 13.9 \pm 0.8$ minutes, $\tau_{HD} = 10.5 \pm 0.2$ minutes, for LD- and HD-SAM respectively. We note here that the time needed for hybridization are comparable and the C_{dsDNA} - values reached are almost the same in both cases and it is due to the Mg^{2+} ions. In fact, in the limit of low surface potentials (few hundreds millivolts) and under physiological salt conditions (~ 0.16 M NaCl), the excess ion concentration at the electrode surface, n_0, can be found directly from the surface potential (Ψ_0) and the Debye screening length (λ_D):

$$n_0 = n_{bulk} + \frac{\varepsilon_0 \Psi_0^2}{2 k_B T \lambda_D^2} = n_{bulk} + \frac{1}{2}\left(\frac{e\Psi_0}{k_B T}\right)^2 \sum_i z_i^2 n_i \qquad (3.10)$$

where z_i and n_i are the valence and bulk concentration of the ith electrolyte species in solution, so magnesium ions admit a larger potential to accumulate near the electrode surface due to their $z = 2$ valence.

Such high electrostatic charge forces the DNA strands to approach the surface as closely as possible, in this case forming two close-packed layers, after which like charge repulsion starts to dominate, moreover the need to screen these highly charged layer also creates an increased in the concentration of counterions near the electrode rising the kinetic activation barrier and thus preventing ssDNA to feel the presence of complementary strands.

3.5 Mismatch detection in DNA monolayer

DNA hybridization is at the basis of most current technologies for genotyping and sequencing, due to the unique properties of DNA base-pairing that guarantee a high grade of specicity. At the same time, diversity and evolution of life is closely related to DNA sequence alterations. In medical diagnostics and human identication, precise nucleic acid hybridization and sequence discrimination between single nucleotides (or a single nucleotide polymorphism (SNP)) is of great importance and signicance. In this framework, the major challenge is, nowadays, to develop a device that is able to distinguish a mismatch of a single base and to simultaneously provide a sensitive signaling mecha-

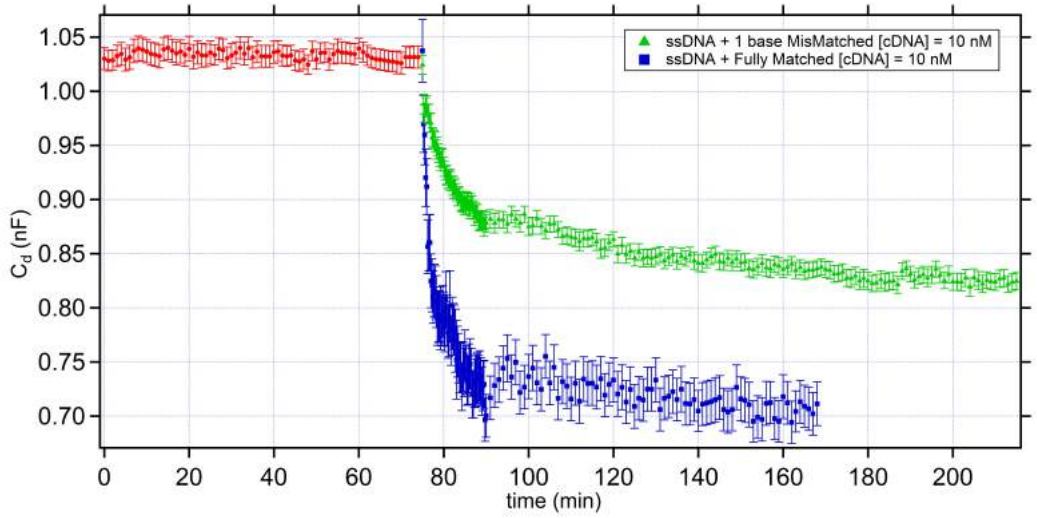

Figure 3.13: The capacitance,extracted from the impedance measured in our Electrochemical setup, is plotted versus time for the ssDNA-functionalized electrode (red curve) and for the mismatched (green) and perfect matching (blue) complementary sequences. The buer used for this experiment was a solution of KCl 100 mM in which we dissolved 1o nM complementary DNA and single-base mismatched sequence. Hybridization times are obtained from the rate constant in eq.3.7.

nism to translate the dierent hybridization events (perfect match vs mismatch) into a dierentiable readout [82, 83, 84].

Here the device applicability is demonstrated through the selective detection for sequence-specic DNA.

Nine oligonucleotide sequences were synthesized by Biomers.net GmbH (Ulm, Germany), and they were used as received. For this kind of experiments measurements are splitted in two dierent sets according to the two distinct probes.

Probe DNA (pDNA1), HS-$(CH_2)_6$-5'-tga taa tca tta taa aac tga aat a-3' was used as 25mer- DNA probe for the rst set of experiments; complementary target DNA (cDNA1), 5'-tat ttc agt ttt Ata atg att atc a-3' was used as the complementary DNA strand; one-base-mismatched DNA (1MM_DNA1), 5'-tat ttc agt ttt Gta atg att atc a-3', this oligonucleotide was identicalto the complementary DNA with a substitution (G/A) at position 13 shown with capital bold letters, leading to a single base mismatch with the probe.

By adopting the same protocol described in section 2.5,we functionalized the WE with the pDNA_1 probe and we measured C_d at the ssDNA-SAM functionalized WE (red

circles in Figure 3.13) in a 100 mM KCl buer solution. Veried that the signal was stable over about an hour of continuous measurements, then we changed the solution in the experimental pool adding a known concentration (10 nM) of perfectly matching sequence cDNA1. As demonstrated, after addition of the complementary DNA (blue squares) in the electrochemicalcell, we can observe a decrease of the capacitance with a variation of about 30% less than the initial value, as a sign of the occurred hybridization. When we insert, at the same concentration, on the regenerated electrode (see 2.5.1 for more details) the mismatched sequence 1MM_DNA1 (green triangles) we observe a slower decay of the capacitance tending to a plateau much closer to the initial C_{ssDNA} value than the perfectly matched one (19% variation), conrming a less ecient hybridization and a slower dierent kinetic behavior (τ_{1MM} ' 16.2 ± 0.6 min $\Rightarrow \tau_{PM}$ ' 3.8 ± 0.3 min).

We further challenged our device exposing a 44 bases ssDNA ($(CH_2)_6$-5'-caa aac agc agc aat cca aag atc aga cac ccg att aca aat gc-3', pDNA2) probe to ve dierent sequences its complementary target (cDNA2) had the sequence 5'-gca ttt gta atc ggg tgt ctg atc ttt gga ttg ctg ctg ttt tg-3'; two-bases-mismatched DNA (2MM_DNA2), 5'-gca ttt gta atc ggg tgt cGg atc Ctt gga ttg ctg ctg ttt tg-3'; and three-bases-mismatched DNA (3MM_DNA2), 5'-Tca ttt gta atc ggg tgt cGg atc Ctt gga ttg ctg ctg ttt tg-3', these sequences were identical to the second fully matched DNA with the exception of two and three bases, highlighted with capital bold letters, respectively; additionally, the hybridization between the probe pDNA_2 and two half (22mer) strands, which are complementary to upper half (5'-gca ttt gta atc ggg tgt ctg a-3', cDNA2_UP) and lower half (5'-tct ttg gat tgc tgc tgt ttt g-3', cDNA2_DOWN) of this probe, was investigated and results were compared with fully matched strands (cDNA2) and thanks to these measurements, we demonstrated that hybridization of ssDNA is sensitive to the position (upper or lower) of half-sequence target strands on the ssDNA probe molecules.

In Figure 3.14a) we report the study of the kinetics of DNA hybridization in presence of 2MM (green triangles) and 3MM (black markers) mismatches compared with the fully matched (blue squares) sequence on the same regenerated probe lm (pDNA2). We can clearly distinguish the behavior of the three dierently matching sequences. As expected we measured a slower kinetics and a lower plateau value going from the PM (36% variation and τ_{PM} ' 5.7 ± 0.2 min) to 2MM (17% variation and τ_{2MM} ' 9.9 ± 0.2 min) and nally to 3MM (10% variation and τ_{3MM} ' 13.1 ± 0.8 min).

Analogously, in Figure 3.14b) we have studied half matching target strands (22-mer),

which are complementary to the lower and upper part of ssDNA and the results have been compared with full length target (44-mer). Again, we can appreciate,in the presence of 20 nM target concentration, a typical hybridization kinetics that is less ecient for the UP (η_{UP} ' 25 %) and DOWN (η_{DOWN} ' 14 %) half sequences with respect to the PM (η_{PM} ' 34 %). Noteworthy, the kinetics of hybridization for the perfect match (τ_{PM} ' 4.1 ± 0.2 min) and 22 UP (τ_{UP} ' 5.1 ± 0.3 min) targets are similarly fast. In contrast, the 22 DOWN target, which must hybridize closer to the surface, shows dramatically slower kinetics, requiring over 30 minutes (τ_{DOWN} ' 30.6±3.6 min) to reach its steady-state hybridization. Presumably, the target must penetrate further into the DNA lm before nucleation and zipping can occur since the rst distal probe nucleotides are non-complementary to this target. In conclusion, the results of experiments show that dierent kinetics signals reected a dierent degree of mismatch between probe DNA and complementary target DNA, and mismatched variants of target DNA. Additionally, we are able to clearly distinguish the presence of single, or multiple mismatches and also the position with respect to the gold surface of the missing basepairs[85]. It can be easy explained considering the activation energy of the association step in the double helix formation. As shown by many pioneering studies ([86, 87]) and already stated this barrier has a negative value which means that the association of two complementary single strands is not an elementary reaction resulting from biomolecular collision but can be interpreted by the nucleation-zipping model. Briey, this model describes double helix formation as a process that starts in a series of fast but unfavorable reactions with a few base-pairing (forward) and un-pairing (backward) processes, then when a further base pair is added to the critical intermediate, a helix nucleus is formed.These observations clearly pointed out that the zipping process and of course the measured signal will be a function not only of the length of the sequence but also of the position as well as the number of mismatches along the sequence.

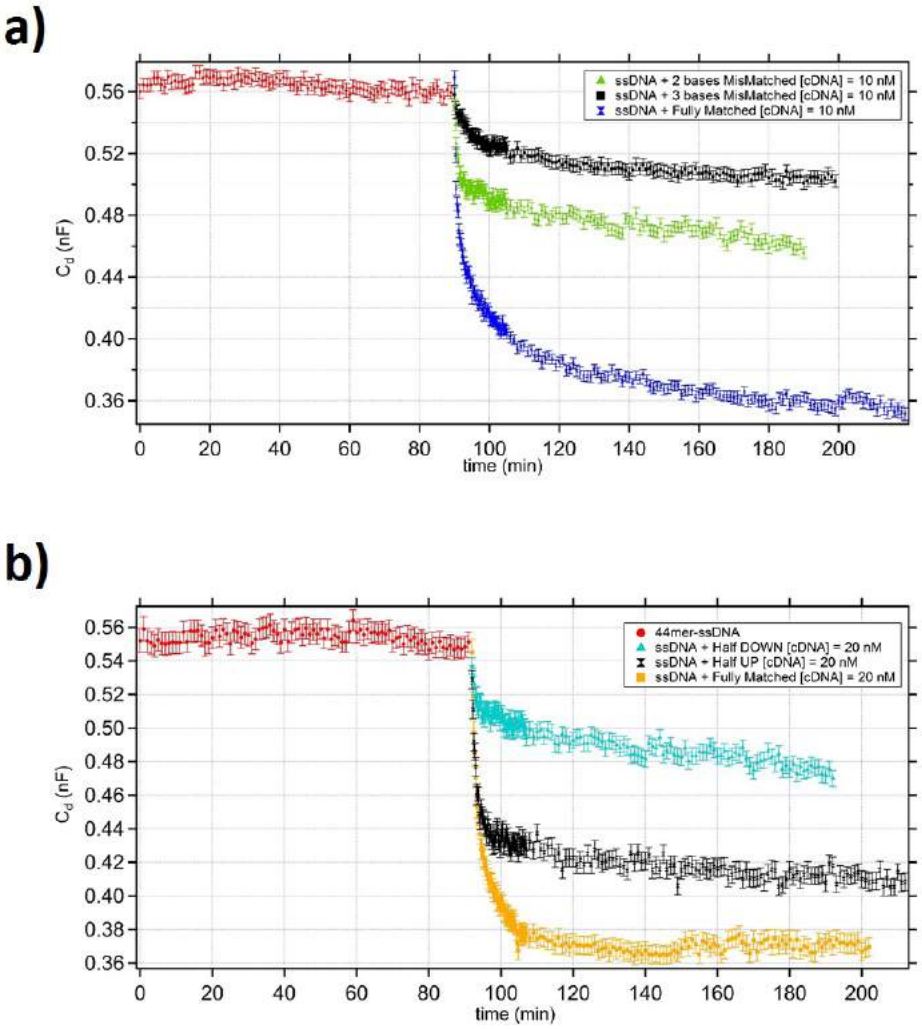

Figure 3.14: Kinetics of DNA-hybridization, in KCl 100mM, via dierential capacitance measurements in presence of multiple mismatches (a) and in presence of partially complementary sequences (b).The red signals are the C_d measured at the LD 44mer ssDNA-SAM functionalized WE. (a) In blue we report the hybridization with the fully matching sequence, in green the hybridization with a sequence with 2 MMs, and in black the hybridization with a sequence with 3 MM. (b) In orange we report the hybridization with the fully matching sequence, in black the hybridization with a 22mer sequence complementary with the upper part (far from the gold surface) of the target and in cian the hybridization with a 22mer sequence complementary with the lower part (close to the gold surface) of the target.

Chapter 4

DNA Surface Hybridization via Theoretical Model

Mathematical modeling of DNA biosensors can be a daunting task, since the system under consideration is dynamic and complex. Additionally, there are many levels of abstraction in the mathematical description of the system, which lead to dierent paradigms in designing the simulation software. Capturing of all the physics of the DNA molecules and coupling them to the physics of our biosensor, requires a huge computational eort that makes it inaccessible to today's most resourceful computers. For this reason, I had resorted to several simplications to the geometry, equations, and boundaries to obtain simpler solutions that, nevertheless, capture the essential physics that is intended to be studied.

In this chapter, we will try to provide an explanation of the results obtained by using an appropriate mathematical model of the hybridization process occurring at the electrode/electrolyte interface and of high strength AC electric elds, generated by our planar microelectrodes, resulting not only in forces on the DNA molecules but also on the suspending buer solution in the experimental pool. Several researching groups have examined DNA surface hybridization theoretically using a variety of approaches. Chan et al. [74] and Erickson et al. [88] considered the case in which DNA probes are immobilized at low density, permitting surface adsorption and lateral diusion of DNA targets. Hagan and Chakraborty [89] explored the eect of steric crowding on initial hybridization rate constants using polymer brush models. Wong and Melosh [76] modeled experimental results at high DNA densities taking into account the changing electrostatics within the layer, which rapidly become nonlinear as hybridization proceeds

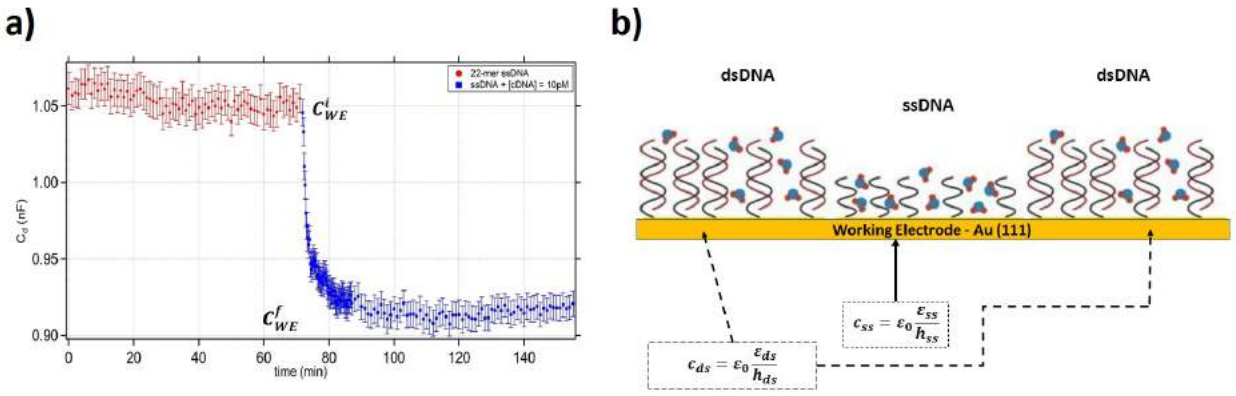

Figure 4.1: a) Hybridization of a LD ssDNA with an applied potential of 10mV in a buer solution of 100mM KCl performed by adding 10 pM complementary DNA. b) Idealization of the electrode/electrolyte interface after a not complete hybridization process.

and the eects of applied potential on the biomolecular activation [80, 81].

Here, we employed a model capacitance-readout DNA detector to demonstrate that the detection limit and specicity of our surface-based genosensor is not dependent on the true anity of the probe for its target but is simply dependent on the eective density with which the probes are packed on the surface area and on the interfacial electric eld.

4.1 The Capacitive Model

As already stated, in this work we have focused our attention on the measurement of the dierential capacitance, C_d, at the electrode/electrolyte interface. In our conguration of a bio-functionalized metal electrode immersed in a saline solution C_d can be modeled as a planar capacitor (cf. Eq. 2.2) whose variations arise upon molecular adsorption on the electrode surface and include height changes, substitution of water molecules in the biological layer, and changes in the electrical charge density. For these reasons, the total capacitance can be described as the sum of capacitances linked in parallel and associated to the area composed of DNA strands (hybridized or not) and ions (Figure 2.4).

Starting from these assumptions, the maximum percentage variation of C_d upon hybridization, $C_{d\%}$, for a given value of [cDNA], can be expressed as a function of the nal (after complete hybridization, C^f_{WE}) and initial (before hybridization, C^i_{WE}) capacitance measured at the functionalized Working Electrode (WE):

$$C_{d\%} = \frac{C^{f}_{WE} - C^{i}_{WE}}{C^{i}_{WE}} \times 100 \tag{4.1}$$

with

$$C^{i}_{WE} = A \times c_{ss} = A \times \frac{ss \cdot 0}{h_{ss}} \tag{4.2}$$

$$C^{f}_{WE} = A \times c_{ss} \quad 1 + N^{f}_{ds} (\xi_C - 1) \tag{4.3}$$

where:

- c_{ss} is the density of capacitance measured at the ssDNA-SAM WE;
- A is the electrode area;
- $\xi_C = c_{ds}/c_{ss} = \frac{h_{ss}}{h_{ds}} \frac{ds}{ss}$ is a helpful tting parameter;
- h_{ss}, $_{ss}$ and $_{ds}$,h_{ds} are the thickness and the dielectric constant of the molecular layer before and after the hybridization process, respectively;
- N^{f}_{ds} is the fraction of total strands that is in duplex form at the equilibrium. Obviously, it is function of [cDNA] and can be estimated by Sips model 3.3:

$$N^{f}_{ds} = \Gamma_{max} \frac{(K_A \cdot [cDNA])^{a}}{1 + (K_A \cdot [cDNA])^{a}} \tag{4.4}$$

where the parameter$a$ can be set equalto 1 since, in our experimental conditions, binding can be well described using a simplied hyperbolic Langmuir isotherm.Γ_{max} is the maximum surface coverage (molecules/cm^2) of hybridized sites for a given value of [cDNA], it is also worth noting that value of$\Gamma_{max} = 0$ implies an absence of hybridization, whereas the opposite$\Gamma_{max} = 1$ means that complete hybridization has occurred. As already stated, the amount of hybridized analyte, detectable on the gold surface,can be described by the dierential equation resulting from the Langmuir adsorption model that can be solved analytically in our experimental conditions:

$$\frac{d\Gamma(t)}{dt} = k_{on}[cDNA] (\Gamma_{max} - \Gamma(t)) - k_{off} \cdot \Gamma(t) \tag{4.5}$$

here,$\Gamma(t)$ is the bound target coverage, for a set of complementary strands concentrations, [cDNA], at a xed temperature on the same probe lm. In the ideal Langmuir

model where all probe sites are energetically equivalent, independent and available for binding, the measured saturation level for target binding should be equal to the coverage of immobilized probe molecules, Γ_{max}.

Rearranging the equation 4.1 in terms of equations 4.2, 4.3 and 4.4, we found out the equation that models the charge density change at the interface:

$$C_{d\%} = N_{max} \frac{K_A \cdot [cDN\,A]}{1 + K_A \cdot [cDN\,A]} (1 - \xi_C) [1 - \exp(-(k_{on}[cDNA] + k_{off})\, t)] \times 100 \quad (4.6)$$

where $K_A = K_D^{-1} = k_{on}/k_{off}$ is the anity constant for DNA hybridization and k_{on}, k_{off} are the adsorption and desorption rate constants, respectively.

Referring to the Table 3.1, we can set, with a good approximation, C_{WE}^{i} ' 1.06±0.01 nF, which implies a dielectric constant for the ssDNA-monolayer, $_{ss}$ ' 36 , consisting with the values found in litetarute. From Bosco et al.[90], obtained for a low density DNA SAM similar to ours, we can x h_{ss}/h_{ds} ' 0.54 . In addition, as found in literature, N_{max} can be arbitrarily set equal to the highest measured target coverage. In our operating conditions (ρ_{SAM} ' 2×10^{12} molecules/cm^2), as stated by Peterson et al. [48], we can set $N_{max} = 1$, which means that DNA-hybridization eciency can reach 100%.

Under these assumptions, a parameter ξ_C ' 0.42±0.07 and an anity constant K_A ' (0.53 ± 0.08) × 10^9 M^{-1}, were derived, which corresponds to a $K_{D,model}$ ≈ (1.88 ± 0.27) nM lower than that experimentally measured, K_D ≈ 2.8 ± 0.7 nM.

By overlapping the percentage change of dierential capacitances upon hybridization experimentally got (red circles) and the $C_{d\%}$-values extracted from the ts (Eq. 4.6) we can note a model that partially match our data which suggests the need to consider elements related to the applied potential and the non-negligible diusion. The results are shown in Figure 4.2:

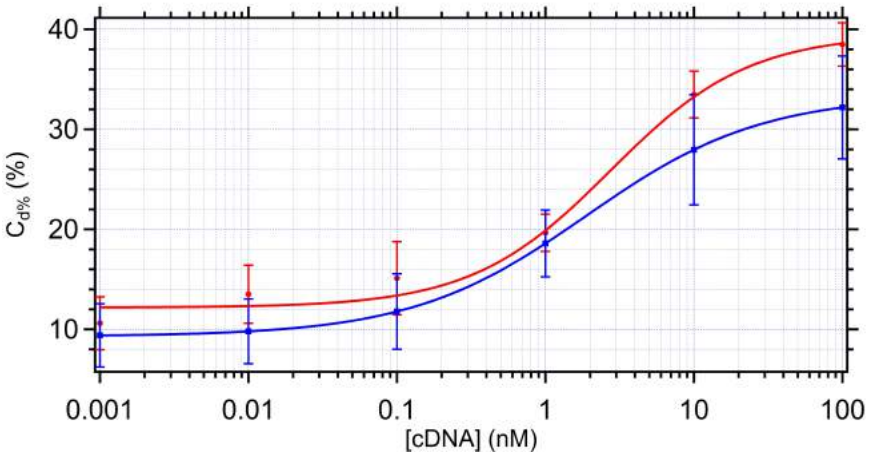

Figure 4.2: $C_{d\%}$ expressed as a function ofthe concentration of complementary DNA dissolved in 100 mM KCl buer solution gotten from the model (blue squares) described by Eq. 4.6 and overlapped to the experimental values (red circles) performed in the same operating conditions.

In this pseudo-Langmuir (PL) regime, the experimentally observed hybridization fractions are constant and exploring the eect of steric crowding on initial hybridization rate constants we did not consider changes in these values as hybridization proceeded and the physical properties of the polymer brush varied.To accurately model experimental results, a model is needed that can account for the applied voltages used to compensate this changing electrostatic kinetic barrier within the layer, which rapidly become nonlinear as hybridization proceeds allowing kinetic suppression of hybridization reducing the hybridization eciency.

Before doing it, under conditions more typical of applications, additional interactions become signicant. In fact, the average distance between probe sites in the experiments was at most 3.8 nm (from equation 3.8 since ρ_{SAM} ' 2.1×10^{12} cm^{-2}), and was thus always comfortably spanned by 22mer probes with a contour length of 7.5 nm. At these coverages and ion concentrations,it appears impossible for the probes to not interact leading to a kinetic suppression of hybridizationWe cannot continue to rely on Pseudo-Langmuir modeland suppressed anity for targets and the lowered sensitivity of probe-target hybridization is consistent with presence of probe-probe associations.

Wong and Melosh [76] quantied hybridized target number density as a function of probe density and ion concentration showing that, in this suppressed hybridization (SH) regime, the electrostatic potential outside the DNA probe layer that, as we antici-

pated, repels incoming DNA targets increased reducing the maximum number of targets to hybridize (see the paper for more details). At experimental conditions (i.e. ionic strength, DNA target concentration in solution) very similar to ours, they found that the eciency of hybridization is ' 49% which means that N_{max} ' 0.5 in Equation 4.6 which further increase the gap between experimental and theoretical values observed in Figure 4.2. In addition, it should be noted that the characteristic timescale needed to hybridize 1 µM of [cDNA] is $\tau \sim 650$ s ~ 10 minutes, consistent with measurements by the Georgiadis group[48].This long hybridization time is mainly due to the stochastic Brownian motion by which cDNA strands move towards the surface-immobilized probe ssDNA. Although this timescale is not experimentally prohibitive, the lower the [cDNA] is, the smaller the directional diusive ux becomes, which adversely aect the detection of lower cDNA concentrations due to the considerably long timescales of hybridization and the low binding density.

4.2 The Electrokinetics component of the Model

As already stated, the applied voltages play a key role in improving the long hybridization time. We have reported previously that, the application of an interfacial electric eld alters the ionic double layer at the metal/electrolyte interface and therefore compensates the electrostatic barrier modifying the surface electron distribution.

In this section, we examine the eect of electrokinetiks on target/probe hybridization since such phenomena, including dielectrophoresis (DEP), electrothermal eect (ETE) and AC electroosmosis (ACEO), can be used both to drive uid ow and manipulate particles and molecules smaller than 1µm in diameter without the use of external pumps or valves ([91, 92, 93]).

DEP arises from a dierence in electrical permittivity between a particle and the surrounding medium. If DEP > 0, the particle is more polarizable than the medium and the DEP force is directed towards regions of high electrical eld strength.In contrast, if the particle is less polarizable than the buer solution (DEP < 0) the force is directed down the electric eld. In fact, the monolayer DNA thiol lm used in this work, tethered directly to the gold working electrode surface through a goldthiol covalent attachment, are exposed to a eld gradient at the metal/electrolyte interface on the order of 10^9 V/m. Positive DEP is employed by Cheng et al.[94] to rapidly trap, via microuidic platform, 26-base-long ssDNA on a chip with a locally tuned AC electric eld gradient

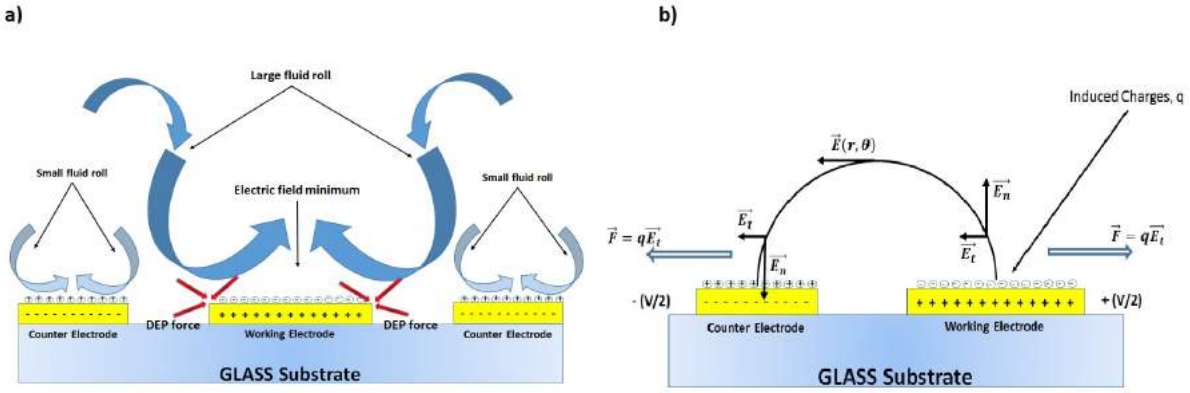

Figure 4.3: Side-view schematic of rotating vortices induced by AC-ElectroOsmosis (ACEO) above the electrodes. The uid motion caused by ACEO is shown as blue arrows as well as Red arrows indicate the force due to DEP.

for hybridization analysis. The DEP trapping method has also been used in order to select and separate dierent types of bacteria[95].

ACEO refers to the uid motion (Figure 4.3a)) originating from the interaction of the electrolyte ions in the double layer with the electric eld over the electrodes (Cartoon in Figure 4.3b)). In other words, this double layer interacts with the transverse component of the electric eld to produce a uid motion across the electrode surface, thus helping to overcome the slow diusional transport that would otherwise will be dominant. Noteworthy, since the sign of the electric eld and the charge density change in phase with each other, the uid motion will always be in the same direction. Hart et al. used AC-electroosmosis to enhance the transport of analyte to an interdigitated planar electrodes observing that binding times was reduced by up to a factor of 6.

ETE arises from the movement of induced charges due to the joule heating within the bulk of the solution and it is present only if the Gauss law and the charge conservation equation are to be satised simultaneously. In general, ETE dominates in higher conductivity solutions (typically > 1 mS/cm) and it takes place at electrical frequencies higher of a critical crossover frequency[96]:

$$f_{crossover} = \frac{\sigma_f}{2\pi\,} \sqrt{1 - \frac{2\beta}{\alpha}} \approx \frac{\sqrt{11}\sigma_f}{2\pi\,} \approx 3.8 \text{ MHz} \qquad (4.7)$$

where $\sigma_f \approx 5$ mS/m ([97]) and $\approx 76,7 \cdot$ $_0$([72]) are the conductivity and permittivity of our experimental 100 mM KCl buer solution. From Eq. 4.7, the electrothermal

induced ow can be considered clearly negligible.

Therefore, cDNA strands in our biosensor move under the inuence of the uid and the dielectrophoretic force exerted on them by the AC electric eld. In particular, we will prove that in our experimental conditions (low frequencies and low potentials), the electroosmotic forces are dominant [98] and that DEP force pushes the complementary strands towards the region where the electric eld is minimum, Fig. 4.3a).

The molecular electrostatics and chemistry of the DNA molecule are very important in dictating the interaction of the DNA with its surroundings. Obviously, the rst step is the computational description of the DNA molecules.

4.2.1 The DNA Molecule

The DNA molecule in itself is by far the hardest part to model. This is due to the complex nature of its geometry, in addition to the molecule's exibility and its versatile chemistry.

As it is very well known, the DNA molecule is a polyelectrolyte comprised of two helically-wound sugar-phosphate backbones, joined in the middle by nucleobases and the two strands are bonded by means of hydrogen bonds between matching nucleobases (AT and CG). The phosphate groups are negatively charged in biologically relevant conditions (25°C, monovalent salt concentration in the range 1mM-1M, pH 7) that are either directly or indirectly responsible for the signal change in a genosensor due to DNA capture.

In our experiments, the DNA molecules used as probes are oligonucleotides (22-44 bases long) which allow faster and more specic hybridization rate and their descriptions can be very dierent from the models used to describe longer chains. Two problems are associated with the description of the DNA molecule: the conformation and motion dynamics, and the electrostatics/chemistry. The motion of longer DNA molecules is generally handled by simplied continuous models, such as the worm-like chain (WLC) model ([99]) or the free-jointed chain model (FJC) ([100]) . Shorter DNA strands are stier and cannot be modeled by such continuous models, but are rather treated using complete molecular dynamics studies ([101]). Unfortunately, for such studies, simulations on the most powerful computers are limited to a few nanoseconds, limiting the observation of longer timescale eects.

The charge distribution of a DNA molecule is obtained by solving the N-body Schrödinger

equation over all nuclei and electrons of the molecule whose time-independent eigenvalues give the N-body wave function which describes the shape of the molecule:

$$-\} \sum_i (2m_i)^{-1} \nabla^2_{\vec{r}_i} + \sum_j V(\vec{r}_i, \vec{r}_j) \Psi(\vec{r}_1, \vec{r}_2, ...) = i\} \frac{\partial}{\partial t} \Psi(\vec{r}_1, \vec{r}_2, ...) \quad (4.8)$$

In Equation 4.8, $\vec{r}_n$ is the position vector for the n-th body, Ψ is the wavefunction amplitude, m_i is the eective mass of the i-th object, V is the potential energy between two objects. Many approximations are used to make the solution easier to solve.The Born-Oppenheimer approximation allows decoupling of nuclei and treating them as classical particles. Therefore, hereinafter, the DNA molecule will be treated as a homogeneous spherical particle of radius equal to its persistence length, permittivity $_{sDNA}$ ' 8 and conductivity σ_{sDNA} ' 1.08 mS/cm.

The problem then reduces to nding the energy and shape of the electronic cloud as a function of the nucleic coordinates.Even with all of these approximations, the N-body electronic wave function has to be decoupled, replacing the dependency of the electronic mutual potential energies by a system (the "KohnSham system") of non-interacting electrons that generate the same density as any given system of interacting particles, is thus dened by a local eective external potential in which the non-interacting particles move, $v_{eff}(\vec{r})$ ([102, 103, 104]).In our case, the particles of interest are non-interacting fermions, so the KohnSham wavefunction is a single Slater determinant constructed from a set of orbitals that are the lowest energy solutions to:

$$-\frac{\}^2}{2m}\nabla^2 + v_{eff}(\vec{r}) \quad \varphi_i(\vec{r}) = \ _i\varphi_i(\vec{r}) \quad (4.9)$$

This eigenvalue equation is the formalism that was used to modelthe electric eld generated by the electron cloud connected to the cDNA strands in solution.Here, $_i$ is the orbital energy of the corresponding KohnSham orbital, φ_i, and the density for an N-particle system is:

$$\rho(\vec{r}) = \sum_i^N |\varphi_i(\vec{r})|^2 \quad (4.10)$$

This, of course, is an approximation but such simplications allow the simulations to run for signicantly longer times, which enable the capture of long-time phenomena such

as DNA hybridization. The key here is to nd the proper problem simplication without sacricing the loss of valuable chemical and electrical information about the molecule.

4.2.2 DEP force calculation

As already stated, at driving frequencies lower than $f_{crossover} \approx 4$ MHz (Equation 4.7), Coulomb force acting on the induced charge at the interface of two materials (i.e. DNA strand and 100 mM KCl-doped aqueous solution) of dierent electric properties will transport the medium of more polarizability to regions of largest eld intensity and vice versa. Given knowledge of the electrical eld gradient, for a spherical particle of radius a immersed in a liquid suspension of dielectric constant ε_m, the time-averaged DEP can be described using the point dipole model,[105]:

$$\left\langle \vec{F}_{DEP} \right\rangle = 2\pi a^3 \varepsilon_m \cdot \mathrm{Re}\{K(\omega)\} \nabla |E_0|^2 \tag{4.11}$$

where the real part of the Clausius=Mossotti factor ($\mathrm{Re}\{K(\omega)\}$) takes into consideration the frequency dependence of the DEP force. For a particle of spherical shape, it is dened as:

$$K(\omega) = \frac{\tilde{\varepsilon}_p - 2\tilde{\varepsilon}_m}{\tilde{\varepsilon}_p + 2\tilde{\varepsilon}_m} \tag{4.12}$$

here, subscripts p and m represent the particle and uid, respectively, and $\tilde{\varepsilon} := \varepsilon - i\sigma/\omega$ is the complex permittivity. Thus, the real part of CM factor is:

$$\mathrm{Re}\{K(\omega)\} = \frac{\varepsilon_p^2 - 4\varepsilon_m^2 + \frac{\sigma_p^2}{\omega_p^2} - 4\frac{\sigma_m^2}{\omega_m^2}}{(\varepsilon_p + 2\varepsilon_m)^2 - \left(\frac{\sigma_p}{\omega_p} + 2\frac{\sigma_m}{\omega_m}\right)^2} \approx -0.223 < 0 \tag{4.13}$$

When manipulating short, single strands of DNA, the DEP force has been proven to be insucient to hold the molecules down over the electrode and the electroosmotic drag should be dominant. More details on the Clausius-Mossotti factor can be found in the Appendix B.

4.2.3 ACEO driving and quantication

A complete computation of an AC electroosmotic ow would require coupled simulations of the electric eld, charge density, conductivity and uid velocity within the electrical

double layer, as well as computations of the electric eld and uid velocity in the bulk of the device. An alternative is to use a linear capacitance approximation for the double layer and a uid slip boundary condition, just outside the double layer, and based upon the force produced by the electrical eld tangential component on the induced charge in the diusive layer that sets the uid bulk into motion ([106, 107]).

In this work we used the simulation strategy proposed by Gonzalez et al.[106] and, in this section, we will limit to describe the method of solution stating the main equations and boundary conditions applied to the system. The approach has assumed an AC potential (with amplitude V_0 and frequency ω) applied to the electrodes immersed in a symmetric electrolyte with a constant conductivity within the double layer.

The governing equations of electroosmotic ow are:

- The Laplace's equation for electric potential φ:

$$\nabla^2 \varphi = 0 \tag{4.14}$$

here the permittivity of the medium is taken as uniform, as a rst approximation, but it is a function of the concentration of complementary DNA strands in solution.

- The velocity eld, $\vec{u}$, of the uid can be obtained from the incompressible NavierStokes equation that, for low Reynolds number, is given by:

$$\eta \nabla^2 u - \nabla p = 0 \tag{4.15}$$

- together with the mass-conservation equation, which for an incompressible uid is:

$$\nabla \cdot u = 0 \tag{4.16}$$

here, η and p are the uid viscosity and pressure, respectively. The Reynolds number, Re, is dened as:

$$Re = \frac{\rho_m u \cdot l}{\eta} \tag{4.17}$$

for ow in micro-electrode structures is very small, and, in our operating condition ($\eta \simeq 904,1$ μ Pa·s at room temperature and at atmospheric pressure[108]), l is the characteristic travelled length of the uid that we can set equal to 100 μm; $\rho_m \simeq 1098$ kg/m^3[108]) and assuming that the velocity of the particles is in the range 1 - 500 μm s^{-1} ([97, 98, 105, 106, 107, 109]), $1.21 \times 10^{-4} < Re < 6.07 \times 10^{-2}$ can be estimated so that

the low Reynolds number approximation is a valid assumption. For these reasons, the inhomogeneities in the viscosity caused by the temperature field are considered to be small and thus we have not included a term for the gradient of viscosity in the Navier Stokes equation 4.15.

The problem is axi-symmetric around the $r = 0$ axis. The Working electrode is 100 μm in diameter and the buer solution is a 100 mM KCl-doped aqueous solution, with a conductivity of 55 μS/cm.

For computing the electric field, following the pioneering work of Gonzalez's group [106], we can describe the electric potential as a combination of the static surface potential and of the imposed alternating voltage, and thus apply an electrical insulation boundary condition to the rest of the cell. The asymptotic matching boundary condition is:

$$\frac{\partial \tilde{\varphi}}{\partial z} = i\Omega \quad \tilde{\varphi} \pm \frac{V_0}{2} \tag{4.18}$$

where Ω is the so-called non-dimensional frequency and defined as $\Omega = \omega a \sqrt{1 + i\omega}/\lambda_D$.

For the Navier–Stokes simulation, the slip boundary condition, Eq. 4.19, is applied to the electrode surfaces, and no slip to the remaining surfaces. The time-averaged slip velocity $< u_{slip} >$ due to electroosmosis in an AC oscillation is derived from the Helmholtz–Smoluchowski formula[107]:

$$< u_{slip} >= -\frac{m}{2\eta}\Lambda \cdot \mathrm{Re}\left[(\varphi - V_o)\frac{\partial \tilde{\varphi}}{\partial r}\right] \tag{4.19}$$

Here, Λ is a tuning parameter to account for the Stern layer and it is defined as the ratio of the diusive layer potential drop over the total double layer potential drop including the Stern layer:

$$\Lambda = \frac{C_{Stern}}{C_{Stern} + C_{diffuse}} \tag{4.20}$$

and it was taken as 0.25 in the computational analysis[107].

The ACEO velocities are implemented and simulated using the computer algebra program Wolfram Mathematica ver.10 which allows us to compute a finite element analysis of the problem. The Laplace equation (cf. equation 4.14) for the electric potential is first solved in a stationary manner. The electric field distribution so estimated is the used

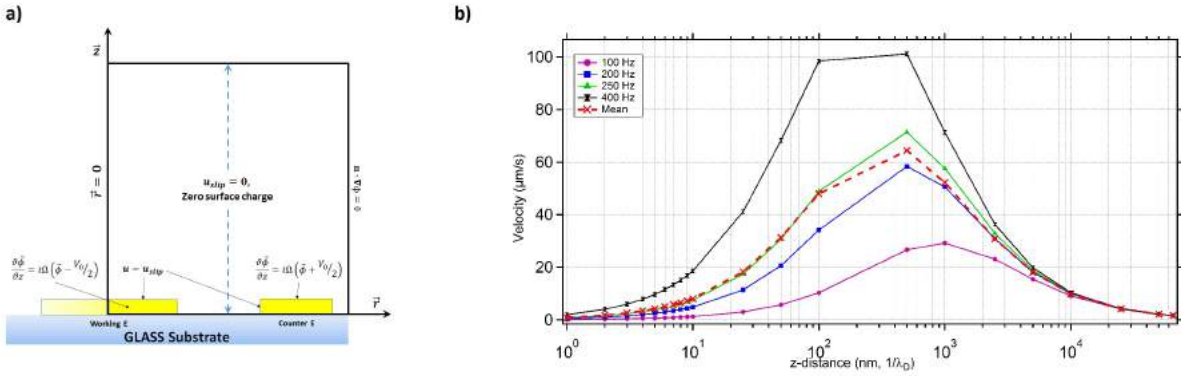

Figure 4.4: a) Boundary conditions for the numerical simulation (not to scale) of the potential and velocity elds. Note that only half of the domain is modelled due to symmetry. b) Velocity of cDNA strands calculated at 100, 200, 250 and 400 Hz as a function of the distance from the working electrode surface with V_{app} = 10 mV in a 100 mM KCl buer solution. The mean velocity is averaged from the velocities obtained for the four frequencies.

as an input to the time-dependent solution of the modied Navier-Stokes equation (cf. equation 4.15) employing linear elements for their solution (small Reynolds number). Figure 4.4a) gives a schematic of the boundary conditions and Figure 4.4b) shows the radial velocities of cDNA strands calculated at 100,200, 250 and 400 Hz as a function of the distance from the working electrode surface.

The results imply and conrm that the ACEO occurs and its velocity decreases with the distance from the electrode surface due to the reduced tangentialelectric eld far from the WE ([98, 107]).

From Figure 4.5b) and c), we can note that the cDNA strands, suspended above the gap between the electrodes are attracted to the WE surface and then, following ACEO uid motion, transported towards the center of the working electrode, where the electric eld has its minimum because of the negative contribution of DEP force, as already stated. The simulation was carried out with an applied voltage of 10 mV at a frequency of 250 Hz.From gure 4.5c), in particular, the radial velocity, within a distance from the electrode equals to the dynamic polarization length[96], was measured to approximately 6 μm/s for an applied voltage of 10 mV peak to peak, a frequency off = 400 Hz, and for an electrical conductivity of σ = 55 μS/cm.

Obviously these calculations are applicable only to the movement of a single isolated cDNA strand, simulated as a spherical particle, and could be used to calculate the

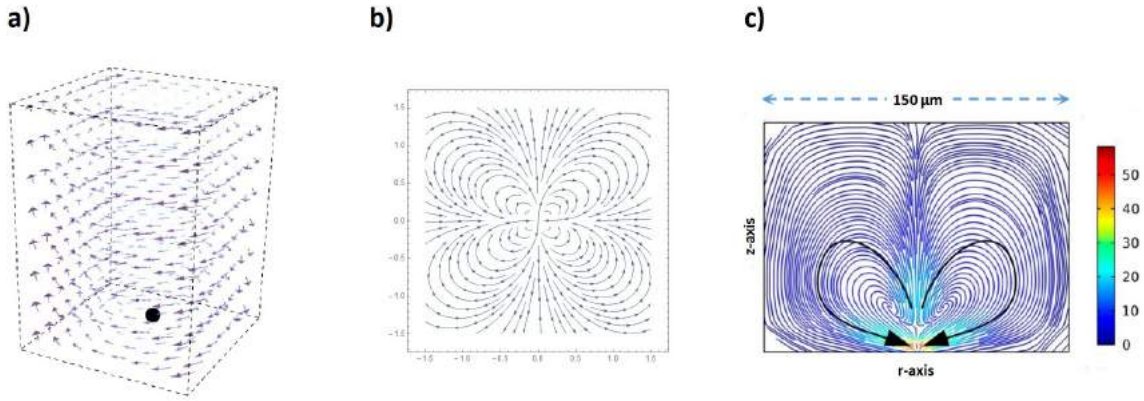

Figure 4.5: Illustration of the AC electroosmosis uid ow of cDNA strands in our capacitance immunosensor. The simulation was carried out with an applied voltage of 10 mV at a frequency of 400 Hz. a) A cartoon showing the motion of a cDNA strand (the spherical particle is not in scale) under the eect of the total electro-uidic ow within a rectangular centered on the working electrode and having a height equal to 67.8 micrometers. b) Shows the variation of $|\nabla E^2|$ on the working electrode surface seen from above, indicating the magnitude and direction of the forces acting on DNA molecules. The sizes of the vectors are drawn on a logarithmic scale in units of $1\,\mu m$. c) Streamline and arrow plot of electroosmosis ow with an applied voltage of 10 mV at a frequency of 400 Hz (color plotted on a log scale, units 10^{-6} m/s).

movement of isolated particles in microelectrode structures. For a collection of particles, a statistical approach must be used to predict the movement and distribution of the ensemble. This approach was chosen not only to simplify the model but also for lack of the computing power required.

Moreover, the modelling of AC electroosmosis as a slip boundary condition based on the tangential component of the potential gradient across the electrode surface (see equation 4.19) is a valid approach, but the linear approximation for determining the potential drop across the electric double layer may not be accurate since it is only valid for small values of potential drops [106].

In addition, although polarizable particles can be moved using non-uniform electrical elds, the electrokinetics forces are not the sole force acting on a particle. The total force on any particle is given by the sum of many forces including sedimentation, Brownian, dielectrophoretic and hydrodynamic forces, the latter arising from viscous drag on the particle.

However, these studies provide a good starting point for further and more accurate

molecular dynamics surveys.

4.3 The nal approach

In the previous section, has been shown that the AC eld induces an electroosmotic circular ow above the working electrode surface. The resulting velocity was found to strongly depend on the frequency and permittivity, and also with properties of the electrical double layer and the applied electric eld, as expected from the conducted bibliographic survey

This velocity prole of equation 4.19 can be integrated to yield the mass carried into our dynamic polarization length by convection. In particular, the electroosmotic ux rate (g/s) into our control volume is given by:

$$\vec{\varphi}_{EO} = [\text{cDNA}] \cdot A_{WE} \cdot \int_0^{\hat{L}} u_{slip}(r) \cdot dr \tag{4.21}$$

where L is the characteristic length of the system sets equal to $1\mu m$ since within this distance we have the peak of velocity (cf. Equation 4.4b)). In this regime, the scaling convective ux rate is:

$$\varphi_{EO} = [\text{cDNA}] \cdot A_{WE} \frac{{}_m V_0^2}{\eta (1 + \Lambda) L \left(\frac{\omega}{\Omega} + \frac{\Omega}{\omega}\right)^2}$$

where V_0 is the applied voltage, and η are the permittivity and viscosity of the liquid (both assumed constant), Λ is the ratio of the diuse-layer to compact-layer capacitances (both assumed constant), and $\Omega = \omega a \sqrt{1 + i\omega}/\lambda_D$ is the peak frequency at the scale of the charging time.

By denition 3.5, the immobilized probes (P) and the targets (T) form hybrids (H), with a forward rate constant k_{on} and a reverse rate constant k_{off}, and thus the rate of formation of H can be written:

$$\frac{\vartheta[H]}{\vartheta t} = k_{on}[P][T] - k_{off}[H] \tag{4.22}$$

where $[P] = [P]_{max} - [H]$, $[P]_{max}$ being the maximum (initial) number of free probes on the surface. By considering the mass transport due to AC electroosmosis, we can

assume an excess of targets $[T]_{exc}$ with respect to their initial value $[T]_0$, within a 1 µm form the electrode surface.The rate of formation of H becomes:

$$\left(\frac{\partial[H]}{\partial t}\right)_{tot} = k_{on}([P]_{max} - [H])[T]_{exc} - k_{off}[H] \tag{4.23}$$

here, $[T]_{exc} = [T]_0 + [T]_{ACEO}$ where $[T]_{ACEO}$ are the targets transported on WE by electrokinetiks ow.

Assuming that there is no hybrid initially, the analytical solution of this dierential equation is:

$$[H]_{tot} = \frac{[T]_{exc} + [P]_{max}}{[T]_{exc} + K_D}\left(1 + \exp\left(-\frac{t}{\tau_{tot}}\right)\right) \tag{4.24}$$

where $K_D = K_A^{-1} = k_{off}/k_{on}$ and $\tau = \frac{1}{k_{on}[T]_{exc} + k_{off}}$.

At the equilibrium, when $\tau_{tot} = \tau$ (τ is the hybridization time calculated using the Langmuir isotherm, equation 3.7, the results for the various [cDNA] are summarized in Table 3 in Appendix A), the fraction of hybridized probes will tend to $\frac{[H]_{eq}}{[P]_{max}} = \frac{[T]_{exc}}{[T]_{exc} + K_D}$. This assumption can be considered valid since the percentage change of C_0 is estimated at the equilibrium, and thus:

$$C_{d\%} = \left[N_{max} + \frac{[T]_{exc}}{[T]_{exc} + K_D} \cdot \frac{K_A \cdot [cDNA]}{1 + K_A \cdot [cDNA]}(1 - \xi_C) \cdot \right] \cdot [1 - \exp(-(k_{on}[cDNA] + k_{off})t)] \times 100 \tag{4.25}$$

where N_{max} will be set equal to 0.49 [76].

Repeating the same procedure described in Section 4.1, we obtained the green markers in Figure 4.6:

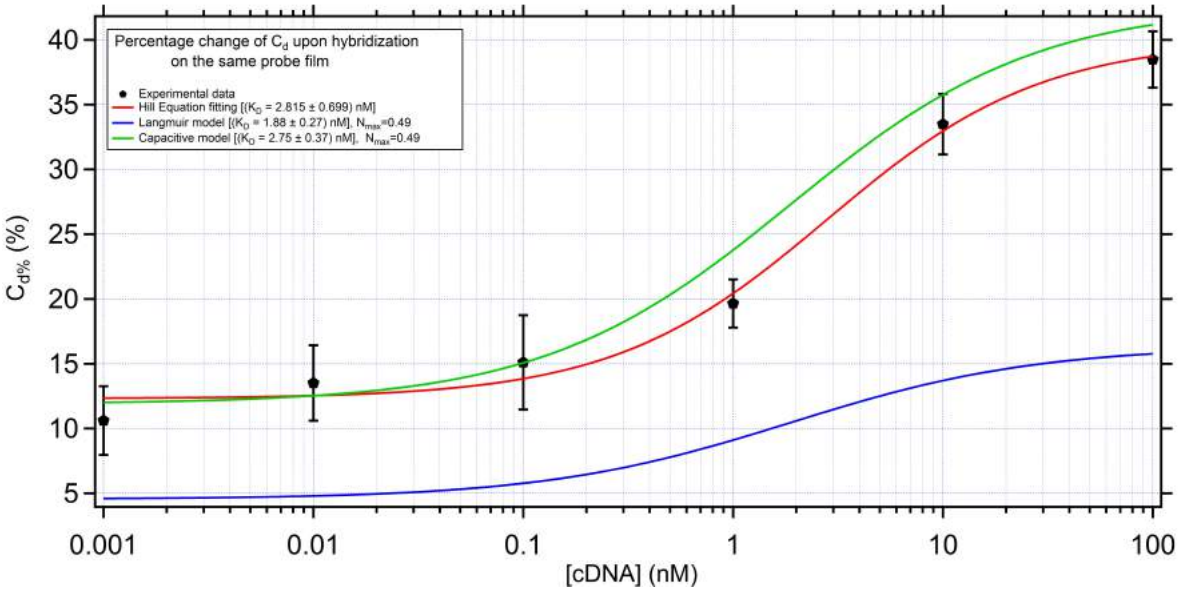

Figure 4.6: $C_{d\%}$ experimentally (red circles) obtained as a function of [cDNA] dissolved in 100 mM KCl buer solution compared with the values got via two theoretical model given by equation 4.6 (blue markers) and by equation 4.25 (green triangles) performed in the same operating conditions.

From Figure 4.6, we can note that the percentage changes of C_d estimated via computational model dier by as much as 8.3 % from the experimental ones; this discrepancy between the theoretical predictions and the experimental electrochemical results, suggests the need for more accurate handling of the electric double layer. In particular, the simulation described in this section, considers ACEO alone without taking into account the eects of Brownian motion. The diusion, in fact, is generally regarded as a `disrupting' force slowing probably the overall hybridization rate. But this will be the topic of further work.

Chapter 5

Detecting miRNAs relevant for heart failure disease

An ideal cancer biomarker should be measured easily, reliably and using a minimally invasive assay with high analytical sensitivity and specicity. In the last few years, detection of fragments of RNA, micro-RNAs (miRNAs), has emerged as a promising approach for studying and monitoring gene expression in a wide range of physiologic and pathologic processes. These RNAs are small, non-coding, 18 to 24-nucleotide single-stranded sequences that are involved in gene regulation, aecting essential processes such as cell proliferation, cell death, tumor genesis, and mammalian cell development [110]. Due to their small size and their easy degradation, miRNAs are dicult to be detected using conventional methods, [111, 112, 113]. There is then a pressing need for rapid, label-free detection methods, which would speed up ongoing research in understanding their role in gene regulation and disease development.

From the rst evidence of the role of miRNAs in disease development, as demonstrated by Croce and co-workers in 2002 [114], many other studies have been conducted proving that proling of circulating miRNAs may help for the early detection, prognosis and even treatment of world spread diseases, from dierent types of cancer to cardiovascular diseases. Nowadays, the ocial miRNA database (miRBase, [115]) lists ~ 540 human miRNAs some of which connected to various pathological conditions. Low expression of miR-29 and miR-181 families[1], and miR-223 were found to be strongly associated with disease progression in chronic lymphocytic leukemia (CLL) [116]. Schwarzenbach

[1] members diering by as little as one nucleotid

et al. [117], provided evidence that patients at advanced tumor stages had signicantly higher miR-34a and miR-155 levelthan patients at early tumor stages. miR-486 overexpression was detected in samples from younger patients with uterine cancer tumors [118]. Moreover, miRNAs can be detected in blood and body uids as well as in tissues, thus making possible non-invasive collection of samples [119].

In recent years, in fact, the measurement of blood-, and its components, impedance through an alternating current has been suggested as a non-invasive approach to determine some blood disorders[6]. Moreover, circulating miRNAs can be readily detected in serum [120] plasma or whole blood [121], with a notable stability in serum and plasma [122]. Mitchell et al. found that plasma miRNAs could remain stable in room temperature for 24 hours and eight freeze-thaw cycles; however, synthetic miRNAs were rapidly degraded in plasma. This indicates that the endogenous plasma miRNAs in RNase-enriched circulating system exist in a form that is resistant to plasma RNase activity [123].

Here, we examined a family of miRNAs connected to several diseases ranging from glioblastoma [124] to gastric cancer [125] to cardiac hypertrophy [126]. In particular, the purpose of the present study was to challenge our device to detect fragments of RNA coming from patients with heart failure [127, 128] in complex matrices, as human extract and plasma.

5.1 Quantication of free circulating miRNA in cellular extract

In order to prove the capabilities of our homemade biosensor to quantify microRNAs, we detected the DNA/miRNA hybridization in 100 mM KCl saline buer. We proceeded to the immobilization of a thiolated oligosequence incubated for 12 minutes and complementary to the human microRNA hsa-miR-451a miRNA. The probe density has been selected as the most suitable for the detection of hybridization processes,as already shown in Section 3.1.

The C_d at the WE was then measured until its stability was achieved, as shown in Figure 5.1a), orange markers. Successively, hybridization (blue curve in Figure 5.1a)) was carried out with 100 pM of complementary miRNA target. Fitting the experimental data obtained using a Langmuir rst order equation rate ($\chi^2_v \approx 1.7$), eq. 3.7, we

estimated an hybridization time of τ ' (12.34 ± 0.25) min.

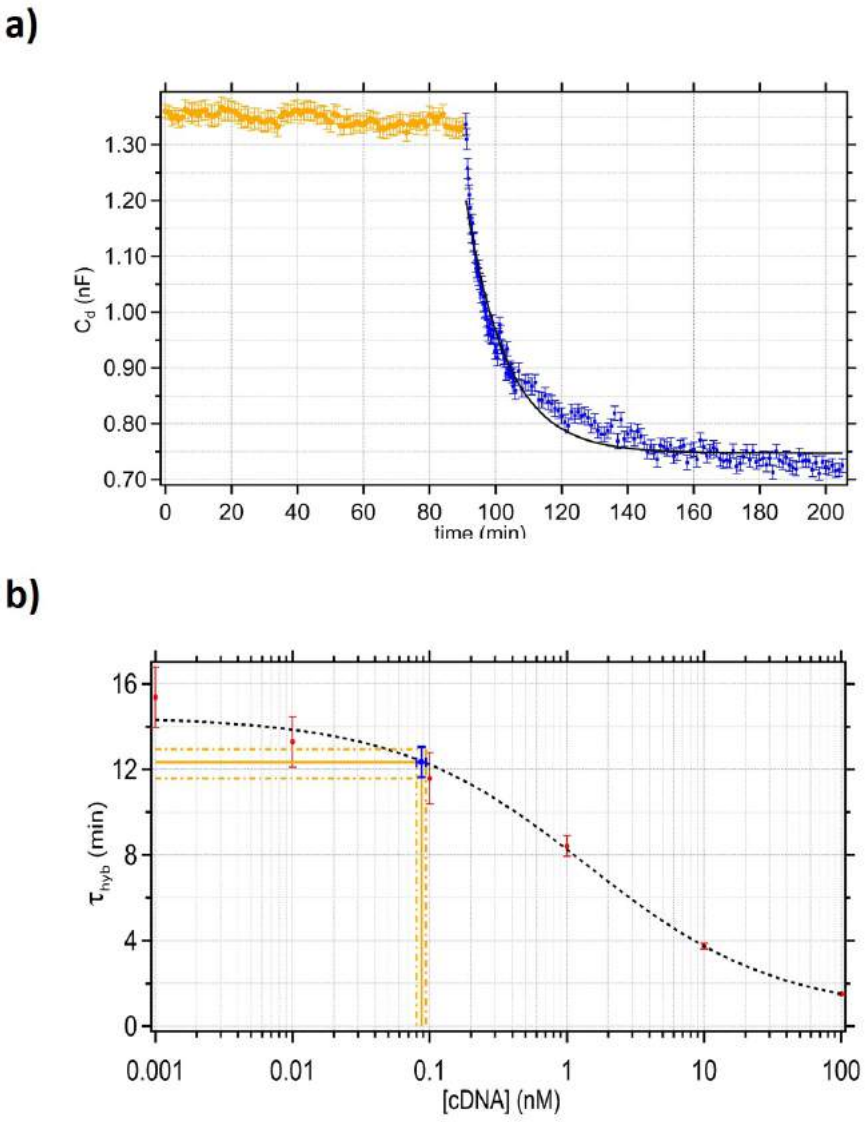

Figure 5.1: Study of the kinetics of miRNA-hybridization via dierential capacitance measurements.a) DNA/miRNA detection (blue signal) in KCl 100mM on DNA-probe lm (orange markers) 12 minutes incubated.The black solid line represents the t based on rst-order Langmuir adsorption model. b) Plot in a semi-Log scale of the hybridization time (red points) as function of [cDNA] in the range of values [1pM; 100nM]. The black dashed line is the Hill Equation t, Eq. 3.4. The solid orange line represents the [miRNA] extrapolated from kinetics studies, whereas the dashed orange lines represent one standard deviation around this value.

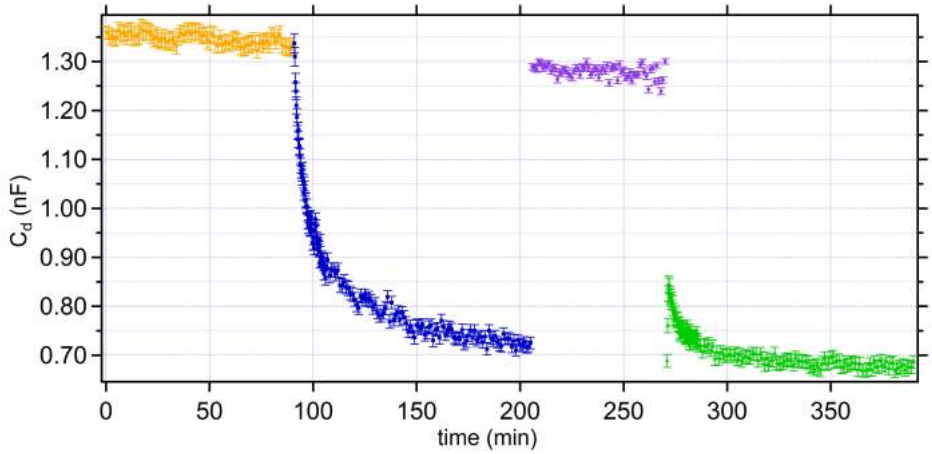

Figure 5.2: Comparison of DNA/RNA-hybridization kinetics for miRNA target molecules (has-miR-451a) on same probe lm in dierent solutions: blue curve in KCl 100mM; green markers in cell extract diluted (1:2) in RNase-free water.

Interpolating this value with the data (red points) of Figure 5.1b) we derived a target concentration of (87 ± 7) pM. The slower kinetics is due to the higher complexity of DNA/miRNA hybridization with respect to the standard DNA/DNA hybridization in saline buer. In fact, miRNAs are more prone to the formation of secondary structures (e.g. hairpins) and need a higher time to deploy themselves and hybridize. From this rst result, we can say however that DNA/DNA hybridization calibration curves represent a good mean to estimate DNA/RNA hybridization parameters too.

We moved forward and investigated the performance of our biosensor in a more complex biological environment. A second blind experiment was thus performed on the same regenerated probe lm (the used procedure is described in Section 2.5.1) and then complementary miRNA in cell extract of patient cells was detected.

The measurements were carried out by adopting the same procedure described in the previous chapter, the only expedient made, was to prepare the solutions, containing miRNAs, not later than one hours before use because of their rapid degradation; and also we used RNAse free water (MP Biomedicals) to dilute (ratio 1:2) extract plasma sample to prevent miRNA degradation by these enzymes.

Figure 5.2 shows the blind miRNA-detection from human extract (green triangles) compared with a DNA/miRNA hybridization recognition performed on the same probe-SAM but in 100 mM KCl salt solution. To quantity the unknown concentration of miRNA in extract, we used the calibration curve in Figure 3.5. By adopting the Langmuir

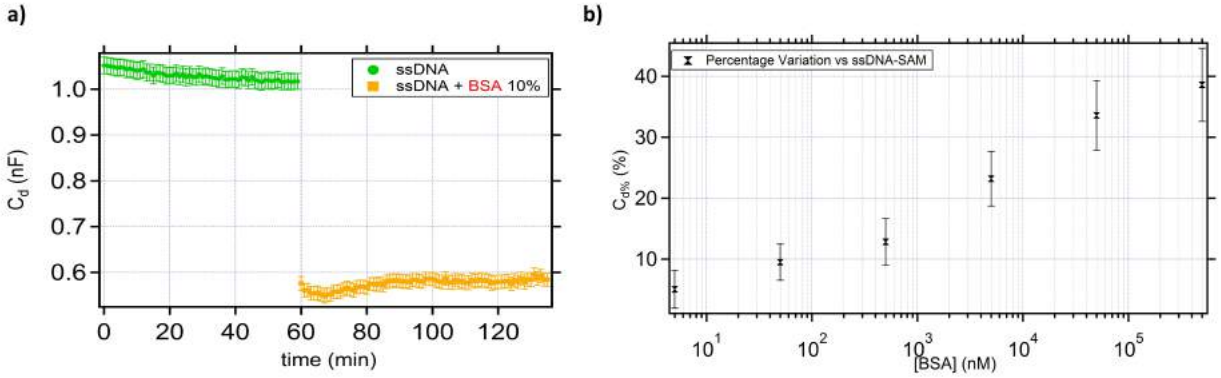

Figure 5.3: a) Eects, in time, on the measured C_d at the ssDNA functionalized WE due to the presence in solution of 10% of BSA (Bovine serum Albuin) and b) percentage change of C_d obtained dissolving increasing concentrations of BSA on the same probe lm.

adsorption model a hybridization time of about 10 minutes was obtained. The nal miRNA concentration, taking into account the dilution ratio, was calculated to be $\approx$ 1.5 nM, quite comparable with the one estimated by the real time qPCR (qRT-PCR) used by MD Daniela Cesselli and her co-workers at University of Udine.

Remarkably, hybridization kinetics curves were well dened also in complex matrices. The main dierence with respect to the kinetics in saline buer is in the initial stepwise decrease of C_d. We associated this gap to the blocking eect carried by protein contaminants (mostly HSA) in the cell extract. To prove it, we monitored the eect of BSA (Bovine Serum Albumin) on the dierential capacitance of a ssDNA SAM. Usually, BSA exerts a blocking action, binding aspecically on ssDNA-SAM, as proved by the absence of any typical absorption kinetics (yellow curve in Figure 5.3a)) in correspondence to the addition of 10% BSA to the saline buer, KCl 100mM. This C_d fall can be rationalized assuming an exchange reaction of the aspecically bound proteins with a given number of adsorbed ions reducing the average dielectric constant of the molecular layer. The amount of such C_d reduction is BSA-concentration dependent, as can be seen in Figure 5.3b), which means that a greater variation corresponds to a higher concentration of protein contaminants.

5.2 Device specicity in Human Plasma

In order to estimate DNA-miRNA binding specicity, the working electrode was functionalized, for 15 minutes, with a solution containing 1 µM of a thiolated ssDNA sequence (mmu-miR-351-5p-comp-SH) complementary to the murine mmu-miR-351-5p miRNA (sequence in section 2.5). The experiment has been performed in PBS 1x (Ionic strength 162.7 mM and pH = 7.4) used also to dilute plasma samples. We used an applied potential of 75 mV in order to overcome the Coulomb repulsion among strands and thus increase the biorecognition sensitivity in a so complex environment as human plasma. We placed attention, however, to keep applied potential low enough to avoid even a partial electrochemically desorption of the thiolated probe molecules of the SAM.

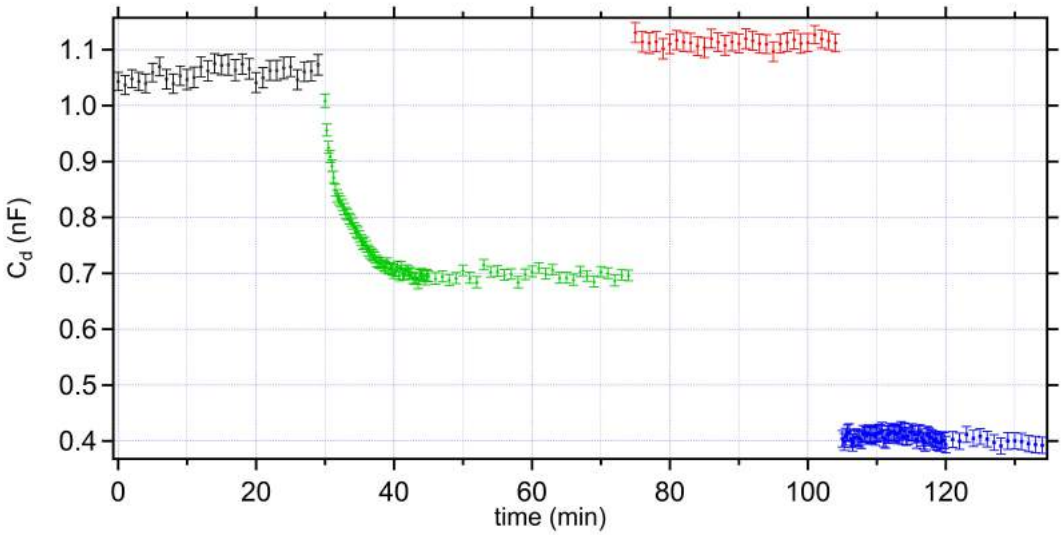

Figure 5.4: Device specicity has been tested. EIS measurements in PBS 1x buer solution, with an applied potential of 75mV for the WE functionalized with not human ssDNA-SAM complementary to a murine miRNA sequence. Black curve shows the dierential capacitance at ssDNA-probe and green triangles are connected to the hybridization process with mouse miRNA complementary sequence. Red curve is the C_d measured at the ssDNA-SAM regenerated WE whereas the blue signal shows the lack of hybridization, evident from the absence of the usual kinetics, after the addition of a human plasma sample diluted 1:3 in PBS 1x.

From Figure 5.4, attested the stability of the dierential capacitance (black markers) at the functionalized WE, the DNA/miRNA hybridization detection (green signal) was run with complementary murine miRNA in concentration of 1 µM until its saturation

(τ ' (2.92 ± 0.09) minutes; $\eta \approx 34.3\%$; results were obtained using the Langmuir adsorption model χ^2_v ' 1.19)

After having performed the hybridization of the sample, the thermal regeneration of the DNA/miRNA layer was carried out. The measured value of C_d corresponding to the de-hybridized ssDNA functionalized WE (red circles) suggested that a complete dehybridization process had occurred. We then tested the response of the device upon its specicity through the use of a human plasma sample containing miRNAs relevant for heart failure disease and diluted 1:3 in PBS 1X. Paying attention to the blue curve in Figure 5.4, we can observe a capacitance decrease versus time, without showing the usual hybridization kinetics. This is a demonstration that the SAM is not hybridized as might be expected since the murine ssDNA has a specic sequence not traceable in human bloodstream. In addition, it is possible to note a signal due to protein contaminants with its characteristic gap.

These results give useful and reliable information on the expression of miRNAs in extracts from plasma samples. Moreover, from these studies, three basic information are worth being highlighted:

- The hybridization kinetics curve represents eectively the bonding between a sequence and its complementary one and this is even true in human plasma environments, making our device an optimal candidate for clinical use;
- Moving from a simple saline buer (KCl, $MgCl_2$, PBS, etc.) to a more complex environment (extract, human plasma and so on), a signal gap can be observed, unequivocally associated to aspecic binding carried by protein components in the sample which screens the applied potential and increases the steric hindrance without preventing a correct monitoring of hybridization events.
- Last but not least, the calibration curves, developed from the studies on DNA/DNA hybridization in a pure salt solution, can be used to precisely quantify the amount of miRNAs in cell extract and in human plasma. Implications of this will be commented in the following section.

5.3 miRNA detection in Human Plasma

Here we applied our label-free biosensor as a proof of principle platform for the detection of a miRNA target (called hsa-miR-154-5p) relevant to human diseases [124, 125, 126,

127, 128], in human plasma samples coming from patients having dierent levels of heart failure. No amplication scheme has been adopted in our EIS setup.

To move towards the detection of blood circulating miRNAs, we monitored DNA/miRNA hybridization in human plasma samples using PBS 1x both as buer solution and to dilute the human plasma samples, choosing a SAM incubation time of 15 minutes and applying an AC voltage with an amplitude of 150 mV.

As already said, in this kind of samples, we ignore not only the concentration of the specic circulating miRNAs but also the concentration and type of contaminants (other miRNAs, proteins, solvents, etc.) present in it. To avoid false positives, it was decided to carry out electrochemical measurements of the same sample in serial dilution (1:20, 1:4 and 1:3) and results are shown in Figure 5.5a). To regenerate the device has been considered a two-step cleaning protocol: the electrode is soaked in a solution of PBS containing Tween 1.25% for a certain time depending on the dilution previously used (i.e. higher is the dilution ratio higher will be the soaking time) and then exposing the slide to the usual thermal treatment (details in Section 2.5.1) in order to promote the breaking of hydrogen bonds between the nucleotide bases.

Again, with reference to Figure 5.5b), it is also possible to underline increasing the concentration of the sample in solution, i.e. the dilution ratio from 1:20 to 1:3, the increase in the gap between the ssDNA G_0 value and the one immediately after the addition of sample to the experimental pool. This can be explained by a greater blocking eect carried by proteins in plasma. In addition, the reduction of the hybridization time is consistent with the increase in plasma concentration in the experimental pool.

However, in human plasma, miRNAs are protected (Figure 5.6) by enzymatic degradation (Ribonuclease, commonly abbreviated RNase, as essential catalytic components of the RNA-induced silencing complex (RISC) [129, 130]) either being encapsulated within nanovesicles called exosomes or linked to large protecting proteins ($\approx$ 110 kDa) called Argonautes (AGO). Readers interested in the technical details can nd a very nice explanation in Kupferschmidt's work [131].

5.3.1 The Argonaute factor

Although miRNAs enclosed inside the exosomes cannot be observed by EIS measurements at our applied frequencies, the bonding to these Argonaute proteins makes dicult to estimate a proper concentration of circulating miRNAs of interest because oftheir

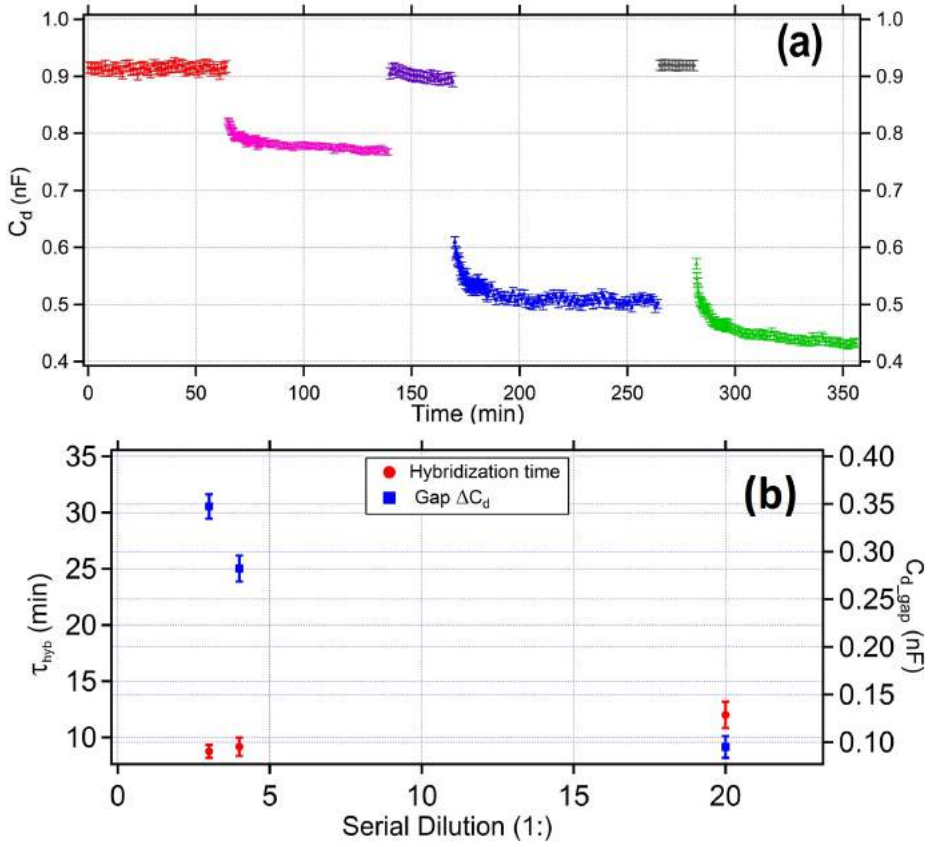

Figure 5.5: Detection of DNA/miRNA Hybridization in Human Plasma. a) The DNA/miRNA hybridization experiments performed here were run diluting the plasma sample, coming from an anonymous patient (AP60), in three dierent ratios:1:20 (pink hourglasses); 1:4 (blue squares) and 1:3 (green triangles). The ssDNA functionalized WE (red curve) was measured, as a reference, in pure PBS 1x buer. For all the measurements, we set an AC voltage of 150 mV amplitude. The regeneration of the ssDNA-SAM (purple and black markers) is carried out using a two-step cleaning protocol. b) Hybridization time (red markers) and proteins blocking eect on C_d (blue points), as a function of the dilution ratio of the plasma sample in PBS 1x. All the measurements are performed on the same sample.

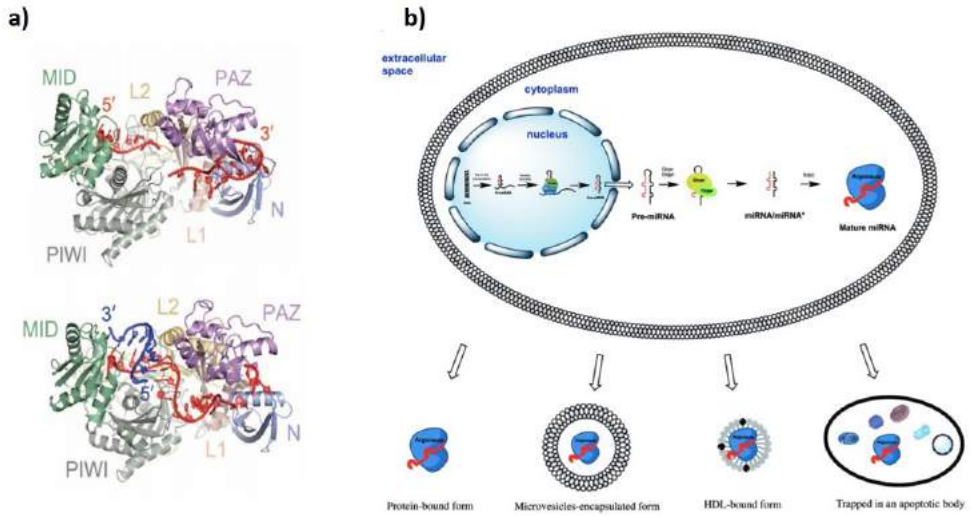

Figure 5.6: a) Schematic of the Argonaute primary sequence and top views of human AGO bound to a dened guide RNA (red) and target RNA (blue). Images from [129]. b) The biogenesis of miRNAs. The extracellular miRNA can be either solely AGO protein-associated or additionally encapsulated into apoptotic bodies, microvesicles, and HDL particles. Image from [132].

steric hindrance (increase in the gap) and their eects on the kinetics of the miRNA recombination (which is expected to increase the hybridization time). For these reasons, we should think about a better way to calibrate this system.

In order to understand Argonaute contribution in the hybridization process a new calibration curve is proposed. By adopting the same experimental conditions, in buer solution composed of PBS 1x and BSA at physiological concentration (4.25 g/dl = 4.51 µM, Normal Ranges for Common Laboratory Tests, Rush University), we hybridized our ssDNA-SAM with a Biotinilated-cDNA strand conjugated with a known concentration of Streptavidin with the aim of simulating Argonaute behavior in kinetics (MW $_{Strep}$ ' 60 kDa Vs MW $_{AGO}$ ' 110 kDa). These experiments were carried out in a PBS 1x + 5µl BSA since albumin is the main component (~ 60%) of plasma proteins [133].

A set of ve hybridization / de-hybridization cycles was performed, each time increasing the concentration of streptavidin in solution, from 100 pM to 100nM, regenerating the functionalized ssDNA-WE with the two-step cleaning protocol previously described. The results of these experiments are shown in Figure 5.7.

From Figure 5.7a) we can appreciate the usual concentration dependence of the hybridization kinetics. In fact, increasing the concentration of conjugated streptavidin,

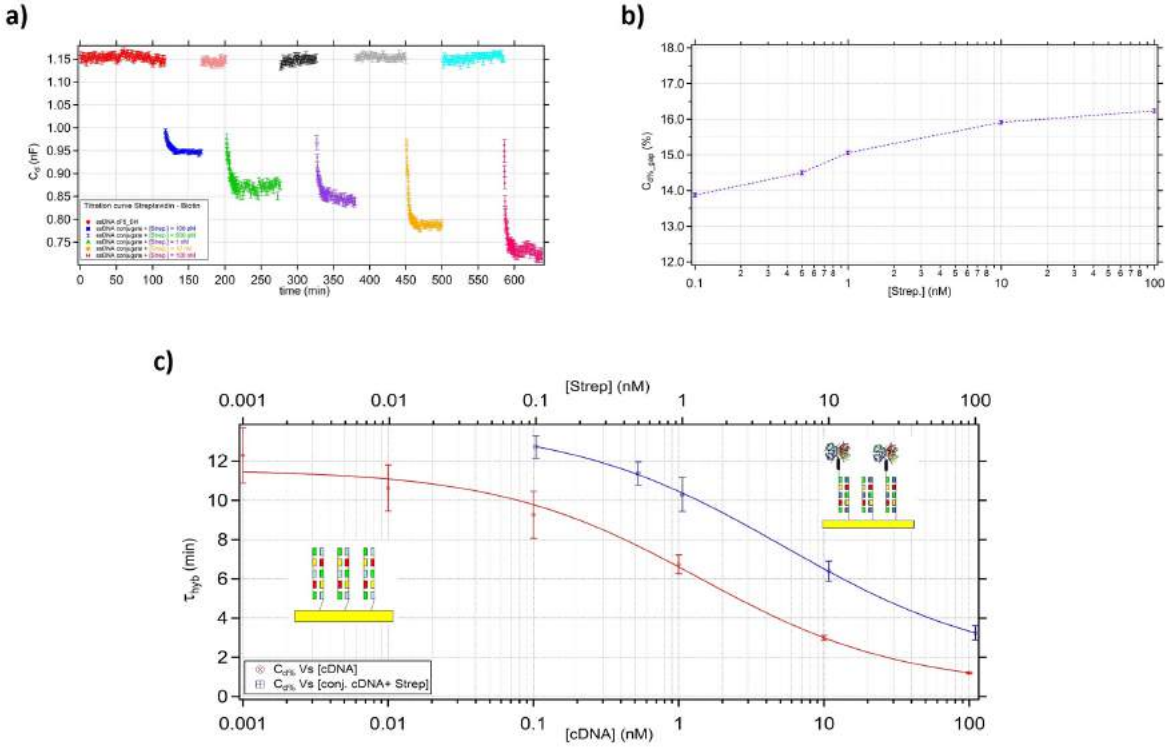

Figure 5.7: a) Titration curve for ssDNA-SAM hybridized with a biotinilated-DNA complementary strand conjugated with dierent concentration of streptavidin ranging from 100 pM to 100 nM. b) Percentage gap in C_d due to protein eect as a function of the concentration of Streptavidin conjugated. c) Hybridization times as a function of concentration of complementary solution.In blue we plot complementary DNA conjugated with Streptavidin, in red DNA/cDNA detection.

we can observe a greater variation,in terms of hybridization eciency, related to the larger number of hybridized sites on the gold electrode.In addition, from Figure 5.7b) we can conclude that our biosensor is also sensitive to higher hindrance due to the growing concentration of streptavidin in solution being the BSA concentration constant along the entire measure.Using the 1st-order Langmuir adsorption kinetics (equation 3.7), we can estimate, referring to Figure 5.7c), the hybridization time connected to the pairing with Streptavidin conjugated strands (blue markers) and compare them with a classical DNA/cDNA hybridization calibration data (red points) obtained in the same conditions of buer solution (PBS 1x + [BSA] = 5 µM) and setting an AC potential with the same amplitude (150 mV).

Furthermore, in Figure 5.7c), we note that the hybridization times are higher (which

means that we are measuring a slower kinetics) in the case with Streptavidin due to the abovementioned twofold eect: the Streptavidin acts as a screening factor, limiting the eect of the applied potential on the mobility of complementary strands and conjugated strands diuse slowly due to their increase in mass and steric hindrance.

5.3.2 Circulating miRNA concentration in Human Plasma

Experiments were then performed for nine dierent human plasma samples to attest the reproducibility of measurements and methods.

The calibration curves shown in Figure 5.7c) can be so used to estimate circulating hsa-miR-154-5p miRNA concentration in blood plasma samples coming from nine different patients. The plasma samples are provided by the MDs D. Cesselli's and A.P. Beltrami's group cataloged in two dierent sets called AP and LV, respectively. The results are listed according to their denomination (AP, LV) and presented in Figures 5.8 and 5.9.

Dierent miRNA concentrations should indicate dierent level of disease.

From Figure 5.9b), higher (2.5 fold) miRNA levels were found in plasma samples belonging to the set named LV with respect to the other group of samples.The results of our blind test will be soon compared by our collaborators in Udine with those derived by real time PCR to conrm that LV-plasma samples have a comparable up-regulation of miRNAs in question. Of course, the statistics needs to be increased to demonstrate that our device can be applicable for clinical purposes.

We are condent that our device, will constitute a sensitive, fast and cheap point-of-care device for medicaldiagnostics/prognosis and for the monitoring of the eect of a therapy from liquid biopsies, at the single patient level.

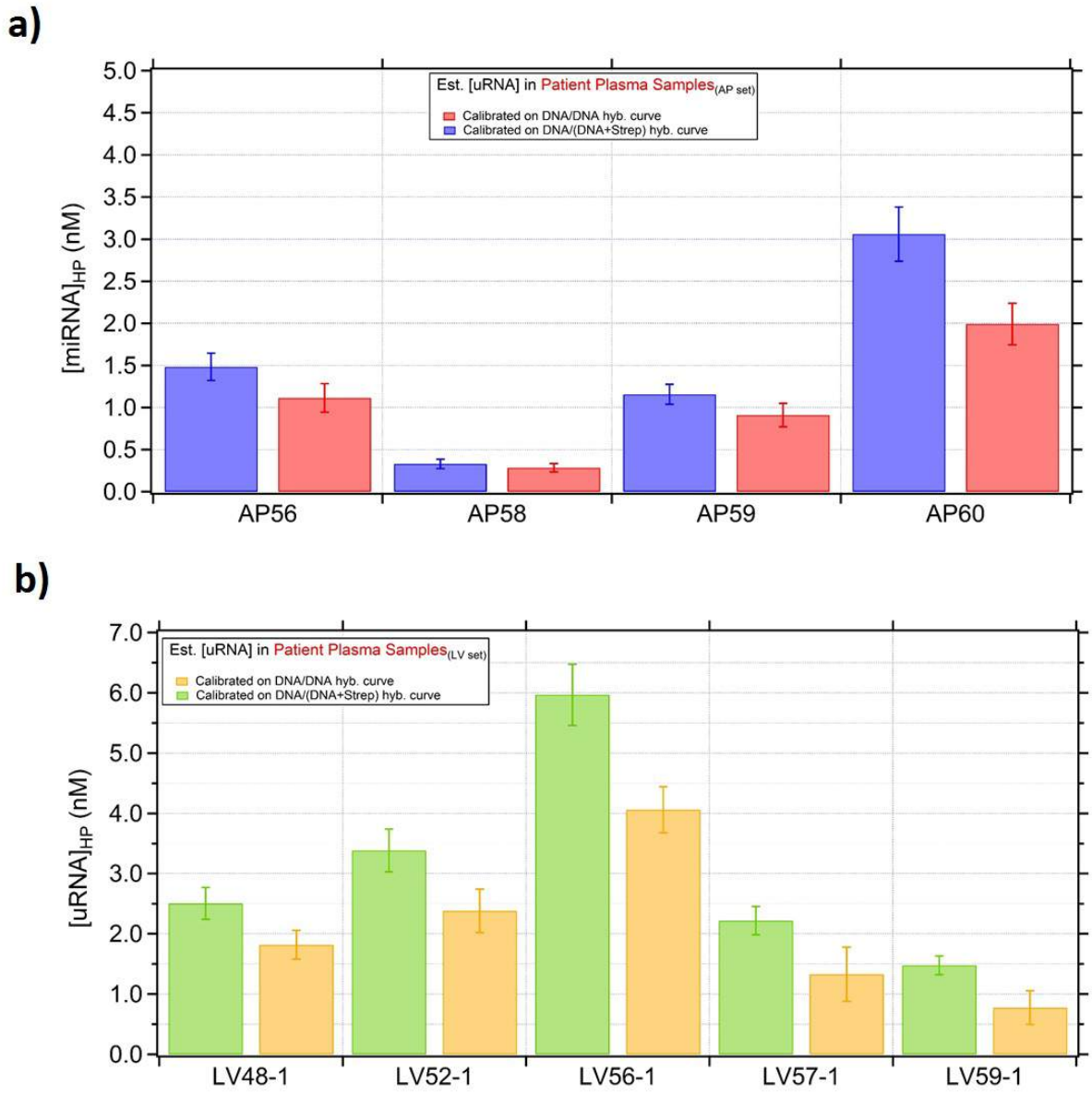

Figure 5.8: Estimation of hsa-miR-154-5p miRNA concentration in blood plasma samples coming from nine dierent patients listed according to their denomination using as reference the titration curve DNA/DNA (red and orange in a) and b), respectively) and the calibration curve DNA/(DNA+Strep) (blue and green in a) and b), respectively). a) AP -set and b) LV set.

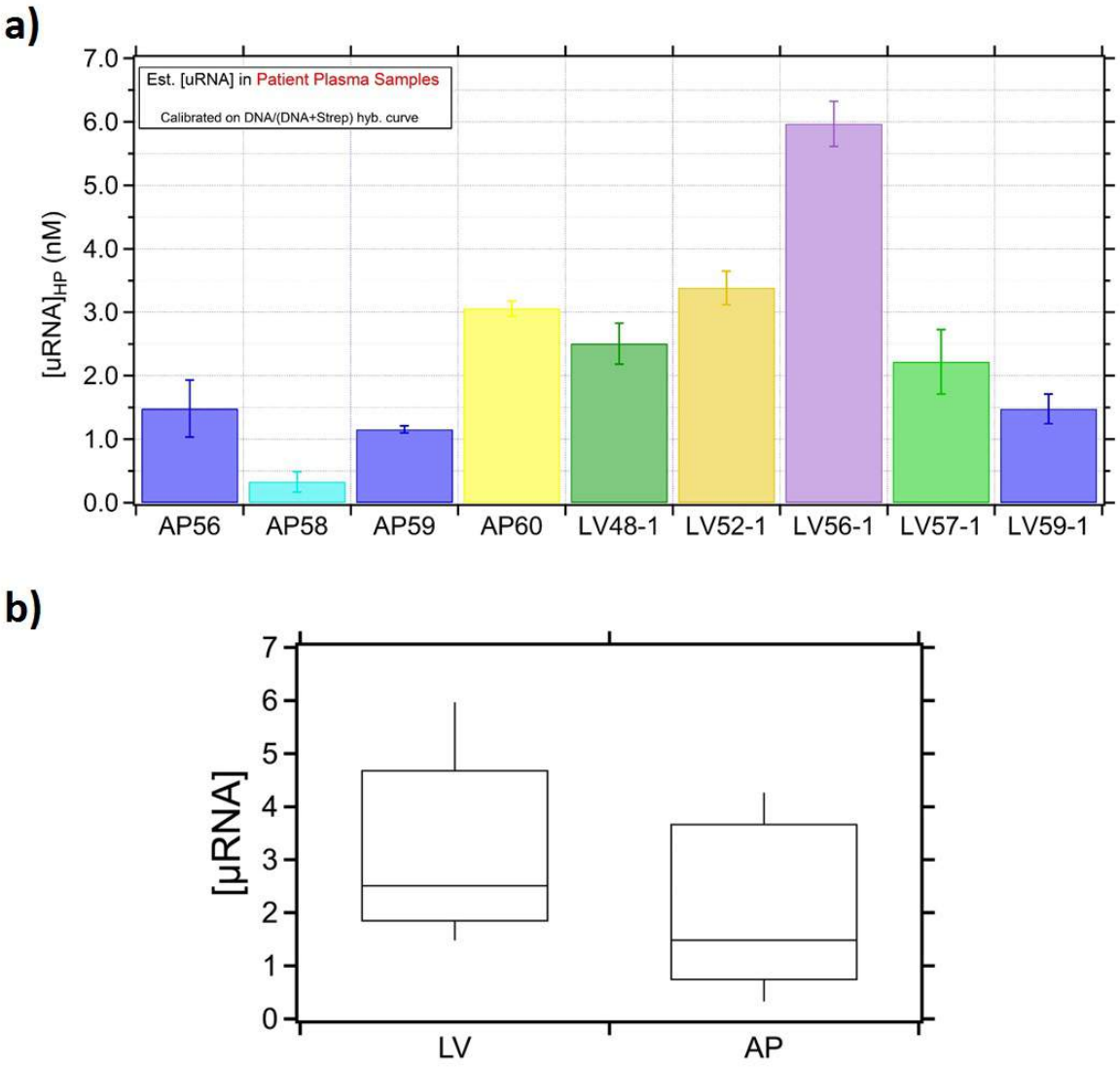

Figure 5.9: a) Summary histogram on extrapolated hsa-miR-154-5p miRNA concentrations in blood plasma samples by use of the DNA/(DNA+Strep.) calibration curve. b) Box plot allows us to graphically depict, in a convenient way, our experimental data presented in the histogram in Figure a).

Chapter 6

Protein Detection: HER2 (Breast Cancer Biomarker)

Breast cancer is the most frequently diagnosed cancer, accounting for 23% of the total cancer cases and 14% of the cancer deaths. However, breast cancer is not considered to be a single disease but rather as a group of diseases distinguished by different molecular subtypes, risk factors, clinical behaviors, and responses to treatment and that is why, nowadays, few different methods are used for breast cancer detection. These depend on woman's age and usually include mammography and clinical breast examination (CBE), as well as magnetic resonance imaging (MRI) for women at high risk.

Different biological markers were proposed for breast cancer screening, including the presence or absence of Estrogen Receptors (ER+/ER-), Progesterone Receptors (PR+/PR-), and Human Epidermal growth factor Receptor 2 (HER2+/HER2-). In particular, we have focused on the detection of the protein HER2 whose overexpression is seen in 20% to 30% of breast cancer and which confers worse biological behavior and clinical aggressiveness. HER2, is a 185 kDa transmembrane receptor in the Human Epidermal Growth Factor Receptor family, has a structure which constitutes of three main parts: a cysteine-rich extracellular growth factor (ligand) binding domain, a lipophilic transmembrane segment and an intracellular tyrosine kinase domain with a regulatory carboxyl-terminal segment [134] (see Figure 6.1c) for a schematic representation).

As discussed along this work, capture molecules with high specicity and selectivity are the essential prerequisite for the design and fabrication of protein nanoarrays and several efforts have been seeking for the assortment of well-characterized anity-based molecules. Besides classical human or humanized antibodies, the so called nanobodies

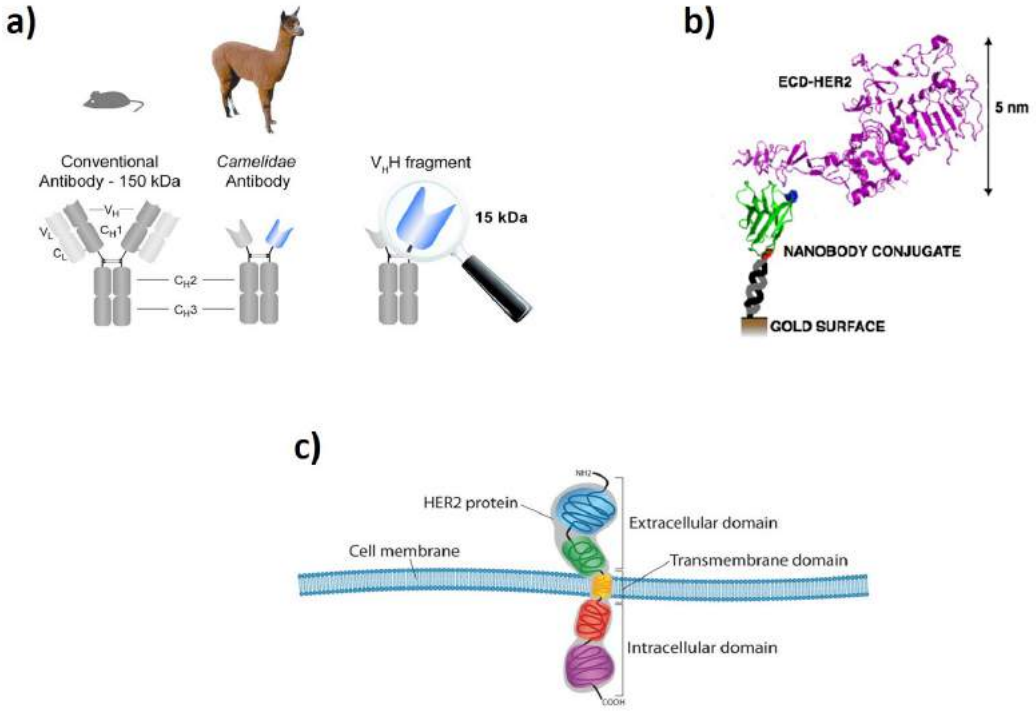

Figure 6.1: a) Schematic cartoon of human antibody, composed by light and heavy chains and camelidae antibody with a representation of nanobody domain (camelid VHH and human VH and VL). b) Schematic representation of ECD-HER2 capture from biosensor. c) Schematic representation of HER2 structure across cell membrane; in purple and red the intracellular domain, in yellow the transmembrane domain and in blue and green the extracellular domain.

constitutes a novel class of reliable and robust binders.

Based on their structure (focus on Figure 6.1a) for details and comparison), these peculiar camelid antibodies have been named Heavy Chain Antibodies (hcAb), as they are composed ofheavy chains only and are devoid of light chains. In the absence of light chains, the fragment-antigen-binding (fab) part of these antibodies is reduced to a single domain, the so called VHH (variable domain of heavy chain antibodies) domain or nanobody. This single domain contains a complete antigen binding site and is the smallest functional antigen binding fragment (around 15 kDa, only one tenth the size of a conventional antibody). The shrunken dimension of the nanobodies encloses considerable advantages allowing the targeting of otherwise inaccessible epitopes [135], (e.g. catalytic centers of enzymes).Nanobodies, can be easily selected and produced in bacteria, ensuring their virtually unlimited supply in constant quality and are exceptionally

stable, with standing conditions of extreme temperatures and pH: nanobodies shelf life is in fact excellent, they can be stored for months at 4°C maintaining the biological activity, and under stringent conditions, are robust and resist to thermal and chemicaldenaturation [136]. Moreover, the intrinsic protein stability constitutes an important probe design factor which means that it can be easily engineered into antibodies constructs of dierent chemical nature [137].

Here, we have focused our attention on the detection of the extracellular domain (ECD) of HER2, which is a shed fragment of approximately 105110 kDa soluble and measurable in the serum fraction of blood, constituting an optimal candidate as a blood-circulating biomarker for HER2 positive breast cancer [138].

There are dierent screening techniques that are used to detect HER2 positive breast cancer: as Immunoistochemistry for detecting HER2 protein overxepression in tissue sections using or ELISA-tests to quantify and monitor the concentration of circulating HER2-ECD released into the serum. Both techniques make use of a combination of monoclonal or polyclonal antibodies. However, recently [139], the American Society of Clinical Oncology College of American Pathologists (ASCO-CAP) denounced the inaccuracy of the current HER2 testing methods both as regards the sensitivity that the inadequacy in the single HER2 detection.

The quest for an accurate and reliable method for routine HER2 testing, also in parrallel with other relevant markers, is becoming an increasingly crucial issue, to improve the ecency of the diagnosis and the response to HER2-targeted therapy.

6.1 ECD-HER2 Detection

Towards this goal, we decided to set up a device for circulating ECD-HER2 detection based on EIS. To eciently detect ECD-HER2, we used a specic VHH, provided by the group of Ario de Marco. Instead of binding the VHH directly on the WE, we capitalized on the experience already gained on DNA SAM formation.We created a ssDNA SAM, as extensively explained in the present thesis work, of an oligonucleotide complementary to the DNA tail previously conjugated to the VHH. Then, we loaded the complementary (c)DNA-VHH conjugate, which linked to the DNA SAM via Watson-Crick base pairing, within a scheme which is known as DNA-Directed Immobilization (DDI).

To create DNA-VHH chimeric constructs we used a maleimide reactiona malemide-terminated ssDNA was used to react to the solfhydryl group present on the cysteine of

the VHH protein to create a stable thioether bond not reversible and cystein specic, which confers to the conjugated a precise orientation with respect to the ssDNA.

6.1.1 Nanobody conjugation via Maleimide reaction

We used a nanobody identied as VHH-A10 selected for its highest anity (measured by SPR-Biacore tests: $k_{on} = 4.95\times10^{6}\ M^{-1}\cdot s^{-1}$; $K_D = 1.7$ nM) among a group of nanobodies that recognize ECD-HER2[140, 141], engineered by our collaborating partners at the University of Nova Gorica in Slovenia, Dr. Ario de Marco.

To start the maleimide reaction, the VHH-nanobody, containing a Cysteine at the C-terminus, was dissolved to a concentration of 100 µM in Hepes 10 mM pH 7.4 buer and reduced adding TCEP in 10-fold molar excess with respect to the protein concentration. The reduction was carried out at room temperature for 20 minutes. A ssDNA F9-maleimide (5'-gtg gaa agt ggc aat cgt gaa g-3 ', purchased from Biomers GmbH Ulm, Germany) dissolved in TE buer (Tris 10mM, EDTA 1mM) pH 8.0 and then added to the nanobody with a molar ratio (ssDNA: protein) of 10:1 (250 µM:25 µM). These components reacted for 2 hours at room temperature. At the end the modied nanobody was puried from reactants and reaction by products with G-25 Illustra Microspin Columns (GE Healthcare Life Science).

The immobilization of the ssDNA-nanobody conjugate was performed, incubating before the thiolated complementary ssDNA ($HS-(CH_2)_6$-5'-ctt cac gat tgc cac ttt cca c-3', called F9-SH) in TE buer with 1M NaCl for 15 minutes (red circles in Figure 6.2) in order to obtain a low density monolayer self-assembled on the gold WE surface (as described in Section 2.5). At this point, the created SAM was used to load 110 nM protein-DNA conjugates via DDI. The high concentration of the conjugate was chosen in order to create a dense layer protein binders on the original DNA SAM. Then, we challenged the device for the detection of ECD-HER2, by applying a bias of 75 mV (blue squares in Figure 6.2). This value of the AC voltage was optimized to the new binding SAM in which the binders are set at a distance from the WE surface of about 4 nm, with a constant charge density area (see Chapter 3) higher that for the case of DNA SAM (cf. Figure 6.1b)).

We started with the measurement of the capacitance signal in KCl 100 mM. Prior to SAM-formation we performed the plasma etching procedure. In Figure 6.2 we show the experimental results. Having attested the success of the hybridization process between

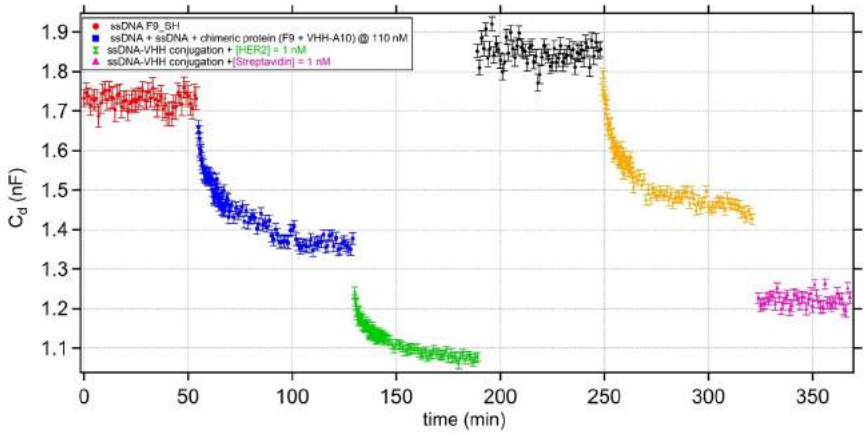

Figure 6.2: ECD-HER2 detection via chimeric-protein binding in KCl 100 mM salt solution.

the ssDNA-SAM probes (red circles) and chimeric DNA-VHH strands (blue squares), we substituted the buer solution with the one containing a known concentration (1 nM) of HER2. The binding of ECD-HER2-VHH by the active SAM is shown in Figure 6.2 (green triangles). To make sure about the specicity of ECD-HER2 biorecognition, we teste the system with Streptavidin. We regenerated the layer up to the ssDNA-SAM by means of a double-step cleaning protocol:the electrode was rinsed ve time with a solution of PBS 1x plus Tween at 0,05% in order to promote HER2-VHH detachment and then to a thermal treated (details in Section 2.5.1) to complete the regeneration process. ssDNA-SAM was again recovered (black curve in Figure 6.2) and a new hybridization (yellow markers) was performed with DNA+VHH conjugate at the same concentration (110 nM) of the previous experiment. Then a Streptavidin containing solution was inserted in the pool (violet points). In this case, we can observe a sudden drop of C_d, without any sign of biorecognition kinetics, as a demonstration that VHH-Streptvidin binding did not occure.

From Figure 6.2, we can see the C_d gap due to the steric hindrance carried by the involved proteins. In parallel, by applying the well-known 1^{st} order Langmuir adsorption kinetics (Equation 3.7) to the ECD-HER2 binding curve, we found a detection time of $\tau \approx (9.93 \pm 0.61)$ minutes with a C_d percentage change of $C_{d\%} \approx (13.18 \pm 1.46)$ %. Moreover, by tting the kinetics of hybridization of the chimeric cDNA-VHH protein onto the ssDNA-SAM we obtained $\tau_{VHH} \approx (3.65 \pm 0.23)$ minutes, to be compared with τ_{cDNA} ' (1.52±0.05) minutes found for a 100 nM DNA hybridization onto the same

ssDNA SAM (cf. Figure 3.5). The slower kinetics measured now is due to the presence of the mass of the nanobody which limits the mobility of the conjugated complementary strands, as widely explained and proven in Chapter 5.

Attested HER2 detection via VHH-A10 nanobody in saline buer (Figure 6.2), in a further step we tested our biosensor on the recognition of breast cancer marker HER2 from simulated patient's serum. We used a solution of Biseko Standardized Human Serum containing ECD-HER2 protein at dierent concentrations (0.1, 1, 10, 100 nM). Results of the biorecognition experiments run with two dierent AC applied voltages (75 and 100 mV) are shown in Figures 6.3 and 6.4.

Biseko Standardized Human Serum is a virus-inactivated human plasma serum that contains the entire spectrum of serum proteins in a standardized, active form [142] with a homemade estimated ionic strength of 157.3mM and purchased from Chong Lap Asia-Pacic Health Care Ltd.

Comparing Figures 6.3a) and 6.4a), we can get a further conrmation of eect of the potential on the measured value of C_s. In fact, rising the bias from 75 to 100 mV, it can be seen that the absolute capacitance at the working electrode increases.

In Figures 6.3b) and 6.4b) the average percentage change of C_s detected for both applied potentials, have been plotted versus ECD-HER2 concentration and the data have been analyzed with Hill equation tting in order to characterize the antigen-antibody binding. From the curves, an increase in eciency of the detection process can be further highlighted with a gain in sensitivity of about (10.97 ± 1.51)% with respect to the detection limit estimated in case of 75 mV applied voltage. The dissociation constant estimated is in the low nanomolar range for both cases: K_D ' (1.67 ± 0.81) nM applying an AC voltage of 75 mV in amplitude, and K_D ' (2.15 ± 0.97) nM with a 100 mV of bias. In conclusion, we can extend the device design to protein biomarker detection (ECD-HER2 vs VHH-A10), in a simulated human plasma environment, by exploiting DNA directed immobilization (DDI)[36] of DNA-protein conjugates and with an anity very closed to the values found using an SPR[141, 143]. The only precaution in this case will be to use small binders, as in-silico designed short peptides, aptamers or single domain antibodies, in order to match the dynamic polarization length of the device, which is around 7.3 nm at 100 mV of applied potential.

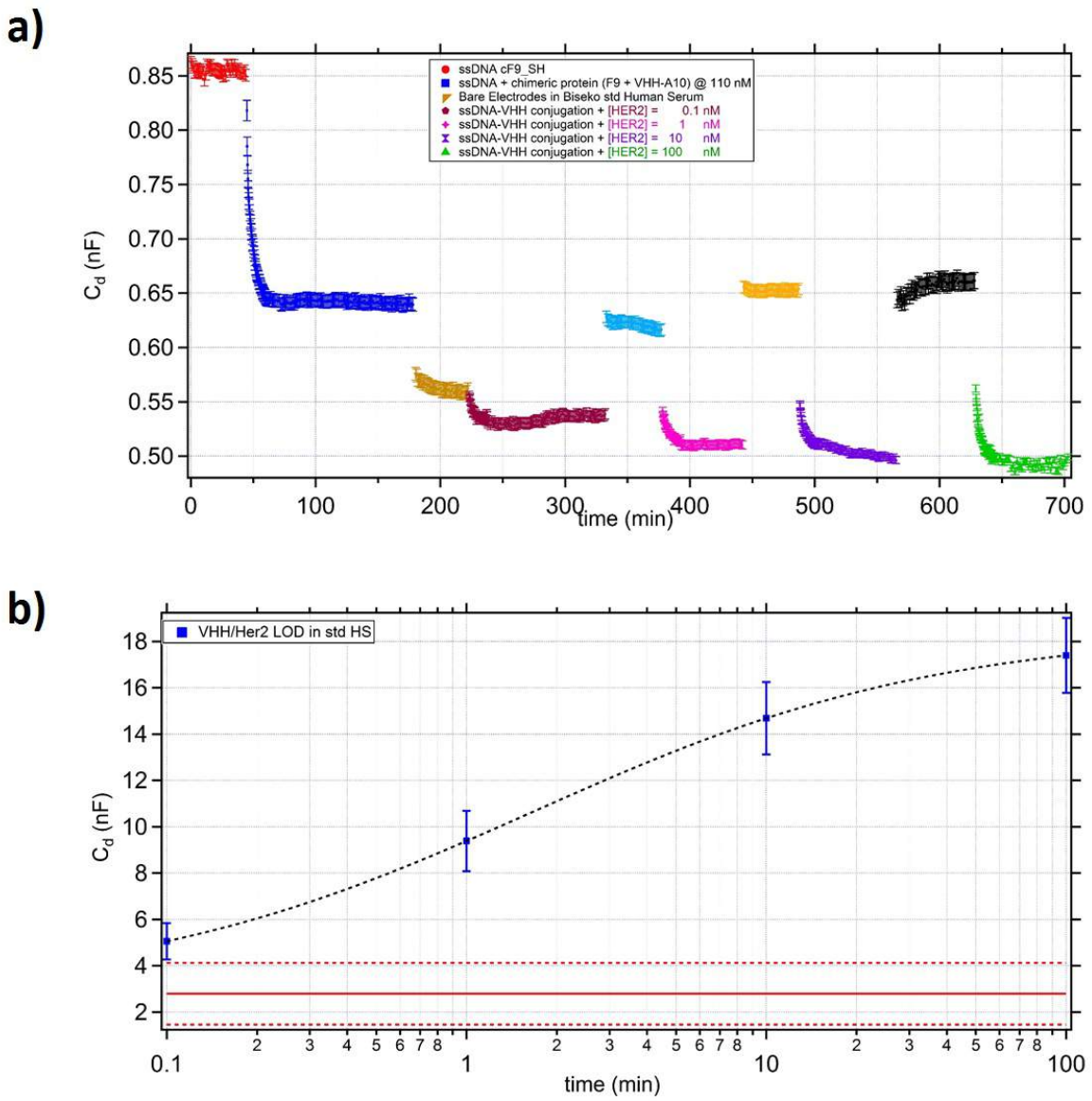

Figure 6.3: ECD-HER2 detection at 75 mV. a) ssDNA functionalized WE (red points) followed by 110 nM chimeric DNA-VHH hybridization estimated in PBS 1x (blue markers). VHH-A10-ECD-HER2 binding detection at dierent biomarker concentrations:100 pM (bordeaux signal); 1 nM (pink points); 10 nM (violet markers) and 100 nM (green triangles). Azure, orange and black points were measured in Biseko std. human serum after the regenerating protocol. The light brown markers represent the C_d measured at the WE soaked in a solution of pure Biseko std. human serum. b) Percentage change of C_d (blue squares) upon ECD-HER2 detection, as a function of [HER2] and tted with a Hill equation (dotted black curve). The solid red line represents the average variation of C_d due to aspecic detection, whereas the dashed red lines represent 3 standard deviations around this value.

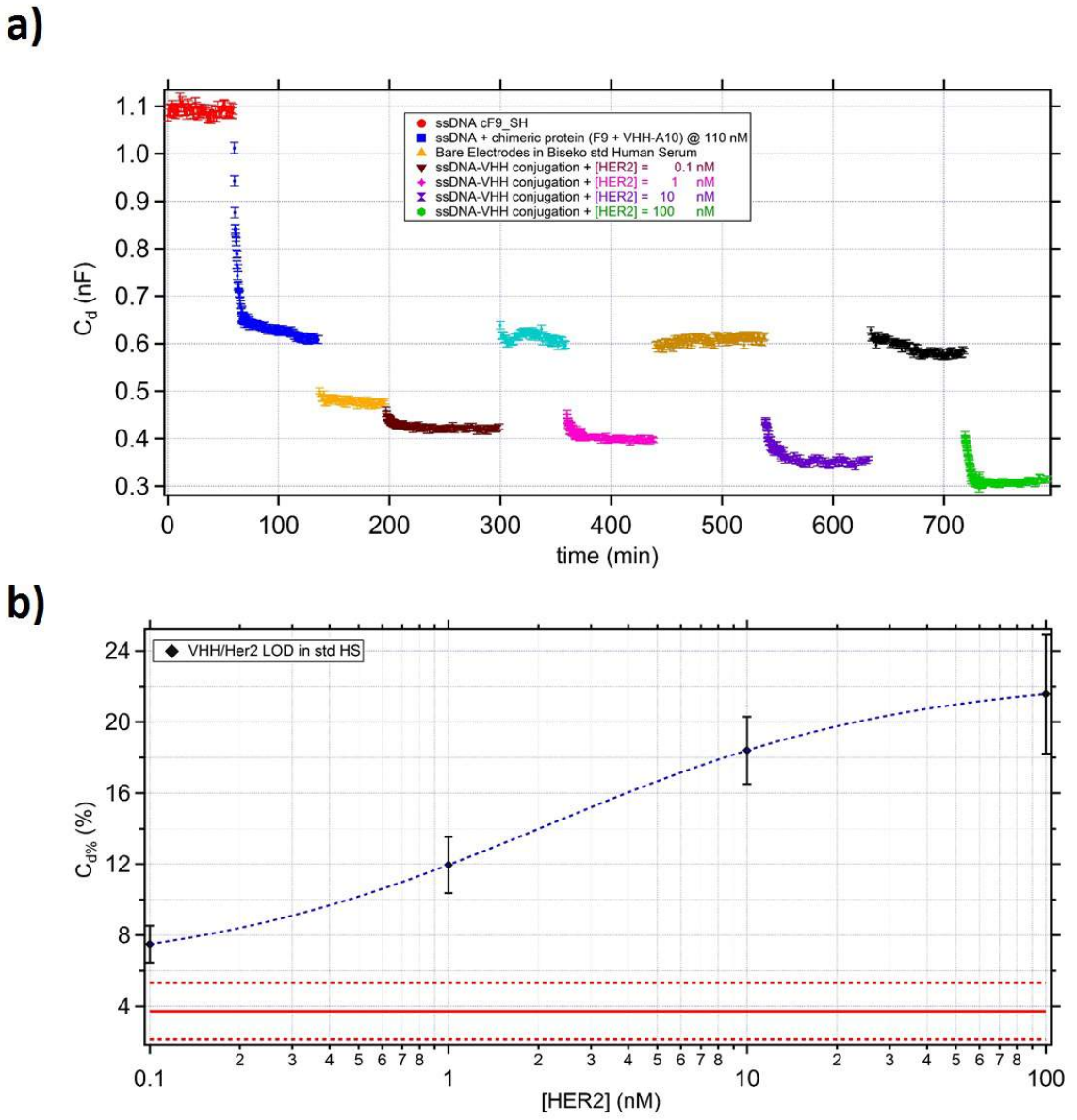

Figure 6.4: ECD-HER2 detection at 100 mV. a) ssDNA functionalized WE (red points) followed by 110 nM chimeric DNA-VHH hybridization estimated in PBS 1x (blue markers). VHH-A10-ECD-HER2 binding detection at dierent biomarker concentrations:100 pM (bordeaux signal); 1 nM (pink points); 10 nM (violet markers) and 100 nM (green triangles). Azure, orange and black points were measured in Biseko std. human serum after the regenerating protocol. The light brown markers represent the C_d measured at the WE soaked in a solution of pure Biseko std. human serum. b) Percentage change of C_d (black diamonds) upon ECD-HER2 detection, as a function of [HER2] and tted with a Hill equation (dotted blue curve). The solid red line represents the average variation of C_d due to aspecic detection, whereas the dashed red lines represent 3 standard deviations around this value.

Chapter 7

Conclusions

High sensitivity detection of circulating biomarkers as miRNAs and proteins relevant to specic disease is still challenging when it comes to real, complex matrices [144]. Biosamples as human plasma, serum, saliva, urine, etcontain an elevated numbers of proteins that can participate to signal generation (e.guorescence, charge distribution) hiding the signal coming from (few) specic biorecognition events. Here we proposed a miniaturized, label-free, electrochemical impedance spectroscopy based device with a careful optimization of the electrode surface functionalization, for the real-time, quantitative detection of double layer capacitance changes derived from the adsorption of molecules at the functionalized interface. Our device measures not only the steady-state, but also the biorecognition kinetics, easily discriminating the blocking eect of other biomolecules present in the matrix.In particular, we developed a three-electrodes sensor for the analysis of miRNAs relevant to specic diseases through the determination of the hybridization kinetics onto a cDNA probe monolayer self-assembled onto the working electrode. We demonstrated that: i) the device is reusable up to several times; ii) data are reproducible on dierent devices (standard deviation of only few percent); iii) the device has a low detection limit of 1 pM (improvable) in buer solution; iv) it can be used to quantify miRNAs in complex matrices, as human plasma, by using DNA/cDNA calibration curves. In the human samples tested so far,a miRNA concentration in the low nM (few nM) range was detected with results comparable with the ones estimated by the real time qPCR (qRT-PCR) used by MD Daniela Cesselli and her co-workers at University of Udine.

Very remarkably, the high sensitivity of our kinetics studies allows not only to quantify unknown concentrations of DNA/miRNA-target in solution, but in principle also to

discriminate dierent miRNAs families through the detection of single-base mismatches along the target sequence,as demonstrated for the case ofDNA/cDNA hybridization in buer solution [85]. In our case, we were able to clearly distinguish the presence of single, or multiple mismatches and also the position with respect to the gold surface of the missing basepairs.

Moreover, we proved to be able to easily extend the device design to protein biomarker detection ([145]) or therapeutic drug monitoring ([31]):by exploiting DNA directed immobilization (DDI) ([36]) of DNA-protein conjugates, we can in fact immobilize protein or drug binders on the surface, and then perform a biomarker/drug screening in complex matrices, similarly to what already described for miRNA analysis.The only precaution in this case will be to use small binders, as aptamers or single domain antibodies (e.g. VHH fragments), in order to match the dynamic polarization length of the device [61]. In particular, although these measurements are preliminary, we proved that:

- in a simulated human serum environment, VHH-A10-ECD-HER2 binding was detected through the incubation of chimeric DNA-protein SAM-probe assemblies attesting HER2 recognition with results comparable to a SPR-Biacore (K_{D-SPR} = 1.7 nM Vs K_{D-EIS} ' (1.9 ± 0.6) nM).

- in bulk, short oligo-labelled aptamer designed and optimized for thrombin recognition (aTHR) at low thrombin concentrations (<5 nM), the EIS sensor is more sensitive than a SPR-Biacore [146].

Being aware that further tests have to be performed in order to improve the signicance of these calibration curves,increasing the number of experimental points and making the relationships more consistent,these represent a very good and encouraging results both in terms of reproducibility of the device and, especially when compared to much more expensive instruments already on the market.

We are condent that our device, when opportunely combined with the available paper-based microuidics and integrated to perform multiplexing analysis of 5-10 dierent biomarkers in a biosample droplet, will constitute a sensitive, fast and cheap point-of-care device for medicaldiagnostics/prognosis and for the monitoring of the eect of a therapy from liquid biopsies, at the single patient level.

Chapter 8

Perspectives (3 Co-planar electrodes setup, AuNPs)

Detection of biomolecules at low concentrations is critically important to the early diagnosis and successful treatment of diseases. We have proved, along this work, that the detection sensitivity of a genosensor is determined by signal variation amplitude of a hybridization event. Therefore, increase the detection limit of our biosensor translates inevitably into an improvement in the sensor sensitivity in order to discern between smaller and smaller stimuli. In this regard, it was decided to move along two parallel tracks.

On one hand, we will try to improve the sensitivity of the device taking advantage to the amplication aorded by Au nanoparticles. Compared to the bare gold electrode, the gold nanoparticles modied electrode could improve the density of probe DNA attachment and the sensitivity of DNA biosensor greatly by avoiding however to increase the electrostatic and steric eects carried by a high probe density regime and thus render unnecessary all the assumptions made so far.

On the other hand, as already stated, the development of a multiplexing system is one of the main goal of our project and thus the miniaturization of the reference electrode on the same plane of the other two gold electrodes could bring great advantages in terms of portability of the device and of its Limit of Detection (LOD).

8.1 Gold Nanoparticles modied gold working electrode

Although dierent nanomaterials such as nanoparticles, nanowires and nanotubes are used for this purpose,we chose to work with gold nanoparticles in order to exploit the expertise of the group in the synthesis of DNA-conjugated gold nanoparticles.

In addition, nanoparticles represent an excellent biocompatibility with biomolecules and display unique structural, electronic, magnetic, optical and catalytic properties which have made them a very attractive material as labels in the detection of DNA hybridization. In addition, due to their low background capacitances these constructs have good potential in electrochemicalsensing with respect to the incorporation of an electrochemicallabel into the target molecule. The excess labels cause inconvenience, which is very time-consuming, and expensive and they would probably also aect the DNA recognition.

A huge variety of dierent (chemical or physical) methods has been employed for the synthesis of AuNPs, in this thesis, we referred to the protocol developed and improved by Deka and co-workers [147]to synthesize citrate stabilized AuNPs (cit@AuNPs) of approx. 20 nm sized by a known method of citrate reduction of $HAuCl_4$ [148] and further used for ssDNA functionalization in acidic conditions (pH = 4.3) in order to decrease the overall negative charge on the AuNP and ssDNA surfaces allowing to bring them closer and thereby ease the functionalization.

Anyway, the main topic of this session is not the synthesis of nanoparticles but the need to anchor the AuNPs to the working electrode surface. In fact, in our experimental conditions the application of an AC voltage could induce the nanoparticles to migrate on the surface and also to avoid creating hidden inhomogeneities in the conductive layer with areas covered by only thiolated ssDNA.

Generally, AuNPs modied electrode surfaces can be prepared in three major ways:

1. binding AuNPs with self-assembled monolayers (SAMs) containing dierent functional groups and sol-gel network[149, 150];
2. binding AuNPs by layer-by-layer assembly method[151, 152];
3. direct deposition of nanoparticles onto the bulk electrode surface by electrochemical and Langmuir Blodgett methods by modifying of the particles surface to render them hydrophobic and amenable to organization on the surface of water[153, 154].

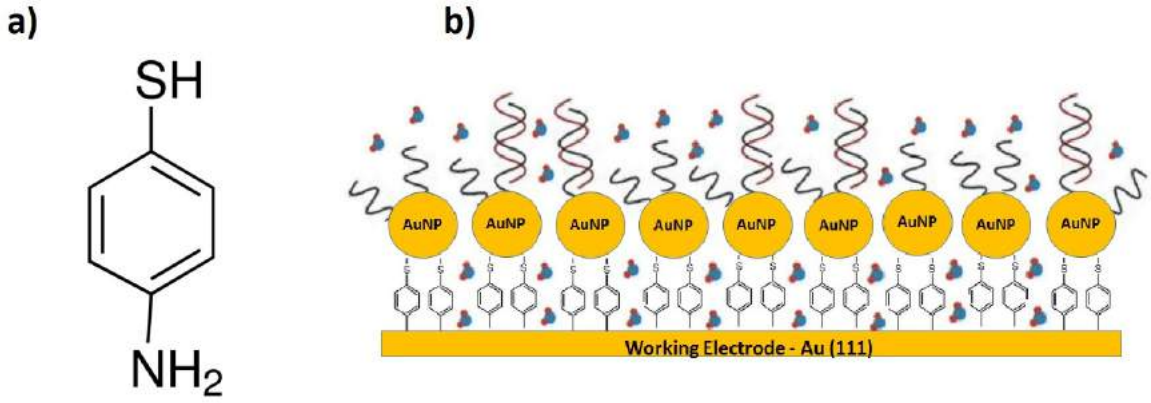

Figure 8.1: a) 4-Aminothiophenol Structural formula. b) schematic of the fabrication of Au/4-TP/AuNP/ssDNA+cDNA surface.

According to the literature, the simplest method of nanoparticles fabrication on electrode surface which gives some remarkable results is the so-called self-assembly method and again because in this way we have the chance to exploit the expertise of the group in the functionalization of gold surfaces and protein immobilization via DNA directed immobilization (DDI)[36, 37].

For fabricating AuNPs on electrode surface usually a bi-functional molecule (either a dithiol or a thiol and amine) is selected and resulting SAM will be in such a way that one thiol moiety will adsorb to the bulk Au surface and the other thiol, or amine moiety will protrude away from the surface. Then the modied electrode is immersed into a colloidal solution of AuNPs for a time period that can allow self-assembling on to the functionalized electrode due to nanoparticles strong anity towards mercapto or amine functionality.

In the end, we decided to use the bifunctional molecules 4-aminothiophenol (C_6H_7NS, MW = 125.19 g/mol, structural formula in Figure 8.1a)) for covalently binding AuNPs on electrode surfaces following the protocol described in [149]. In this work, Liu et al. passivate their polycrystalline gold electrodes through the electrochemical reduction in-situ of 4-TP diazonium salt by applying a potential to the electrode between 0.5V and =0.4V for two cycles. As outlined in the paper, instead of forming NH_2ArSAu bond on gold surfaces, the $HSArNH_2$ species, once converted to $HSArN_2^+$ is attached to the gold surface preferentially by the formation of a gold carbide bond, thus leaving a distal sulfhydryl groups free to bind to the AuNP soaking the electrode in AuNP solu-

tion for 3 h at room temperature. After this step, the AuNP immobilized gold surface (Au/4- TP/AuNP) is functionalized with thiolated ssDNA (see procedure in Section 2.5) and thus, our DNA-hybridization experiments can be performed as usual and an idealization of the so functionalized gold WE is shown in Figure 8.1b).

At this point we started to test whether, with our gold nanoparticles functionalized electrode surface, we are able to improve the DNA hybridization detection accelerating the kinetics. We have chosen to start with 2 nM for cDNA measuring the dierential capacitance at each functionalization step. The experimental results are summarized in Figure 8.2.

Figure 8.2a) shows C_d monitored at the bare working electrode and after the stepwise attachment of the thiolated molecule, AuNPs, ssDNA-SAM and the subsequent 2 nM cDNA-hybridization on gold surface. As can be seen, a stable C_d-signal was measured on bare gold electrode (red markers) while a capacitance reduction (blue squares) is detectable after that the 4-aminothiophenol surface functionalization has occurred. An increase in C_d can be observed (green points) after the incubation of Au/4-Tp surface with gold nanoparticles. This increase upon the attachment of the AuNPs is consistent with previous experiments which show that the nanoparticles can increase the electronic coupling to the underlying electrode[155]. After incubation of Au/4-TP/AuNPs modied surfaces with thiolated ssDNA, the C_d signal decreased slightly (yellow diamonds), showing the attachment of ssDNA on the nanoparticle by forming Au/4-TP/AuNP/ssDNA surface, and nally the hybridization curve (black hourglasses), shown several times during this work, revealed that the zippering mechanism among ssDNA probe layer and the 2 nM cDNA took place.

In Figure 8.2b), we compare the behavior of C_d, measured in KCl 100 mM and applying a 10 mV AC potential, as a function of the incubation time to the similar experiment shown in Figure 3.5 (blue markers) and performed at a concentration of 1nM of complementary DNA. We note here that passivating the electrode surface through AuNPs a reduction in the hybridization time (τ_{AuNp} ' 5.4±0.8 < τ ' 8.4±0.5 minutes) and thus a faster kinetics can be observed conrming the key role played by nanoparticles in improving the sensitivity of biosensors.

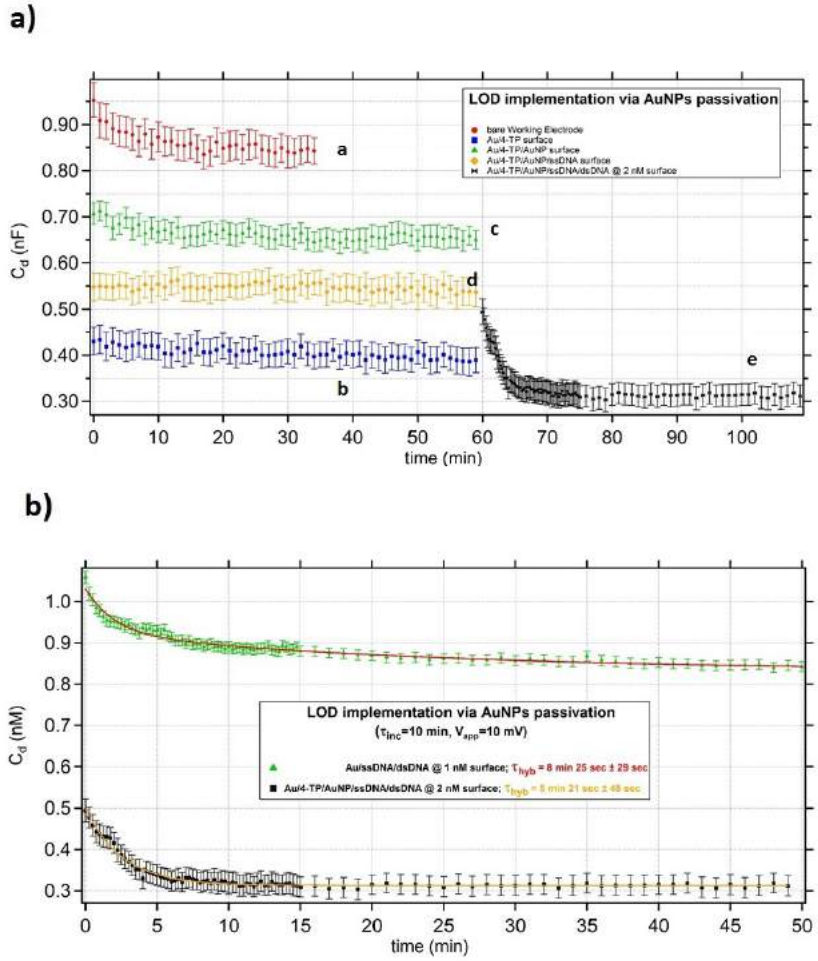

Figure 8.2: a) C_d signals recorded in 100 mM KCl buer solution after dierent steps modication: (a) bare Working Electrode; (b) Au/4-TP surface modication; (c) Au/4-TP/AuNPs surface; (d) Au/4-TP/AuNPs/ssDNA-SAM surface; Au/4-TP/AuNPs/ssDNA/2 nM dsDNA. b) Relative capacitance changes versus time for two dierent electrodes functionalization using the usual DNA/1nM cDNA hybridization process (green markers) and one example of DNA-hybridization via AuNPs passivation.

8.2 3 Co-planar electrodes setup as a possible implementation

Detecting several targets in the same biological sample is possible if dierent surface regions are functionalized with dierent probes. In addition, multiplexing is desirable

because it reduces the cost and sample volume per data point,satisfying some of the requirements of a point-of-care biosensor. For these reasons, as mentioned in the above section, multiplexing is one of the main goals of the project.

After the encouraging achievements in the detection of cancer biomarkers, which we obtained with the three-electrode conguration, we plan now to further upgrade the setup to allow for multiplexing and improving the biosensor LOD. The common denominator concerns the miniaturization of the reference electrode (RE) in order to move towards a three miniaturized coplanar electrodes conguration. As already stated, several reference electrodes can be used, for example, the saturated calomel electrode (SCE) is often employed in laboratory but, requiring a large amount of mercury, it is avoided in biosensor applications. The standard hydrogen electrode (SHE) is dicult to fabricate and miniaturize and thus, the solid state Ag/AgCl reference electrode (SSRE) is probably the best choice to be miniaturized and integrated on a chips, because of its electrochemical features (don't forget that the chloride ions are among the main serum electrolytes) and simplicity of fabrication using easy-to-handle chemicals useful to chlorinate, as bleach/sodium hypochlorite (NaOCl) or iron(III) chloride, also called ferric chloride ($FeCl_3$). The readers who are interested in learning the basic principles of the functioning and applicability of a microfabricated reference electrode will nd all the necessary details in [156].

A few methods are available that describe the miniaturization of the Ag/AgCl electrode on chip [156, 157, 158] but most of the Ag/AgCl electrodes have a vexing problem associated to its solubility product constant, $K_{sp} ' 1.8 \times 10^{-10}$, which implies, from a thermodynamic point of view, that about 2 mg of silver chloride can dissolve in a liter of water at room temperature, and thus it is characterized by a poor stability for many practical uses.Several methods have been proposed, we merely introduce the three most common procedure of improving RE stability.

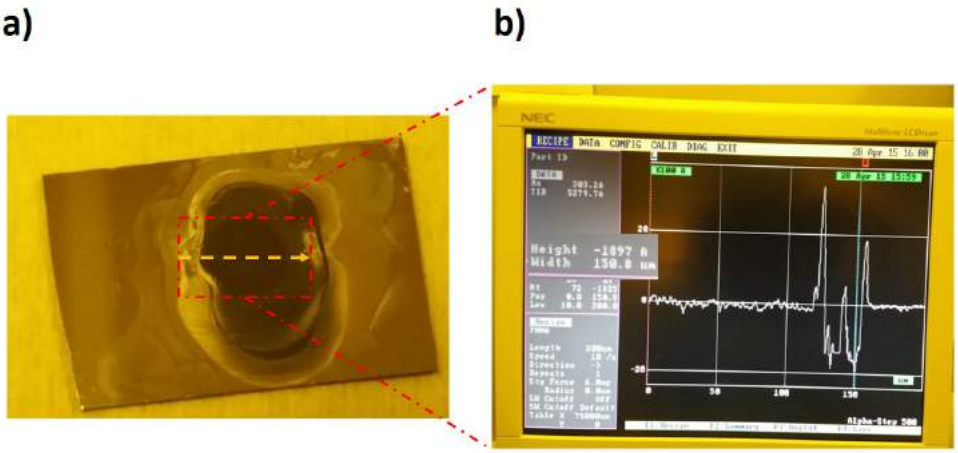

Figure 8.3: a) An half microscope slide coated by two metal layers, 20 nm of Titanium (adhesion layer) and 150 nm of Silver. Inside the red rectangle is evident a circular darker region of silver chloride obtained by exposing the slide to 50 mM $FeCl_3$ solution for 50 seconds. The orange dotted line marks the area scanned by a 3D surface prolometer whose results are shown in b) where the surface prole of the chlorinated area is displayed showing a thickness of 189.7 nm. The surface prole has been derived by using the Tencor AlphaStep 500 stylus-based surface proler available on the clean rooms of TASC - INFM National Laboratory, in Trieste, which also explains the yellow light in the pictures.

A rst solution consists in coating the silver chloride electrode with compound such graphene oxide [159] creating a diusion barrier to slow down the rate at which the silver chloride dissolves. Another procedure to improve AgCl stability is to evaporate a buer layer of Ni [160] between an adhesion layer of Ti and an Ag coat. The simplest last solution to this problem, which is the used method, is to increase the amount of silver chloride on the microelectrode surface through the silver anodization in chloride containing solutions, as NaOCl or $FeCl_3$. To achieve this goal we have moved on a two-pronged strategy, rst of all we have increased the amount of silver evaporated on the patterned slide (150 nm) and then we proceeded with its chlorination by immersing it in a solution of 50 mM ferric chloride for 50 seconds resulting in a 200 nm thick AgCl layer, as you can see in Figure 8.3.

Iron(III) chloride was chosen because of higher number of chloride ions per molecule (with respect to the mostly used bleach, NaOCl) reducing in this way the soaking time and the risk to damage the gold electrodes due to our co-planar conguration.

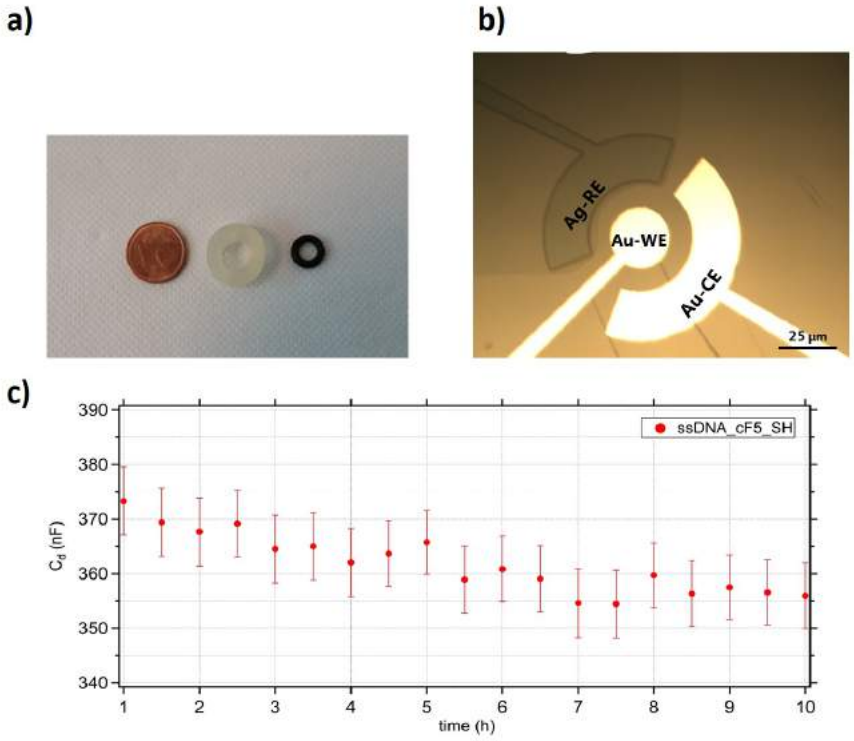

Figure 8.4: a) Comparison of the experimental pools for the old and new conguration. b) Zoom-in of the glass slide with microfabricated gold WE and CE and Ag/AgCl RE. c) Relative capacitance changes versus time for the three-coplanar electrodes conguration over a period of 10 hours.

The microfabrication of this three co-planar electrodes conguration has been made using a lithography procedure similar to the protocol described in Section 2.1., by using a new chrome photomask designed by myself and purchased by Dutch company Delta Mask B. V.. All the electrodes were fabricated by using microscope slides as substrate. Thin-lm metal electrodes were patterned onto the substrates via two dierent lift-o metallization protocols (cf. Table 2.2) using MEGAPOSIT ™ SPR™ 220 1.2 as a positive photoresist. Metals were deposited with e-beam evaporation. A 20 nm thick Ti layer was used to improve the adhesion on glass in both cases, and Au (80 nm) was evaporated as the top layer for the fabrication of Working and Counter electrodes, whereas Ag (150 nm) was employed for the RE. A top down photograph of the as-fabricated thin-lm electrode is shown in Figure 8.4b). From the red curve in Figure 8.4c), within nine hours, C_d changed by a maximum of (7.94 ± 0.04)% with respect to its initial value. This variation, albeit small, over time of the capacitance could

Experimental Pool features		
	old Conf.	New Conf.
Inner /[mm]	9.15	4.65
height /[mm]	7.2	1.45
Total Area /[cm ^{2}]	7.85×10^{-5}	1.96×10^{-5}
Sample volume requested /[µL]	125	25
Current Range appreciated /[µA]	1	0.001

Table 8.1: Comparison among the features of the old setup consisting of two micro-gold electrodes and a mm-sized AgCl pellet RE and the new 3 coplanar electrodes congura-tion.

be connected to a worsening of the SAM morphology probably because of too many lithography steps that created defects on the surface of the gold electrodes. The success rate (25% success) is really low for our standards (100% success in the fabrication of samples) but this protocol was chosen, among the procedures available in literature, for its simplicity but mainly because of my expertise.

Anyway, taken together, the largest amount of AgCl and the thicker silver layer allow a good stabilization of the Ag/AgCl microelectrode and, the reduction in the overall size of the electrolytic cell has resulted an increase of the device sensitivity as shown in Table 8.1 and as demonstrated in Figure 8.5.

From Figure 8.5, the absolute variations of Cd as a function of the functionalization layer of the electrodes are obviously linked to the smaller overall size of the new elec-trochemical cell (see Table 8.1 for details and Equation 2.2 for the model). It is also clear that we are able to detect 500 fM cDNA-hybridization with the new three-coplanar electrodes biosensor. In fact, in the rst hybridization process (red-blue curves in Figure 8.5) we estimated a variation of C_d between ssDNA and dsDNA of (4.86 ± 0.42)% and thus we cannot unambiguously state that this variation is connected to a biorecognition events, as already shown in Figure 3.6. The case of the new sensing device, we obtained a variation of the capacitance upon 500 fM cDNA-hybridization of (16.36 ± 2.76)%, is dierent. Further, an usual hybridization curves can be appreciated and a hybridization time of $\tau \approx (17.874 \pm 1.99)$ minutes was estimated, and then a great improvement can be highlighted especially when compared to the hybridization time derived for the other hybridization process (red-blue point in Figure 8.5), where a time of decay of about 125 minutes was calculated, even if we cannot actually talk about DNA-hybridization.

In a further step we plan to integrate the whole system into a microuidic channel,

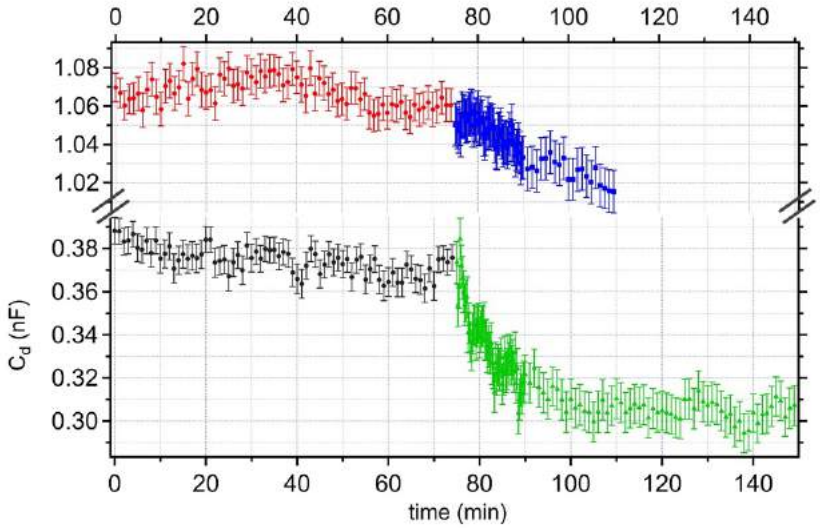

Figure 8.5: DNA/cDNA hybridization experiments were run with the two dierent setup congurations and performed in 100 mM KCl in 100 mM KCl saline buer at 10 mV applied AC potential. The ssDNA probe density (incubation time of 10 minutes) is the same in both cases as wellas the concentration (500 fM) of the complementary DNA strands. Red and black markers describe the dierential capacitance at the ssDNA functionalized WE measured with the old three-electrode setup and with the new three-coplanar electrodes conguration, respectively. The blue squares show the C_d-changes upon 500 fM cDNA-hybridization obtained with the classical biosensing setup, the green triangles instead displayed the variation in capacitance estimated with the new three-coplanar electrodes at the same cDNA concentration.

an idealization of our ideas is shown in Figure 8.6. In order to do it we will appeal to a OSTE [1] microuidic system which is an emerging trend in the bioengineering eld due to their ability to maintain rapid, sensitive and specic attributes of microuidic devices.There are several advantages [161] with respect to the commonly used PDMS, in fact with this technique we can pattern on a OSTE-coated microscope slide and thus have a microuidic system with desired characteristics (sizes, shape,etc. . .) and adaptable to unexpected future needs. Another great advantage is that it is hydrophilic and so we can dene areas of hydrophilic paper separated by hydrophobic walls enabling the transport of uids, without pumping, due to capillary action and thus providing a spatial control of biological uids.

Using the explained setup,we are relatively sure to produce a microuidic channel

[1] is a novel polymer platform comprising O-Stoichiometry Thiol-Enes (OSTE)

with incorporated electrodes with a height, ≈ 7 µm, which can and must be further reduced especially in the case of multiplexing system. The problem with this device would be the targeted functionalization of the dierent WEs. For this aim we plan to use the so-called low-voltage electrowetting microvalves [162], that concerns the interfacial surface tension of solid-liquid by the applied electric potential between a conductive droplet and insulated underlying electrodes. According to our idea, each valve should contain two inkjet-printed silver electrodes in series. Capillary ow within the main microchannelcan be stopped at the entrance of a secondaryµchannelequipped with an electrode modied with a hydrophobic monolayer (e.gOTS, n-octadecyl-trichlorosilane, $C_{18}H_{37}SiCl_3$) (valve closed). When a potential was applied across the electrodes, the hydrophobic monolayer became hydrophilic and allowed ow to continue (valve opened). Increasing the distance between two electrodes we need to increase the applied voltages. Additionally, the actuation time required to open the valve increased when voltage was decreased.

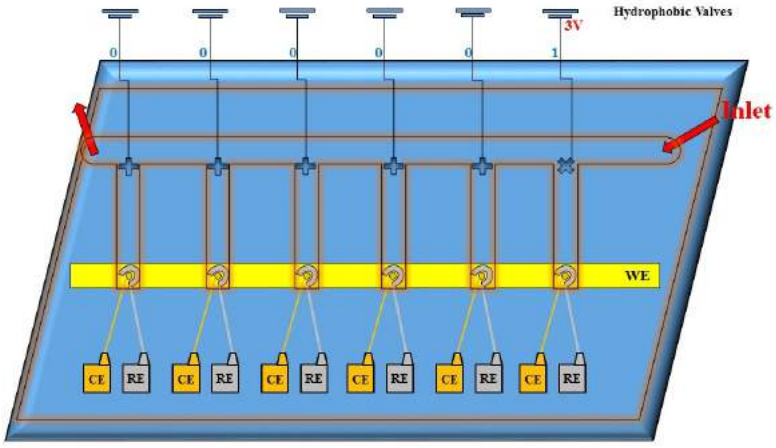

Figure 8.6: a) b) Idealization of how it should be a multiplexing system based on our three-coplanar electrodes as sensing unit.

Following this idea, we plan to create up to six parallel microchannels using soft lithography (see Figure 8.6), ux within them up to six dierent solutions containing up to six dierent thiolated DNA sequences by opening and closing valves hydrophobic and thus perform the detection inside the microchannel.

Appendices

A - Discussion about Langmuir 1 st-order kinetics

[cDNA]	Fitting Parameters	1st order Langmuir Kinetics	Double Exponential Kinetics
[1pM]	C_{dsDNA}	(0.941±0.001)nF	(0.93±0.01) nF
	k_1	(0.07±0.01) min^{-1}	
	τ	(15.4±1.4) min	
	τ_{hyb}		(11.36 ± 0.97)min
	τ_{melt}		(47.7 ± 5.1) min
	χ^2_v	0.62	0.93
[10pM]	C_{dsDNA}	(0.918±0.001)nF	(0.915±0.001)nF
	k_1	(0.08±0.01) min^{-1}	
	τ	(13.1±0.8) min	
	τ_{hyb}		(8.4 ± 0.08) min
	τ_{melt}		(45.1 ± 3.9) min
	χ^2_v	0.7	0.9
[100pM]	C_{dsDNA}	(0.869±0.001)nF	(0.867±0.001)nF
	k_1	(0.09±0.01) min^{-1}	
	τ	(11.6±1.2) min	
	τ_{hyb}		(7.2 ± 0.7) min
	τ_{melt}		(50.3 ± 7.3) min
	χ^2_v	0.93	0.9

Table 2:

[cDNA]	Fitting Parameters	1st order Langmuir Kinetics	Double Exponential Kinetics
[1nM]	C_{dsDNA}	(0.845±0.002)nF	(0.86±0.02) nF
	k_1	(0.12±0.01) min^{-1}	
	τ	(8.4±0.5) min	
	τ_{hyb}		(5.2 ± 0.8) min
	τ_{melt}		(44.0 ± 6.1) min
	χ^2_v	0.68	0.81
[10nM]	C_{dsDNA}	(0.707±0.001)nF	(0.67±0.02) nF
	k_1	(0.27±0.01) min^{-1}	
	τ	(3.7±0.8) min	
	τ_{hyb}		(2.5 ± 0.08) min
	τ_{melt}		(50.1 ± 5.2) min
	χ^2_v	1.58	1.15
[100nM]	C_{dsDNA}	(0.632±0.001)nF	(0.59±0.04) nF
	k_1	(0.65±0.02) min^{-1}	
	τ	(1.52±0.05) min	
	τ_{hyb}		(1.47 ± 0.05)min
	τ_{melt}		(46.1 ± 4.1) min
	χ^2_v	1.34	1.03

Table 3: Fitting parameters for DNA/DNA hybridization C_d-proles shown in Figure 3.5 obtained using the 1st order Langmuir adsorption kinetics and double exponential model, respectively.From the χ^2_v-values, it can be said that our experimental curves are best t by the double exponential model since, in this way, we take into account the two dierent mechanism that concur in the oligonucleotide hybridization process.

B - Clausius Mossotti factor

As stated in Chapter 4, at microscopic scale,a non-uniform electric eld, induces the movement of dielectrically polarized particles. The acting force on a spherical particle of radius a, of complex dielectric permittivity $\tilde{}_p$, suspended in a medium of relative permittivity $_m$, is given by Equation 4.12, which is here reported again:

$$\vec{F}_{DEP} = 2\pi a^3 \, _m \cdot \mathrm{Re}\{K(\omega)\} \nabla |E_0|^2 \qquad (1)$$

in this equation, $\nabla |E_0|^2$ is the gradient of the square of the electric eld, E_0 being the root mean square amplitude of the applied eld and $\mathrm{Re}\{K(\omega)\}$, is the real component of the complex ClausiusMossotti (CM) factor dened as:

$$K(\omega) = \frac{\tilde{\varepsilon}_p - 2\tilde{\varepsilon}_m}{\tilde{\varepsilon}_p + 2\tilde{\varepsilon}_m} \quad (2)$$

where $\omega = 2\pi f$ is the angular frequency of the applied field (with f that is the frequency of the field); $\tilde{\varepsilon} = \varepsilon' - i\,\varepsilon''$ is the complex dielectric permittivity and ε' and ε'' are the real and imaginary components of the complex dielectric permittivity, which may be written in the Debye form[163]:

$$\varepsilon' = \varepsilon_\infty + \frac{\varepsilon(0) - \varepsilon_\infty}{1 + \omega^2\tau^2} \quad (3)$$

$$\varepsilon'' = \frac{\sigma}{\omega\varepsilon_0} + \frac{[\varepsilon(0) - \varepsilon_\infty]\,\omega\tau}{1 + \omega^2\tau^2} \quad (4)$$

where σ is the electric conductivity of the particle or medium and τ is the relaxation time. From the Debye theory [163], the relaxation time is correlated to the frequency f_{max}, at which ε'' has a maximum, by the relation $2\pi\tau \cdot f_{max} = 1$. Moreover, $\varepsilon(0)$ is the permittivity at frequencies much smaller than f_{max} and ε_∞ is the permittivity at frequencies much larger than f_{max} [164]. By introducing in Equation 2 the complex form of dielectric permittivity of particle and of medium, we can calculate the real, $\mathrm{Re}\{K(\omega)\}$, and imaginary, $\mathrm{Im}\{K(\omega)\}$, components, of the Clausius-Mossotti factor resulting in the following relationships:

$$\mathrm{Re}\{K(\omega)\} = \frac{\varepsilon_p'^2 + \varepsilon_p''^2 + \varepsilon_p'\varepsilon_m' - 2\varepsilon_m'^2 + \varepsilon_m''^2 - \varepsilon_p''\varepsilon_m'' - 2\varepsilon_m''^2}{\varepsilon_p'^2 + \varepsilon_p''^2 + 4\varepsilon_p'\varepsilon_m' + 4\varepsilon_m'^2 + 4\varepsilon_m''^2 - 2\varepsilon_p''\varepsilon_m'' + \varepsilon_m''^2} \quad (5)$$

$$\mathrm{Im}\{K(\omega)\} = \frac{3\varepsilon_p''\varepsilon_m' - 3\varepsilon_p'\varepsilon_m''}{\varepsilon_p'^2 + \varepsilon_p''^2 + 4\varepsilon_p'\varepsilon_m' + 4\varepsilon_m'^2 + 4\varepsilon_m''^2 - 2\varepsilon_p''\varepsilon_m'' + \varepsilon_m''^2} \quad (6)$$

From Equations 5 and 6 we can observe that the real and imaginary components of the Clausius-Mossotti factor, depend on the dielectric properties of the particle and medium, and on the frequency of the applied field which determines the dependence in frequency of the DEP force.

The measurements of the complex dielectric permittivity were performed using a DSO Lock-In Amplifier: Model SR830 by Stanford Research Systems 7a). An AC voltage with frequency ranging from 5 Hz to 5 kHz and a root mean square (rms) amplitude of 10 mV was applied across the electrodes and the current flowing in the experimental pool was amplified with a transresistance amplifier, Femto DLPCA 200 7b). In order

Figure 7: a) Front view of the lock-in amplier, model SR830 by Stanford Research Systems. The tool can be used in the output frequency and voltage ranges ranging from 1 mHz to 102 kHz and from 4mV to 5V (error 1%), respectively. b) Picture of the trans-resistance amplier DLPCA 200 by Femto. The amplier can be used both for DC and AC current-signal and the amplication factor can be tuned in a very broad range, from 10^3 to 10^{11} V/A.

to automatize the scans we wrote a procedure using LabView, a software powered by National Instruments.

The experiments were carried out exploring the dynamic range of [cDNA] over 6 orders of magnitudes, from 1 pM to 100 nM. For each concentration we left the solution in contact with the WE for 1.5 h and then we measured the dierential capacitance and the quality factor in the presence of the cDNA (C^f_{WE} , Q^f_{WE}) as well as in its absence (C^i_{WE} , Q^i_{WE}), over the working frequency range. The real and imaginary components (^{0} and ^{00}) of the complex dielectric permittivity were determined using the following relations[165], using the same notation adopted in Chapter 4.1:

$$^0 = \frac{C^f_{WE}}{C^i_{WE}} \tag{7}$$

$$^{00} = \frac{Q^i_{WE} \cdot C^f_{WE} - Q^f_{WE} \cdot C^i_{WE}}{Q^f_{WE} \cdot Q^i_{WE} \cdot C^i_{WE}} \tag{8}$$

The experimental frequency dependence of the real and imaginary components of the complex dielectric permittivity of the investigated dsDNA-SAM, for dierent concentration of the cDNA ([cDNA]), are presented in Figure :

Figure 8: The frequency dependence of the measured a) real$_{;}^{0}$, and b) imaginary, $_{;}^{00}$, components ofthe complex dielectric permittivity, of the sample for dierent value of [cDNA] hybridized with a 15 minutes ssDNA-SAM probe adsorbed on the gold surface of the WE.

C - Aptamer-based assays for protein detection

As widely expounded, the rapid and reliable detection of multiple biomarkers simultaneously in small sample volumes is increasingly requested in current clinical practice and a promising strategy for multiplexing probe immobilization is DDI (DNA Directed immobilization) where dierent DNA-conjugated antibodies are employed for detecting dierent biomarkers. However, the synthesis of chimeric conjugates is quite challenging, demanding a careful engineering to ensure a nal construct that has not lost its original anity.

From this point of view, a valid alternative to antibodies is represented by nucleic acid aptamers that are oligosequences selected in vitro to bind a target with high anity, highly reproducible and reduced cost production since the DNA-aptamer construct is produced simply by adding the surface binding sequence to the aptamer during oligosynthesis.

As a proof of principle, in this study we used an extensively investigated a 15-mer aptamer (aTHR) which is selective for the brinogen binding site of the human α-thrombin[166] and that shows a well characterized structure and binding properties (K_D = 50 nM), conrmed by several studies[167, 168].

The DNA-aptamer construct, named cF9-aTHR, was prepared adding the sequence complementary to the F9-thiolated linker ($HS-(CH_2)_6$-5'-ctt cac gat tgc cac ttt cca c-3', F9_SH) to the 3' aptamer (5'-ggt tgg tgt ggt tgg-3') end. To run the assay the aptamer construct was rst activated. In order to do it, the construct prepared as 10 µM solution in the binding buer (20mM Tris pH7.4, 140mM NaCl, 5mM KCl, 1mMMgCl2, 1mMCaCl2, named THR buer) was rst denaturated for 10 min at 95°C, cooled immediately on crushed ice for 10 min and left at room temperature for 15 min to restore their functional conformation. All the reagents in the binding experiment including buers, human thrombin and synthesis of aptamer construct were ordered from Sigma-Aldrich.

To functionalize the Working Electrode with ssDNA-molecules, we used the well-

known procedure described in Section 2.5 wetting the gold electrode with a drop of TE NaCl 1 M, containing cF9_SH at 1 µM in order to have a Langmuir-like kinetics regime. In addition, the dierential capacitance at the WE was measured tting the current response upon the application of an AC voltage with amplitude of 10 mV. The hybridization of the ssDNA-SAM was performed with the aptamer construct cF9-aTHR at 1 µM in a solution containing 100 mM KCl, whereas the antigen detection experiments have been carried out using the THR buer that folds the aptamer in the functional conformation for the recognition of the humanα-thrombin at three dierent concentration: 4, 10 and 40 nM.

From Figure 9a), attested the stability of the dierential capacitance at the ssDNA functionalized WE (red points) and the successful DNA-aptamer SAM-covered electrode hybridization (blue markers) in 100 mM KCl buer solution, we challenged the device for thrombin detection. First of all, we changed the buer solution with the one for THR, which contains divalent ions, in order to promote the formation of the secondary fold of the DNA aptamer. The capacitance-change kinetics measured in-situ upon changing of the buer solution (Figure 9a), cyan diamonds) has to be attributed to the electrode interface rearrangement due to the conformational reorganization of the nucleic acids upon the interaction with the divalent salt solution. At this point, we monitored the capacitance variation upon the binding of 4 nM THR (green triangles). A three rinse cycle in THR buer was carried out in order to test the stability of the DNA aptamer - THR binding which, as can be seen (grey markers), appears to be suciently stable. After an overnight regeneration procedure, consisting in soaking the device in a 2M NaCl solution, we tested again the stability of the aptamer functionalized electrode (gold and pink points) and then we incubated the sensor with two solutions with a 10 nM and a 40 nM thrombin concentration (blue down-oriented and orange left-oriented triangles, respectively), interspersed with a 30 minutes binding denaturation process in 2M NaCl (black markers).

In conclusion, the percentage change of f_0 was estimated on all three concentrations (4, 10 and 40 nM) and the results, in very good agreement with SPR data (Figure 9b)[146]), are listened in Table 9:

However, although these measurements are preliminary, we observed that at low thrombin concentrations ($\lesssim$ 5 nM), the EIS sensor is more sensitive than SPR, and that could be pushed to reach lower detection limits (in the pM range, as we expected from literature).

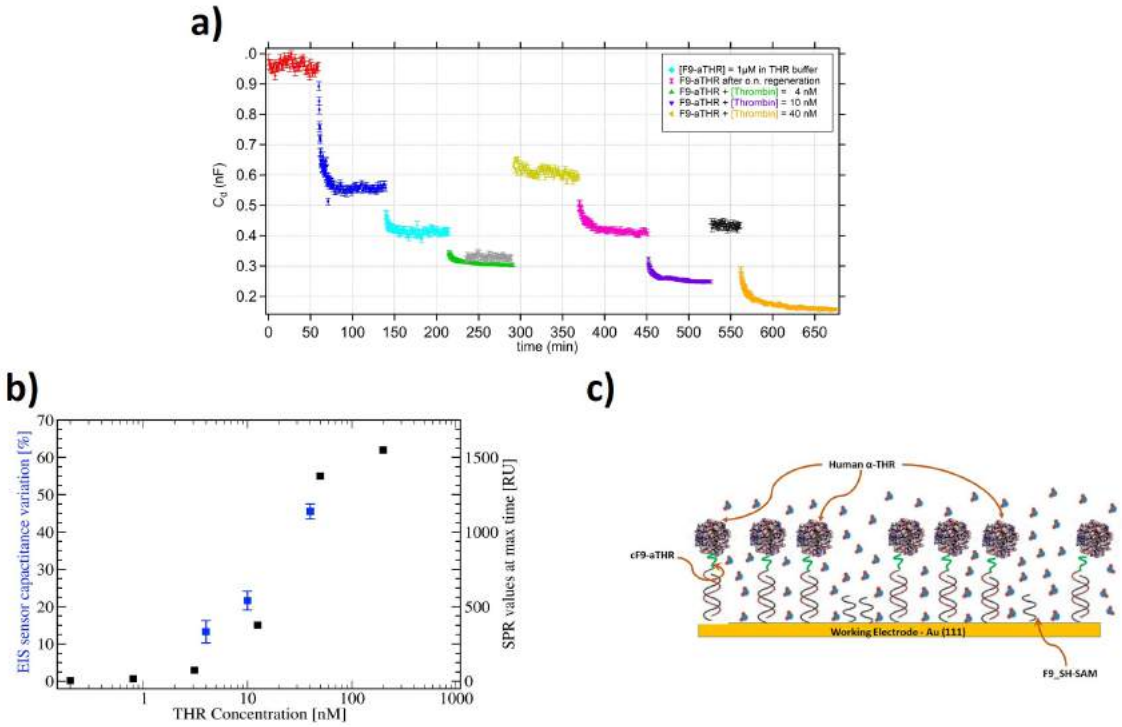

Figure 9: a) Dierential capacitance measured in-situ upon DNA-Aptamer construct (F9-aTHR) - human α− thrombin at dierent THR concentration (4, 10 and 40 nM). b) C_d percentage changes, $C_{d\%}$ (blue point) compared with the binding anity analysis performed on surface immobilized aptamers via Surface Plasmon Resonance (black markers). Picture from [159]. c) Cartoon of the DNA-aptamer SAM-covered electrode after incubation with human α-thrombin.

[THR]/[nM]	$C_{d\%}$/[%]	τ/[min]
4	(12.8 ± 2.6)	(11.5 ± 1.6)
10	(22.2 ± 4.1)	(8.1 ± 0.3)
40	(45.8 ± 6.7)	(5.2 ± 0.3)

Table 4: C_d percentage change and hybridization time, via Langmuir adsorption kinetics, upon DNA-Aptamer construct - human thrombin recognition, as a function of [THR].

D - Oligonucleotide Sequences and Nomenclature

Sequence Name	Length	Sequence
F5-SH	22-mer	HS-$(CH_2)_6$-5'-ctt atc gct tta tga ccg gac c-3'
cF5	22-mer	5'-ggt ccg gtc ata aag cga taa g-3'
F9-SH	22-mer	HS-$(CH_2)_6$-5'-ctt cac gat tgc cac ttt cca c-3'
F9/F9-maleimid	22-mer	5'-gtg gaa agt ggc aat cgt gaa g-3'
aTHR	15-mer	5'-ggt tgg tgt ggt tgg-3'
pDNA1	25-mer	HS-$(CH_2)_6$-5'-tga taa tca tta taa aac tga aat a-3'
cDNA1	25-mer	5'-tat ttc agt ttt ata atg att atc a-3'
1MM_DNA1	25-mer	5'-tat ttc agt ttt Gta atg att atc a-3'
pDNA2	44-mer	HS-$(CH_2)_6$-5'-caa aac agc agc aat cca aag atc aga cac ccg att aca aat gc-3'
cDNA2	44-mer	5'-gca ttt gta atc ggg tgt ctg atc ttt gga ttg ctg ctg ttt tg-3'
2MM_DNA2	44-mer	5'-gca ttt gta atc ggg tgt cGg atc Ctt gga ttg ctg ctg ttt tg-3'
3MM_DNA2	44-mer	5'-Tca ttt gta atc ggg tgt cGg atc Ctt gga ttg ctg ctg ttt tg-3'
cDNA2_UP	22-mer	5'-gca ttt gta atc ggg tgt ctg a-3'
cDNA2_DOWN	22-mer	5'-tct ttg gat tgc tgc tgt ttt g-3'
hsa-miR-154-5p-comp-SH	22-mer	HS-$(CH_2)_6$-5'-cga agg caa cac gga taa cct a-3'
hsa-miR-154-5p (RNA)	22-mer	5'-uag guu auc cgu guu gcc uuc g -3'
mmu-miR-351-5p-comp-SH	24-mer	HS-$(CH_2)_6$-5'-cag gct caa agg gct cct cag gga-3'
mmu-miR-351-5p (RNA)	24-mer	5'-ucc cug agg agc ccu uug agc cug-3'

Figure 10: List of oligonucleotides sequences used for the EIS experiements.

Bibliography

[1] Tsouti, V.; Boutopoulos, C.; Zergioti, I.; Chatzandroulis, S. Capacitive microsystems for biological sensing. Biosensors and Bioelectronics, 2011, 27(1):111.

[2] Beyette, F. R.; Kost, G. J.; Gaydos C. A.; Weigl B. H. Point-of-care technologies for health care, IEEE Trans. Biomedical Engineering, 2011, 58(3), 732-735.

[3] Neuºil, P.; Giselbrecht, S.; Länge, K.; Huang, T. J.; Manz, A. Revisiting lab-on-a-chip technology for drug discovery. Nat. Rev. Drug. Discov., 2012, 11, 620632.

[4] Chin, C.D.; Linder, V.; Sia, S.K. Commercialization of microuidic point-of-care diagnostic devices. Lab. Chip., 2012 12, 21182134.

[5] Kumar, S.; Kumar, S.; Ali, M.A.; Anand, P.; Agrawal, V.V.; John, R.; Maji, S.; Malhotra, B.D. Microuidic-integrated biosensors: prospects for point-of-care diagnostics. Biotechnol. J., 2013, 8(11), 1267-79.

[6] Ferrario, C.M.; Flack, J.M.; Strobeck, J.E. Individualizing hypertension treatment with impedance cardiography: a meta-analysis of published trials. Ther. Adv. Cardiovasc. Dis., 2010, 4, 5-16.

[7] Wijaya, E.; Lenaerts, C.; Maricot, S.; Hastanin, J.; Habraken, S.; Vilcot, J.P.; Boukherroub, R.; Szunerits, S. Surface plasmon resonance-based biosensors: From the development of dierent SPR structures to novel surface functionalization strategies. Curr. Opin. Solid St. M., 2011, 15, 208-224.

[8] Ferrari, L.; ipovà, H.; Tichy, I.; Chadt, K.; Homola, J. Electrochemical surface plasmon resonance biosensor for study of DNA desorption and hybridization. Optical Sensors, 2013, Proc. of SPIE Vol.8774, 87740F-1.

[9] Nguyen, H.H.; Park, J.; Kang, S.; Kim, M. Surface Plasmon Resonance: A versatile technique for Biosensor Applications. Sensors, 2015, 15, 10481-510.

[10] Liu, Y.; Liu, Q.; Chen, S.; Cheng, S.; Wang, H.; Peng, W. Surface Plasmon Resonance Biosensor based on smart phone platforms. Scientic Reports, 2015, 5, 12864.

[11] Abell, J.L.; Garren, J.M.; Driskell, J.D.; Tripp, R.A.; Zhao, Y. Label-Free Detection of Micro-RNA Hybridization Using Surface-Enhanced Raman Spectroscopy and Least-Squares Analysis. J. Am. Chem. Soc., 2012, 134, 12889-12892.

[12] Toma, A.; Das, G.; Chirumamilla, M.; Saeed,A.; Proietti, Z. R.; Razzari, L.; Leoncini, M.; Liberale, C.; De Angelis, F; Di Fabrizio, E. Fabrication and characterization of a nanoantenna-based Raman device for ultrasensitive spectroscopic applications. Microelectron. Eng., 2012, 98, 424-427.

[13] Citartan, M.; Gopinath, S.C.; Tominaga, J.; Tang, T.H. Label-free methods of reporting biomolecular interactions by optical biosensors. Analyst., 2013, 138(13), 35763592.

[14] Zhang, Z.; Lin, M.; Zhang, S.; Vardhanabhuti, B. Detection of aatoxin m1 in milk by dynamic light scattering coupled with superparamagnetic beads and gold nanoprobes. J. Agr. Food Chem., 2013, 61(19), 4520-4525.

[15] Arlett, J.L.; Myers, E.B.; Roukes, M.L. Comparative advantages of mechanical biosensors. Nat. Nanotechnol., 2011, 6(4):203215.

[16] Melli, M.; Scoles,G.; Lazzarino, M. Fast detection of biomolecules in diusion-limited regime using micromechanical pillars. ACS nano, 2011, 5(10):7928e35.

[17] Holford, T.R.J.; Davis, F.; Higson, S.P.J. Recent trends in antibody based sensors. Biosens. & bioelectron., 2012,34(1), 12-24.

[18] Tamayo, J.; Kosaka, P.M.; Ruz J.J.; San Paulo, A.; Calleja, M. Biosensors based on nanomechanical systems. Chem. Soc. Rev., 2013, 42(3), 12871311.

[19] Kosaka, P.M.; Pini, V.; Ruz, J.J.; da Silva, R.A.; Gonzalez, M.U.; Ramos, D.; Calleja, M.; Tamayo, J.; Detection of cancer biomarkers in serum using a hybrid

mechanical and optoplasmonic nanosensor. Nat. Nanotechnol., 2014, 9, 1047-1053.

[20] Mao, X.; Huang, T.J. Microuidic diagnostics for the developing world. Lab. chip., 2012, 12, 1412-6.

[21] Hong, J.; Yoon, D.S.; Kim, S.K.; Kim, T.S.; Kim, S.; Pak, E.Y.; No, K. AC frequency characteristics of coplanar impedance sensors as design parameters. Lab. chip, 2005, 5(3), 270279.

[22] Daniels, J.S.; Pourmand, N. Label-Free Impedance Biosensors: Opportunities and Challenges. Electroanalysis, 2007, 19(12), 12391257.

[23] Karnik, R.; Duan, C.; Castelino, K.; Daiguji, H.; Majumdar, A. Rectication of ionic current in a nanouidic diode. Nano letters, 2007, 7(3), 54751.

[24] Durand, N.F.Y.; Renaud, P. Label-free determination of protein-surface interaction kinetics by ionic conductance inside a nanochannel. Lab on a chip, 2009, 9(2),31924.

[24-1] Daniels, J.S.; Nader Pourmanda, N. Label-Free Impedance Biosensors: Opportunities and Challenges. Electroanal., 2007, 19(12), 1239-1257.

[25] Limbut, W.; Hedström, M.; Thavarungkul, P.; Kanatharana, P.; Mattiasson, B.; Capacitive biosensor for detection of endotoxin. Anal. Bioanal. Chem., 2007, 389, 517525.

[26] Qureshi, A.; Niazi, J.H.; Kallempudi, S.; Gurbuz, Y. Label-free capacitive biosensor for sensitive detection of multiple biomarkers using gold interdigitated capacitor arrays. Biosens. Bioelectron, 2010, 25, 2318-2323.

[27] Tosar, J.P.; Branas, G.; Laíz, J. Electrochemical DNA hybridization sensors applied to real and complex biological samples. Biosens. Bioelectron., 2010, 26, 12051217.

[28] Numnuam, A.; Kanatharana, P.; Mattiasson, B.; Asawatreratanakul, P.; Wongkittisuksa, B.; Limsakul, C.; Thavarungkul, P. Capacitive biosensor for quantication of trace amounts of DNA Biosens. Bioelectron., 2009, 24, 25592565.

[29] Ianeselli, L.; Grenci, G.; Callegari, C.; Tormen, M.; Casalis, L. Development of stable and reproducible biosensors based on electrochemical impedance spectroscopy: Three-electrode versus two-electrode setup. Biosens. Bioelectr., 2014, 55, 16.

[30] Zou, Z.; Kai, J.; Rust, M.J.; Han, J.; Ahn, C.H.; Functionalized nano interdigitated electrodes arrays on polymer with integrated microuidics for direct bio-anity sensing using impedimetric measurements. Sens. Actuators A, 2007, 136, 518526.

[31] Aarnoutse, R.E.; Schapiro, J.M.; Boucher, C.A.B.; Hekster, Y.A.; Burger, D.M. Therapeutic drug monitoring: an aid to optimising response to antiretroviral drugs? Drugs, 2003, 63, 741753.

[32] Kuo, Y.C.; Chen, C.S.; Chang, K.N.; Lin, C.T.; Lee, C.K. Sensitivity improvement of a miniaturized label-free electrochemical impedance biosensor by electrode edge eect. J. Micro/Nanolithogr., MEMS, MOEMS., 2014, 13, 033019.

[33] Wallace, R.; Shaer, J.; Murphy, R.; Bonner, J.; Hirose, T.; Itakura, K. Hybridization of synthetic oligonucleotides: the eect of single base pair mismatch. Nucleic Acids research, 1979, 6(11), 3543-3558.

[34] Souteyrand, E.; Cloarec, J.P.; Martin, J.R. Direct detection of the hybridization of synthetic homo-oligomer DNA sequences by eld eect. J. Phys. Chem. B, 1997,Vol. 101(15), 2980-2985.

[35] Waleed Shinwari, M. Static and Dynamic Modeling of DNA Biosensors for BioMedical Applications, 2007, http://hdl.handle.net/11375/11236.

[36] Bano, F.; Fruk, L.; Sanavio, B.; Glettenberg, M.; Casalis, L.; Niemeyer, C.M.; Scoles,G. Toward multiprotein nanoarrays using nanografting and dna directed immobilization of proteins. Nano letters, 2009, 9(7), 26142618.

[37] Mirmomtaz, E.; Castronovo, M.; Grunwald, C.; Bano, F.; Scaini, D.; Ensa, A.A.; Scoles,G.; Casalis, L. Quantitative study of the eect of coverage on the hybridization eciency of surface-bound DNA nanostructures. Nano letters, 2008, 8(12), 41344139.

[38] Ianeselli., L. PhD Thesis, SISSA, Trieste 2013, http://www.sissa.it/sbp/phdsection/AlumniThesis/Luca%20Ianeselli.pdf.

[39] Guiducci, C.; Stagni, C.; Zuccheri, G.; Bogliolo, A.; Benini, L.; Samorì, B.; Riccò, B. A Biosensor for Direct Detection of DNA Sequences Based on Capacitance Measurements. Proc. European Solid State Research, 2002, 479482.

[40] Guiducci, C. DNA detection by integrable electronics. Biosensors and Bioelectronics, 2004, 19(8), 781787.

[41] Carrara, S.; Bhalla,V.; Stagni, C.; Benini, L.; Ferretti, A.; Valle, F.; Gallotta, A.; Riccò, B.; and Samorì, B. Label-free cancer markers detection by capacitance biochip. Sens. Actuators B, 2009, 136, 163172.

[42] Lehninger 5th edition

[43] Strong, L.; Whitesides, G. M. The Structures of Self-Assembled Monolayer Films of Organosulfur Compounds Adsorbed on Gold Single Crystals: Electron Diraction Studies. Langmuir, 1988, 4, 546-558.

[44] Dubois, L.H.; Nuzzo, R.G. Synthesis, Structure, and Properties of Model Organic Surfaces. Annu. Rev. Phys. Chem., 1992, 43, 437-463.

[45] Lavrich, D. ; Wetterer, S.; Bernasek, S.; Scoles, G. Physisorption and Chemisorption of alkanethiols and alkylsuldes on Au(111). J.Phys. Chem. B, 1998, 102(18), 3456.

[46] Vericat, C.; Vela, M.E.; Benitez, G.; Carro, P.; Salvarezza,R.C. Self-assembled monolayers of thiols and dithiols on gold:new challenges for a well known system. Chem. Soc. Rev, 2010, 39, 1805-1834.

[47] Schreiber, F. Structure and growth of self-assembling monolayers. Progress in surface science, 2000, 65(5), 151 257.

[48] Peterson, A.W.; Heaton, R.J.; Georgiadis, R.M. The eect of surface probe density on DNA hybridization. Nucleic Acids Res., 2001, 29, 51635168.

[49] Petrovykh, D.Y.; Kimura-Suda, H.; Whitman, L.J.; Tarlov, M.J. Quantitative analysis and characterization of DNA immobilized on gold. J. Am. Chem. Soc., 2003, 5219-5226.

[50] O'Shaughnessy, B.; Yang, Q. Strongly charged polymer brushes. Europhys. Lett., 2006, 75, 427433.

[51] Toomey, R.; Tirrell, M. Functional polymer brushes in aqueous media from self-assembled and surface-initiated polymers. Annu. Rev. Phys. Chem., 2008, 59, 493517.

[52] Bosco, A.; Bano, F.; Parisse, P.; Casalis, L.; De Simone A.; Micheletti C. Hybridization in nanostructured DNA monolayers probed by AFM: theory versus experiment. Nanoscale, 2012, 4, 1734-1741.

[53] Castelino, K.; Kannan, B.; A. Majumdar. Characterization of grafting density and binding eciency of DNA and proteins on gold surfaces. Langmuir, 2005, 21, 19561961.

[54] Goren, Y.; Kushnir, M.; Zafrir, B.; Tabak, S.; Lewis, B.S.; Amir, O. Serum levels of microRNAs in patients with heart failure. Eur. J. Heart Fail., 2012, 14, 147154.

[55] Bauters, C.; Kumarswamy, R.; Holzmann, A.; Bretthauer, J.; Anker, S.D.; Pinet, F., Thum, T. Circulating miR-133a and miR-423-5p fail as biomarkers for left ventricular remodeling after myocardial infarction. Int. J. Cardiol., 2013, 168, 1837-40.

[56] Love, J.C.; Estro, L.A.; Kriebel, J.K.; Nuzzo, R.G.; Whitesides, G.M. Self-Assembled Monolayers of Thiolates on Metals as a Form of Nanotechnology. Chem. Rev., 2005, 105, 1103=1169.

[57] Arinaga, K.; Rant, U.; Knezevic, J.; Pringsheim, E.; Tornow, M.; Fujita, S.; Abstreiter, G.; Yokoyama, N. Controlling the surface density of DNA on gold by electrically induced desorption. Biosens Bioelectron., 2007, 23(3), 326-331.

[58] Bard, A.J.; Faulkner, L.R. Electrochemical Methods, J. Wiley, New York, 2001, Chapter 13.

[59] Falkenhagen, H. Electrolytes, Oxford University Press, 1934, London, p. 73.

[60] Hasted, J.B.; Ritson, D.M.; Collie, C.H. Dielectric Properties of Aqueous Ionic Solutions. Parts I and II. J. Chem. Phys., 1948, 16, 1.

[61] Singh, M.B.; Kant, R. Debye-Falkenhagen dynamics of electric double layer in presence of electrode heterogeneities. J. Electroanal. Chem., 2013, 704, 197-207.

[62] Nkoua Ngavouka, M. D.; Bosco, A.; Casalis, L.; Parisse, P. Determination of Average Internucleotide Distance in Variable Density ssDNA Nanobrushes in the Presence of Dierent Cations Species. Macromolecules, 2014, 47(24), 8748-8753.

[63] Wang, K.; Hamill, J.M.; Wang, B.; Guo, C.; Jiang, S.; Huangb, Z.; Xu, B. Structure determined charge transport in single DNA molecule break junctions. Chem. Sci., 2014, 5, 3425.

[64] Persson, B.; Stenhag, K.; Nilsson, P.; Larsson, A.; Nygren, P. Analysis of oligonucleotide probe anities using surface plasmon resonance as means for mutational scanning. Anal. Biochem., 1997 246(1),3444.

[65] Long, F.; Wu, S.; He, M.; Tong, T.; Shi, H. Ultrasensitive quantum dots-based DNA detection and hybridization kinetics analysis with evanescent wave biosensing platform. Biosens. Bioelectron., 2011, 26(5),23905.

[66] Rao, A.N.; Rodesch,C.K.; Grainger, D.W. Real-time uorescent image analysis of DNA spot hybridization kinetics to assess microarray spot heterogeneity. Anal. Chem., 2012, 84(21):9379 87.

[67] Li, D.; Zou, X.; Shen, Q.; Dong, S. Kinetic study of DNA/DNA hybridization with electrochemical impedance spectroscopy. Electrochem. Commun., 2007, 9(2), 191196.

[68] Mandel. M. Dielectric properties of charged linear macromolecules with particular reference to DNA. Ann. N. Y. Acad. Sci., 1977, 303, 74-87.

[69] Fumagalli, L.; Ferrari, G.; Sampietro, M.; Gomila, G. Dielectric-constant measurement of thin insulating lms at low-frequency by nanoscale capacitance microscopy. Appl. Phys. Lett., 2007, 91, 243110.

[70] Tomiz, S.; Dolanski Babic S.; Vuletic, T.; Krca, S.; Ivankovic, D.; Griparic L.; Podgornik, R. Dielectric relaxation of DNA aqueous solutions. Phys. Rev. E, 2008, 75, 021905.

[71] Liu, Y.S.; Banada, P.P.; Bhattacharya, S.; Bhunia A.K.; Bashir R. Electrical charactherization of DNA molecules in solution using impedance measurements. Appl. Phys. Lett., 2008, 92, 143902.

[72] Hubbard, J.B.; Onsager, L.; van Beek, W.M.; Mandel, M. Kinetic polarization deciency in electrolyte solutions. Proc. Natl. Acad. Sci. USA, 1977, 74(2), 401-404.

[73] Sips, R. Combined form of Langmuir and Freundlich equations. The Journal of Chemical Physics, 1948, 16, 490495.

[74] Chan, V.; Graves, D.J.; McKenzie, S.E. The biophysics of DNA hybridization with immobilized oligonucleotide probes. Biophys. J., 1995, 69, 2243-2255.

[75] Gong, P; Levicky, R. DNA surface hybridization regimes. PNAS, 2008, 105(14), 5301-5306.

[76] Wong, I.Y.; Melosh, N.A. An electrostatic model for DNA surface hybridization. Biophys. J., 2010, 98, 2954-2963.

[77] Peterson, A.W.; Wolf, L.K.; Georgiadis, R.M. Hybridization of mismatched or partially matched DNA at surfaces. J. Am. Chem. Soc., 2002, 682, 14601-607.

[78] Rant, U.; Arinaga, K.; Fujita, S.; Yokoyama, N.; Abstreiter, G.; Tornow, M. Dynamic electrical switching of DNA layers on a metal surface. Nano Lett., 2004, 4 (12), 24412445.

[79] Rant, U.; Arinaga, K.; Fujita, S.; Yokoyama, N.; Abstreiter, G.; Tornow, M. Electrical manipulation of oligonucleotides grafted to charged surfaces. Org. Biomol. Chem., 2006, 4 (18), 3448.

[80] Wong, I. Y.; Footer, M. J.; Melosh, N. A. Dynamic control of biomolecular activity using electrical interfaces. Soft Matter, 2007,3, 267-274.

[81] Wong, I. Y.; Melosh, N. A. Directed hybridization and melting of DNA linkers using counterion-screened electric elds. Nano Lett., 2009, 9, 35213526.

[82] Nakatani, K. Chemistry challenges in SNP typing. ChemBioChem, 2004, 5, 1623.

[83] Merkoci, A. Nanoparticles-based strategies for DNA, protein and cell sensors. Biosens. Bioelectron., 2010, 26, 11641177.

[84] Knez, K.; Spasic,D.; Janssen,K.P.F.; Lammertyn, J. Emerging technologies for hybridization based single nucleotide polymorphism detection. Analyst, 2014, 139, 353.

[85] Capaldo, P.; and Nkoua Ngavouka, M. D.; Ambrosetti, E.; Scoles, G.; Casalis, L.; Parisse,P. Mismatch detection in DNA monolayers by atomic force microscopy and electrochemical impedance spectroscopy. Beilstein J. Nanotechnol., 2016, 7, 220-227.

[86] Craig, M.E.; Crothers, D.M.; Doty, P. Relaxation kinetics of dimer formation by self complementary oligonucleotides. J. Mol. Biol., 1971, 62, 383-401.

[87] Pörschke, D.; Eigen, M. Co-operative non-enzymatic base recognition III. Kinetics of the helix-coil transition of the oligoribouridylic - oligoriboadenylic acid system and of oligoriboadenylic acid alone at acidic pH. J. Mol. Biol., 1971, 62, 361-381.

[88] Erickson, D.; lo, D.; Krull, U.J. Modeling of DNA hybridization kinetics for spatially resolved biochips. Anal. Biochem., 2003, 317, 186-200.

[89] Hagan, M.F.; Chakraborty, A.K. Hybridization dynamics of surface immobilized DNA. J. Chem. Phys., 2004, 120, 4958-4968.

[90] Bosco, A.; Bano, F.; Parisse, P.; Casalis, L.; DeSimone, A.; Micheletti, C. Hybridization in nanostructured DNA monolayers probed by AFM: theory versus experiment. Nanoscale, 2012, 4, 1734-1741.

[91] Asbury, C.; van der Engh, G. Trapping of DNA in nonuniform oscillating electric elds. Biophys. J., 1998, 74, 1024-1030.

[92] Wong, P.K.; Chen, C-Y.; Wang T-H.; Ho C-M. Electrokinetic bioprocessor for concentrating cells and molecules. Anal. Chem., 2004, 76(23)89086914.

[93] Wu, C.C; Huang, W.E., Hu, C.C. An ultrasensitive label-free electrochemical impedimetric DNA biosensing chip integrated with a DC-biased AC electroosmotic vortex. Sensor. Actuat. B-Chem., 2015, 209, 61-68.

[94] Cheng, I-F.; Senapati, S.; Cheng, X.; Basuray, S.; Chang, H-C.; Chang, H-C. A rapid eld-use assay for mismatch number and location of hybridized DNAs. Lab. Chip, 2010, 10, 828831.

[95] Fernádez-Morales, F.H.; Duarte, J.E.; Samitier-Martí, J. Bacterial handling under the inuence of non-uniform electric elds: dielectrophoretic and electrohydrodynamic eects. An. Acad. Bras. Cienc., 2008, 80(4), 627-638.

[96] Singh, M.B.; Kant, R. Debye-Falkenhagen dynamics of electric double layer in presence of electrode heterogeneities. J. Electroanal. Chem., 2013, 704, 197-207.

[97] Loucaides, N.G..; Ramos, A.; Georghiou, G.E. Dielectrophoretic and AC electroosmotic trapping of DNA: Numerical simulation incorporating uid dynamics and steric particle eects. J. Electrostat., 2011, 69(2), 111-118.

[98] Ramos, A.; Morgan, H.; Green, N.G.; Castellanos, A. AC electrokinetics; a review of forces in microelectrode structures. J. Phys. D: Appl. Phys., 1998, 31, 2338-2353.

[99] Bustamante, C.; Smith, S.; Liphardt, J.; Smith, D. Single-molecule studies of DNA dynamics. Curr. Opin. Struct. Biol., 2000, 10(3), 279-285.

[100] Baumgärtner, A. Statics and dynamics of the freely jointed polymer chain with Lennard- Jones interaction. J. Chem. Phys., 1980, Vol. 72(2), 871-879.

[101] Karplus, M.; McCammon, J. Molecular dynamics simulations of biomolecules. Nat. Struct. Biol., 2002, 9(9), 646-652.

[102] Sherrill, C.D. An Introduction to Hartree-Fock Molecular Orbital Theory. School of Chemistry and Biochemistry, Georgia Institute of Technology, 2000. http://vergil.chemistry.gatech.edu/notes/hf-intro/hf-intro.pdf

[103] Kohn, W.; Sham, L.J. Self-Consistent Equations Including Exchange and Correlation Eects". Phys. Rev., 1965, 140 (4A): A1133A1138.

[104] Parr, R.G.; Yang, W. Density-Functional Theory of Atoms and Molecules. Oxford University Press, 1994, ISBN 978-0-19-509276-9.

[105] Bown, M.R.; Meinhart, C.D. AC electroosmotic ow in a DNA concentrator. Microuid. Nanouid., 2006, 2, 513-523.

[106] Gonzalez,A.; Ramos, A.; Green, N.G.; Castellanos,A.; Morgan, H. Fluid ow induced by nonuniform AC electric elds in electrolytes on microelectrodes. II. A linear double-layer analysis. Phys. Rev. E Stat. Nonlin. Soft Matter Phys., 2000, 61(4), 40194028.

[107] Green, N.G.; Ramos, A.; Gonzalez,A.; Morgan, H.; Castellanos,A. Fluid ow induced by nonuniform AC electric elds in electrolytes on microelectrodes. III. Observation of streamlines and numerical simulation. Phys. Rev. E Stat. Nonlin. Soft Matter Phys., 2002, 66, 026305(1-11).

[108] Kestin, J.; Khalifa, H.E.; Correia, R.J. Tables of the dynamic and kinematic viscosity of acqueous KCl solution in the temperature range 25-150°C and the pressure range 0.1-35 MPa.http://www.nist.gov/data/PDFfiles/jpcrd175. pdf

[109] Hart, R.; Lec, R.; Noh, H.M. Enhancement of heterogeneous immunoassays using AC electroosmosis. Sens. Actuator. B-Chem, 2010, 147, 366-375.

[110] Ha, M. and Narry Kim, V. Regulation of microRNA biogenesis.Nat. Rev. Mol. Cell Biol., 2004, 15, 509524.

[111] Lee, R.C.; Feinbaum,R.L.; Ambros, V. The C. elegans heterochronic gene lin-4 encodes small RNAs with antisense complementarity to lin-14. Cell., 1993, 75(5), 843-854.

[112] Cissell, KA and Deo, S.K. Trends in microRNA detection. Anal. Bioanal. Chem., 2009, 394, 11091116.

[113] Takada, S. and Asahara, H. Current strategies for microRNA research. Mod. Rheumatol., 2012, 22, 645653.

[114] Calin, G.A.; Dumitru, C.D.; Shimizu, M.; Bichi, R.; Zupo, S.; Noch, E.; Aldler, H.; Rattan, S.; Keating, M.; Rai, K.; Rassenti, L.; Kipps, T.; Negrini, M.; Bullrich, F.; Croce, C.M. Frequent deletions and down-regulation of micro- RNA genes miR15 and miR16 at 13q14 in chronic lymphocytic leukemia. PNAS, 2002, 99(24), 15524-15529.

[115] Griths-Jones laboratory at the Faculty of Life Sciences,University of Manchester. miRBase:the microRNA database. http://www.mirbase.org/

[116] Visone, R.; Rassenti, L.Z.; Veronese, A.; Taccioli, C.; Costinean, S.; Aguda, B.D.; Volinia, S.; Ferracin, M.; Palatini, J.; Balatti, V.; Alder, H.; Negrini, M.; Kipps, T.J.; Croce C.M. Karyotype-specic microRNA signature in chronic lymphocytic leukemia. Blood., 2009, 114, 3872387910.

[117] Roth, C.; Rack, B.; Muller, V.; Janni, W.; Pantel, K.; Schwarzenbach, H. Circulating microRNAs as blood-based markers for patients with primary and metastatic breast cancer. Breast Cancer Res., 2010, 12(6), R90.

[118] Ratner, E.S.; Tuck, D.; Richter, C.; Nallur, S.; Patel, R.M.; Schultz, V.; Hui, P.; Schwartz,P.E.; Rutherford, T.J.; Weidhaas,J.B. MicroRNA signatures dierentiate uterine cancer tumor subtypes. Gynecol. Oncol., 2010, 118(3), 251-257.

[119] de Plannell-Saguer, M.; Rodicio, M. C. Analytical aspects of microRNA in diagnostics: A review. Analytica Chimica Acta., 2011, 699(2), 134-152.

[120] Gilad, S.; Meiri, E.; Yogev, Y.; Benjamin, S.; Lebanony, D.; Yerushalmi, N.; Benjamin, H.; Kushnir, M.; Cholakh, H.; Melamed, N.; Bentwich, Z.; Hod, M.; Goren, Y.; Chajut, A. Serum microRNAs are promising novel biomarkers. PLoS One, 2008, 3(9), e3148.

[121] Heneghan, H.M.; Miller, N.; Lowery, A.J.; Sweeney, K.J.; Newell, J.; Kerin, M.J.; Circulating microRNAs as novel minimally invasive biomarkers for breast cancer. Ann. Surg., 2010, 251(3), 499-505.

[122] Mitchell, P.S.; Parkin, R.K.; Kroh, E.M.; Fritz, B.R.; Wyman, S.K.; Pogosova-Agadjanyan, E.L.; Peterson, A.; Noteboom, J.; O'Briant, K.C.; Allen, A.; Lin, D.W.; Urban, N.; Drescher, C.W.; Knudsen, B.S.; Stirewalt, D.L.; Gentleman, R.; Vessella,R.L.; Nelson, P.S.; Martin, D.B.; Tewari, M.\ Circulating microRNAs as stable blood-based markers for cancer detection. PNAS, 2008, 105(30), 10513-10518.

[123] Mo, M.H.; Chen, L. ; Fu, Y.; Wang, W.; Fu, S. W. Cell-free Circulating miRNA Biomarkers in Cancer. J. Cancer., 2012, 3, 432-448.

[124] Gal, H.; Pandi, G.; Kanner, A.A.; Ram, Z.; Lithwick-Yanai, G.; Amariglio, N.; Rechavi, G.; Givol, D. MIR-451 and Imatinib mesylate inhibit tumor growth of Glioblastoma stem cells. Biochem. Biophys. Res. Commun., 2008, 376(1), 86-90.

[125] Bandres, E.; Bitarte, N.; Arias, F.; Agorreta, J.; Fortes, P.; Agirre, X.; Zarate, R.; Diaz-Gonzalez, J.A.; Ramirez, N.; Sola, J.J.; Jimenez, P.; Rodriguez, J.; Garcia-Foncillas, J. microRNA-451 regulates macrophage migration inhibitory factor production and proliferation of gastrointestinal cancer cells. Clin. Cancer Res., 2009, 15(7), 2281-2290.

[126] Cheng, Y.; Ji, R.; Yue, J.; Yang, J.; Liu, X.; Chen, H.; Dean, D.B.; Zhang, C. MicroRNAs are aberrantly expressed in hypertrophic heart: do they play a role in cardiac hypertrophy?. Am. J. Pathol., 2007, 170(6), 1831-1840.

[127] Goren, Y.; Kushnir, M.; Zafrir, B.; Tabak, S.; Lewis, B.S.; Amir, O. Serum levels of microRNAs in patients with heart failure. Eur. J. Heart. Fail., 2012, 14, 147154.

[128] Bauters, C.; Kumarswamy, R.; Holzmann, A.; Bretthauer, J.; Anker, S. D.; Pinet, F.; Thum, T. Circulating miR-133a and miR-423-5p fail as biomarkers for left ventricular remodeling after myocardial infarction. Int. J. Cardiol., 2013, 168(3), 1837-1840.

[129] Schirle, N.T.; Sheu-Gruttadauria, J.; MacRae, I.J. Structural basis for microRNA targeting. Science, 2014, 346(6209), 608-613.

[130] Gregory R, Chendrimada T, Cooch N, Shiekhattar R. Human RISC couples microRNA biogenesis and posttranscriptional gene silencing.Cell, 2005, 123 (4), 63140.

[131] Kupferschmidt, K. A Lethal Dose of RNA. Science, 2013, 341(6147), 7323.

[132] Turchinovich, A.; Samatov, T.R.; Tonevitsky, A.G.; Burwinkel, B. Circulating miRNAs: cell-cell communication function? Front Genet, 2013, 4, 119.

[133] Shen, Y.; Jacobs,J. M.; Camp, D.G.; Fang, R; Moore, R.J.; Smith, R.D.; Xiao, W.; Davis, R.W.; Tompkins, R.G. Ultra-High-Eciency Strong Cation Exchange LC/RPLC/MS/MS for High Dynamic Range Characterization of the Human Plasma Proteome. Anal. Chem. , 2004, 76, 1134-1144.

[134] van der Geer, P.; Hunter, T.; Lindberg, R.A. Receptor protein-tyrosine kinases and their signal transduction pathways. Annu. Rev. Cell. Biol., 1994,10, 251-337.

[135] Lawson, A.D.G. Antibody-enabled small-molecule drug discovery. Nat. Rev. Drug Discov., 2012, 11, 519-525.

[136] Muyldermans, S. Nanobodies: Natural Single-Domain Antibodies. Annu. Rev. Biochem., 2013, 82, 775797.

[137] Fridy, P.C.; Li, Y.; Keegan,S.;Thompson, M.K.; Nudelman, I.; Scheid, J.F.; Oenger, M.; NussenzweigM.C.; Fenyö,D.; Chait, B.T.; Rout, M.P. A robust pipeline for rapid production of versatile nanobody repertoires.Nat. Methods., 2014, 11(12), 12531260.

[138] Carney, W.; Bernhardt, D.; Jasani, B. Circulating HER2 Extracellular Domain: A Specic and Quantitative Biomarker of Prognostic Value in all Breast Cancer Patients? Biomark. Cancer, 2013, 5, 31-39.

[139] Wol, A.C et al. Reccomandations for human epidermalgrwoth factor receptor 2 testing in breast cancer: American Society of Clinical Oncology/College of American Pathologists Clinical Practice Guideline Update. JCO, 2013, 31(31), 3997-4013.

[140] Djender, S.; Beugnet, A.; Schneider, A.; de Marco, A. The Biotechnological Applications of Recombinant Single-Domain Antibodies Optimized by the C-Terminal Fusion to the EPEA Sequence (C Tag). Antibodies, 2014, 3, 182191.

[141] Djender, S.; Schneider, A.; Beugnet, A.; Crepin, R.; Desrumeaux, K.E.; Romani, C.; Moutel, S.; Perez,F.; de Marco, A. Bacterial cytoplasm as an eective cell compartment for producing functional VHH-based anity reagents and Camelidae IgG-like recombinant antibodies. Microb. CellFact., 2014, 13, 140-150.

[142] Keller, E.; Beeser, H.; Peter, H.H.; Arnold, A.; Kotitschke, R. Comparison of fresh frozen plasma with a standardized serum protein solution following therapeutic plasma exchange in patients with autoimmune diseasea prospective controlled clinical trial. Ther. Apher., 2000, 4(5), 332-337.

[143] Vincke, L.R.; Saerens, D.; Martinez-Rodriguez, S.; Muyldermans, S.; Conrath, K. General Strategy to Humanize a Camelid Single-domain Antibody and Identication of a Universal Humanized Nanobody Scaold. J. Biol. Chem., 2009, 284(5), 32733284.

[144] Gaster, R.S.; Hall, D.A.; Neilson, C.; Osterfeld, S.J.; Heng, Yu; Mach, K.; Wilson, R.J.; Murmann, B.; Liao, J. C.; Gambhir, S.S.; Shan, X.W. Matrix-insensitive protein assays push the limits of biosensors in medicine,Nat. Med., 2009, 15, 1327-1332.

[145] Boozer, C.; Ladd, J.; Chen, S.; Yu, Q.; Homola, J.; Jiang, S. DNA directed protein immobilization on mixed ssDNA/oligo (ethylene glycol) self-assembled monolayers for sensistive biosensors. Anal. Chem., 2004, 76(23), 6967-6972.

[146] Bosco, A.; Ambrosetti, E.; Mavri, J.; Capaldo, P.; Loredana Casalis. Miniaturized Aptamer-based assays for protein detection. Sensors, 2016. in press

[147] Deka, J.; M¥ch, R.; Ianeselli, L.; Amenitsch, H.; Cacho-Nerin, F.; Parisse, P.; and Casalis, L. Surface Passivation Improves the Synthesis of Highly Stable and Spe-cic DNA-Functionalized Gold Nanoparticles with Variable DNA Density. ACS Appl. Mater. Interf aces, 2015, 7(12), 70337040.

[148] Frens, G. Controlled nucleation for the regulation of the particle size in monodis-perse gold suspensions. Nat. Phys. Sci., 1973, 241, 20-22.

[149] Liu, G.; Liud, J.; Davisc, T.P.; Goodinga, J.J. Electrochemical impedance im-munosensor based on gold nanoparticles and aryldiazonium salt functionalized gold electrodes for the detection of antibody. Biosens. Bioelectron., 2011, 26, 36603665.

[150] Zeng, S.; Wang, S.; Wang, L.; Yang, L.; Chen, Z.; Liang1, Z. A Novel CD105 Determination System Based on an Ultrasensitive Bioelectrochemical Strategy with Pt Nanoparticles. Sensors, 2012, 12(10), 1347113479.

[151] Srinivasaraghavan, V.; Strobl, J.; Wang, D.; Hein, J.R.; Agah, M. A comparative study of nano-scale coatings on gold electrodes for bioimpedance studies of breast cancer cells. Biomed. Microdevices, 2014, 16(5), 689-696.

[152] Wu, B.; Hou, S.; Miao, Z.; Zhang, C.; Ji, Y. Layer-by-Layer Self-Assembling Gold Nanorods and Glucose Oxidase onto Carbon Nanotubes Functionalized Sol-Gel Matrix for an Amperometric Glucose Biosensor. Nanomaterials, 2015, 5, 1544-1555.

[153] Sastry, M.; Kumar, A.; Mukherjee, P. Phase transfer of aqueous colloidalgold particles into organic solutions containing fatty amine molecules.Colloids Surf. A, 2001, 181, 255-259.

[154] Li, W.; Xu, R.; Wang, L.; Cui, H.; Xi, S.Q. Superlattice structure of gold nanoparticles lm deposited by Langmuir-Blodgett technique. Mol. Cryst. Liq. Cryst., 1999, 337, 185-188.

[155] Shein, J.B.; Lai, L.M.H.; Eggers,P.K.; Paddon-Row,M.N.; Gooding, J.J. Langmuir, 2009, 25, 1112111128.

[156] Shinwari, M.W.; Zhitomirsky, D.; Deen, I.A.; SelvaganapathyP.R.; Deen, M.J.; Landheer, D. Microfabricated reference electrodes and their biosensing applications. Sensors, 2010, 10, 1679-1715.

[157] Polk, B. J.; Stelzenmuller, A.; Mijares, G.; MacCrehan, W.; Gaitan, M. Ag/AgCl microelectrodeswith improved stability for microuidics. Sens. Actuators, B, 2006, 114, 239247.

[158] Guth, U.; Gerlach, F.; Decker, M.; Oelssner, W.; Vonau, W. Solid-state reference electrodes for potentiometric sensors. J. Solid State Electrochem., 2009, 13, 2739.

[159] Kim, T.Y.; Hong, S.A.;Yang, S. A solid-state thin-lm Ag/AgCl reference electrode coated with graphene oxide and its use in a pH sensor. Sensors, 2015, 15, 6469-6482.

[160] Kim, H.R.; Kim, Y.D.; Kim, K.I.; Shim, J.H.; Nam, H.; Kang, B.K. Enchancement of physical and chemical properties of thin lm Ag/AgCl reference electrode using a Ni buer layer. Sens. Actuators, B, Chem., 2004, 97, 348354.

[161] Carlborg, C.F.; Haraldsson, T.; Öberg, K.; Malkoch, M.; van der Wijngaart, W. Beyond PDMS: o-stoichiometry thiolene (OSTE) based soft lithography for rapid prototyping of microuidic devices. Lab. Chip, 2011, 11, 3136-3147.

[162] Samad, M.F.; Kouzani, A.Z.; Rahman, M.M.; Magniez, K.; A. Kaynak. Design and fabrication of an electrode for low-actuation-voltage electrowetting-on-dielectric devices. Procedia Technology, 2015, 20, 20 25.

[163] Debye, P. Polar Molecules. Dover Publication, New York, 1929, 18, 89-95.

[164] Myroshnychenko, V.; Brosseau, C. Finite-element modeling method for the prediciton of the complex eective permittivity of two-phase random statistically isotropic heterostructures. J.Appl. Phys., 2005, 97 044101.

[165] Marin, C.N.; Malaescu,I.; Savici, A. Investigation of the Low Frequency Polarization Mechanisms in Magnetic Fluids. Acta. Phys. Pol. A, 2013, 124, 724727.

[166] Bock, L.C.; Grin, L.C.; Latham, J.A.; Vermaas,E.H.; Toole, J.J. Selection of single-stranded DNA molecules that bind and inhibit human thrombin. Nature, 1992, 355, 564-566.

[167] Padmanabhan,K.; Padmanabhan,K.P.; Ferrara, J.D.; Sadler, J.E.; Tulinsky, A. The structure of alpha-thrombin inhibited by a 15-mer single-stranded DNA aptamer. J. Biol. Chem., 1993, 268, 17651-17654.

[168] Padmanabhan, K.; Tulinsky, A. An ambiguous structure of a DNA 15-mer thrombin complex. Acta Crystallogr. Sect. D-Biol. Crystallogr., 1996, 52, 272-282.